

AD-A268 358

MENTATION PAGE

Form Approved
OMB No. 0704-0188

2

is estimated to average 1 hour per response, including the time for reviewing instructions, searching existing data sources, gathering and reviewing the collection of information, sending comments regarding this burden estimate or any other aspect of this collection of information, including this burden estimate, to Washington Headquarters Services, Directorate for Information Operations and Reports, 1215 Jefferson Davis Highway, Suite 1204, Arlington, VA 22202-4302, and to the Office of Management and Budget, Paperwork Reduction Project (0704-0188), Washington, DC 20503.

1. AGENCY USE ONLY (Leave blank)		2. REPORT DATE Jun 1993		3. REPORT TYPE AND DATES COVERED THESIS/ DISSERTATION	
4. TITLE AND SUBTITLE Budget Studies of a Prefrontal Convective Rainband in Northern Taiwan Determined From Tamex Data				5. FUNDING NUMBERS C	
6. AUTHOR(S) Martin R. Martino					
7. PERFORMING ORGANIZATION NAME(S) AND ADDRESS(ES) AFIT Student Attending: St Louis University				8. PERFORMING ORGANIZATION REPORT NUMBER AFIT/CI/CIA- 93-047	
9. SPONSORING / MONITORING AGENCY NAME(S) AND ADDRESS(ES) DEPARTMENT OF THE AIR FORCE AFIT/CI 2950 P STREET WRIGHT-PATTERSON AFB OH 45433-7765				10. SPONSORING / MONITORING AGENCY REPORT NUMBER	
11. SUPPLEMENTARY NOTES					
12a. DISTRIBUTION / AVAILABILITY STATEMENT Approved for Public Release IAW 190-1 Distribution Unlimited MICHAEL M. BRICKER, SMSgt, USAF Chief Administration				12b. DISTRIBUTION CODE	
13. ABSTRACT (Maximum 200 words) DTIC ELECTE AUG 20 1993 S A D 93-19314 					
14. SUBJECT TERMS				15. NUMBER OF PAGES 171	
				16. PRICE CODE	
17. SECURITY CLASSIFICATION OF REPORT		18. SECURITY CLASSIFICATION OF THIS PAGE		19. SECURITY CLASSIFICATION OF ABSTRACT	
				20. LIMITATION OF ABSTRACT	

**Budget studies of a prefrontal convective rainband in northern
Taiwan determined from TAMEX data**

Martin Russell Martino

Rank: Captain

Branch: United States Air Force

Year: 1993

Number of Pages: 171

Degree: Master of Science (Research)

School: Saint Louis University

St. Louis, MO 63103

ABSTRACT

The budgets of total kinetic energy, horizontal momentum flux and three-dimensional vorticity for a subtropical prefrontal convective rainband associated with the Mei-Yu front on 25 June 1987 over northern Taiwan are investigated. This slow-moving system lasted for more than 10 hours and produced heavy precipitation over northern and central Taiwan. Doppler radar data from the TOGA and CP-4 radars captured this event during the morning hours. Dual-Doppler derived three-dimensional winds and retrieved thermodynamic parameters were processed from the 0653 and 0700 LST 25 June volume scans. A $25 \times 40 \text{ km}^2$ rotated horizontal domain encompassing the investigated rainband with a 1 km three-dimensional grid spacing was used for the budget calculations.

The total kinetic energy budget revealed that there was an upward transport of mean kinetic energy throughout the rainband with the strongest transport within the middle levels. The main sources of kinetic energy generation were due to the horizontal generation and the total buoyancy production terms. The two main processes that reduced the kinetic energy of the system were horizontal flux divergence and dissipation due to frictional forces. The momentum-flux budget showed that the shear production, the total buoyancy production and the velocity-pressure interaction terms were the strongest contributors to the local time-change of eddy horizontal momentum flux. The three-dimensional vorticity budget analyses implied that the tilting/tipping of vorticity into the horizontal and the vertical very likely increased circulation thus prolonging the lifetime of the rainband.

Accession For	
NTIS	CRA&I <input checked="" type="checkbox"/>
DTIC	TAB <input type="checkbox"/>
Unannounced	<input type="checkbox"/>
Justification	
By	
Distribution/	
Availability Codes	
Dist	Avail and/or Special
A-1	

BIBLIOGRAPHY

- Barnes, S., 1973: Mesoscale objective analysis using weighted time series observations. *NOAA Tech. Memo. ERL-NSSL-62*, 60 pp., 1973.
- Beeson, M.R., 1991: An observational study of a prefrontal convective rainband using TAMEX single- and dual-Doppler data. M.S. Thesis, Saint Louis University. 106 pp.
- Chang, H.W., 1992: Dynamic and thermodynamic characteristics of a prefrontal convective rainband in northern Taiwan determined from TAMEX data. Ph.D. Thesis, Saint Louis University. 155 pp.
- Chen, G. T.-J., 1983: Observational aspect of the Mei-Yu phenomenon in subtropical China. *J. Met. Soc. Japan.*, **61**, 306-312.
- _____, and Y.-H. Kuo, 1991: The scientific results of TAMEX. Proceedings, *International Conference on Mesoscale Meteorology and TAMEX*. 3-6 December 1991, Taipei, Taiwan, 7-15.
- Douglas, M. W., 1992: Structure and dynamics of two monsoon depressions. Part II: Vorticity and heat budgets. *Mon. Wea. Rev.*, **120**, 1548-1564.
- Fuelberg, H. E., and J. R. Scoggins, 1978: Kinetic energy budgets during the life cycle of intense convective activity. *Mon. Wea. Rev.*, **106**, 637-653.
- _____, and M. F. Printy, 1984: A kinetic energy analysis of the meso- β -scale severe storm environment. *J. Atmos. Sci.*, **41**, 3212-3226.
- Gal-Chen, T., 1978: A method for the initialization of the anelastic equations: Implications for matching models with observations. *Mon. Wea. Rev.*, **106**, 587-606.
- _____, 1982: Errors in fixed and moving frame of references: Applications for conventional and Doppler radar analysis. *J. Atmos. Sci.*, **39**, 2279-2300.
- Kung, E. C., and T. L. Tsui, 1975: Subsynoptic-scale kinetic energy balance in the storm area. *J. Atmos. Sci.*, **32**, 729-740.
- Kuo, Y. H., and G. T. -J. Chen, 1990: Taiwan Area Mesoscale Experiment: An overview. *Bull. Amer. Meteor. Soc.*, **71**, 488-503.

- Lee, W. C., R. Wakimoto, and R. Carbone, 1992: The evolution and structure of a "Bow-Echo-Microburst" event. Part II: The bow echo. *Mon. Wea. Rev.*, **120**, 2211-2225.
- LeMone, M. A., 1983: Momentum transport by a line of cumulonimbus. *J. Atmos. Soc.*, **40**, 1815-1834.
- _____, G. M. Barnes, and E. J. Zipser, 1984: Momentum flux by lines of cumulonimbus over the tropical oceans. *J. Atmos. Sci.*, **41**, 1914-1932.
- _____, and D. P. Jorgensen, 1991: Precipitation and kinematic structure of an oceanic mesoscale convective system. Part II: Momentum transport and generation. *Mon. Wea. Rev.*, **119**, 2638-2653.
- Lin, Y. J., and R. W. Pasken, 1982: A diagnostic study of the tornadic storm based on dual-Doppler wind measurements. *Cloud Dynamics* (Agee and Asai, Eds.), D. Reidel Publication Co., 315-328.
- _____, and P. M. Condray, 1988: Momentum flux in the subcloud layer of a microburst-producing thunderstorm determined from JAWS dual-Doppler data. *Boundary-Layer Meteorology*, **43**, 125-141.
- _____, and J. A. Coover, 1988: A kinetic energy analysis of a microburst-producing thunderstorm based on JAWS dual-Doppler data. *J. Atmos. Sci.*, **45**, 2764-2771.
- _____, and P. G. LaPointe, 1991: Observational study of a multiple microburst-producing storm. Part III: Vorticity budgets. *TAO*, **2**, 217-241.
- _____, R. W. Pasken, and H. Shen, 1991: Momentum-flux budgets of a subtropical squall line in TAMEX IOP-2 based on dual-Doppler data. Preprints, *International Conference on Mesoscale Meteorology and TAMEX*, 3-6 December, Taipei, Taiwan, Meteor. Soc. Rep. China and Amer. Meteor. Soc., 133-139.
- _____, H. Shen, and R. W. Pasken, 1991: Kinetic energy budget of a squall line over the Taiwan straits revealed by dual-Doppler radar. *Mon. Wea. Rev.*, **119**, 2654-2663.
- _____, R. W. Pasken, and H. W. Chang, 1992: The structure of a subtropical prefrontal convective rainband. Part I: Mesoscale kinematic structure determined from dual-Doppler measurements. *Mon. Wea. Rev.*, **120**, 1816-1836.

- _____, H. W. Chang, and R. W. Pasken, 1993: The structure of a subtropical prefrontal convective rainband. Part II: Dynamic and thermodynamic structures and momentum budgets. *Mon. Wea. Rev.*, **121**, (in press).
- Miglioranza, M. J., 1992: The kinematic structure of a prefrontal convective rainband revealed by TAMEX Doppler radar data. M.S. Thesis, Saint Louis University, 114 pp.
- Rao, G. V., and T. H. Hor, 1991: Observed momentum transport in monsoon convective cloud bands. *Mon. Wea. Rev.*, **119**, 1075-1087.
- Stevens, D. E., 1979: Vorticity, momentum and divergence budgets of synoptic-scale wave disturbances in the tropical eastern Atlantic. *Mon. Wea. Rev.*, **107**, 535-550.
- Townsend, T. L., and J. R. Scoggins, 1983: The influence of convective activity on the vorticity budget. *NASA Contractor Report-3752*, NASA Marshall Space Flight Center, Alabama, 105 pp.
- Wang, T. C., Y. J. Lin, R. W. Pasken, and H. Shen, 1990: Characteristics of a subtropical squall line determined from TAMEX dual-Doppler data. Part I: Kinematic structure. *J. Atmos. Sci.*, **47**, 2357-2381.
- Wiseman, M. L., and J. B. Klemp, 1986: Characteristics of isolated convective storms. *Mesoscale Meteorology and Forecasting* (Edited by Ray, 1986), Chapter 15., Amer. Meteor. Soc., Boston, MA, 331-358.

**BUDGET STUDIES OF A PREFRONTAL CONVECTIVE RAINBAND
IN NORTHERN TAIWAN DETERMINED FROM TAMEX DATA**

Martin R. Martino, B.S.

**A Thesis Presented to the Faculty of the Graduate School
of Saint Louis University in Partial Fulfillment of
the Requirements for the Degree of
Master of Science (Research)**

1993

**BUDGET STUDIES OF A PREFRONTAL CONVECTIVE RAINBAND
IN NORTHERN TAIWAN DETERMINED FROM TAMEX DATA**

Martin R. Martino, B.S.

**A Digest Presented to the Faculty of the Graduate School
of Saint Louis University in Partial Fulfillment of
the Requirements for the Degree of
Master of Science (Research)**

1993

DIGEST

In this study, the budgets of total kinetic energy, horizontal momentum flux and three-dimensional vorticity for a subtropical prefrontal convective rainband associated with the Mei-Yu front on 25 June 1987 over northern Taiwan are investigated. This slow-moving system lasted for more than 10 hours and produced heavy precipitation over northern and central Taiwan. Doppler radar data from the TOGA and CP-4 radars captured this event during the morning hours. Dual-Doppler derived three-dimensional winds and retrieved thermodynamic parameters were processed from the 0653 and 0700 LST 25 June volume scans. A $25 \times 40 \text{ km}^2$ rotated horizontal domain encompassing the rainband with a 1 km three-dimensional grid spacing was used for the budget calculations.

Results for the total kinetic energy budget calculation show that there was an upward transport of mean kinetic energy throughout the rainband with the strongest transport within the middle levels. The main sources for the generation of kinetic energy were the horizontal generation and the total buoyancy production terms. The two main processes that reduced the kinetic energy of the system were horizontal flux divergence and dissipation due to frictional forces. The momentum-flux budget revealed that the shear production, the total buoyancy production and the velocity-pressure interaction terms significantly contributed towards the local time-change of eddy horizontal momentum flux. The three-dimensional vorticity budget analyses implies that the

tilting/tipping of horizontal vorticity into the vertical very likely played a major role in prolonging the lifetime of the prefrontal convective rainband.

**BUDGET STUDIES OF A PREFRONTAL CONVECTIVE RAINBAND
IN NORTHERN TAIWAN DETERMINED FROM TAMEX DATA**

Martin R. Martino, B.S.

**A Thesis Presented to the Faculty of the Graduate School
of Saint Louis University in Partial Fulfillment of
the Requirements for the Degree of
Master of Science (Research)**

1993

COMMITTEE IN CHARGE OF CANDIDACY:

**Professor Yeong-Jer Lin,
Chairperson and Advisor**

Associate Professor Robert W. Pasken

Professor Gandikota V. Rao

ACKNOWLEDGEMENTS

This author would like to express his deepest thanks to Dr. Yeong-Jer Lin for his guidance and assistance in completing this thesis research and throughout my graduate work in the Department of Earth and Atmospheric Sciences at Saint Louis University. Special thanks go to Dr. Robert. W. Pasken for his assistance in his initial development of the software used in this research and for his outstanding patience and guidance in teaching me the operation of the Parks College computer system. Many thanks to the United States Air Force Institute of Technology (AFIT) for giving me the opportunity to gain new knowledge through the pursuit of this advanced degree.

I would personally like to thank all the professors and fellow students at Saint Louis University for all their help and support during my graduate studies. Special thanks to my parents, Robert and Doris, and the rest of my family for all their unending love and support through the years. Most of all, I would like to express my sincere gratitude to my wife, Natalie, and my boys, John and Matt, for their patience and understanding during my graduate studies.

TABLE OF CONTENTS

Title	Page
Chapter 1. Introduction	1
Chapter 2. Literature Review	7
2.1 Kinetic Energy Budget Studies	7
2.2 Momentum-flux Budget Studies	9
2.3 Vorticity Budget Studies	12
Chapter 3. Environmental Summary	16
3.1 Synoptic Conditions	16
3.2 Satellite Display	17
3.3 Surface Observations	20
3.4 Vertical Characteristics	25
3.5 Radar Summary	35
3.6 Rainfall Distribution	40
Chapter 4. Methodology	49
4.1 Data Reduction	49
4.2 Three-dimensional Winds	52
4.3 Error Analysis	55
4.4 Thermodynamic Retrieval	58
4.5 Verifications of the Derived Fields	60
4.6 Rotation Coordinate System	62
4.7 Kinetic Energy Budget	62

Title	Page
4.8 Momentum-flux Budget Calculation	65
4.9 Vorticity Budget Calculation	68
Chapter 5. Discussion of Results	72
5.1 Total Kinetic Energy Budget	73
5.1.1 Horizontal Variations of Kinetic Energy	73
5.1.2 Kinetic Energy Budget Analysis	89
5.1.3 Vertical Totals of Kinetic Energy	99
5.2 Momentum-flux Budget	100
5.2.1 Momentum Fluxes	102
5.2.2 Momentum-flux Budget Analysis	110
5.3 Vorticity Budgets	118
5.3.1 Vorticity Fields	118
5.3.2 Horizontal Variations of Component Terms	132
5.3.3 Analysis of the Vorticity Budget Calculations	150
Chapter 6. Conclusions	160
Bibliography	165
Biography of the Author	171

LIST OF TABLES

Table		Page
1.	Synoptic Characteristics of TAMEX IOP-13 25 June 1987	26
2.	Characteristics of the CP-4 and TOGA radars	50
3.	Total kinetic energy budgets averaged over the domain of interest	101
4.	Results of the u-momentum-flux ($\overline{u'w'}$) budget calculation	111
5.	Results of the v-momentum-flux ($\overline{v'w'}$) budget calculation	116
6.	Area mean and standard deviation values for each vorticity component	130
7.	Area mean and standard deviation values of the vorticity budget terms for each component	152

LIST OF FIGURES

Figure		Page
1.1	TAMEX Doppler network identifying the locations of the CAA, CP-4 and TOGA radars	3
3.1	Progressive positions of the (a) Mei-Yu front and (b) the squall-line gust front (GF) for 25 June 1987	18
3.2	IR imagery from Japan's GMS satellite for (a) 0200 LST, (b) 0500 and (c) 0800 LST on 25 June 1987	19
3.3	Surface observations reported at several northern Taiwan stations on 25 June 1987	21
3.4	Same as in Fig 3.3 except for central west coast and coastal island stations	24
3.5	The environmental sounding at 02 LST 25 June 1987 for the prefrontal atmosphere at Makung in the Taiwan Strait	28
3.6	Same as in Fig. 3.5 except for the postfrontal atmosphere at Pan-Chiao in northern Taiwan	30
3.7	Vertical profile of equivalent potential temperature (θ_e) for Pan-Chiao at 20 LST 24 June and 08 LST 25 June 1987	31
3.8	Time-height variations of rawinsonde winds at Makung on 25 June 1987	32
3.9	Same as in Fig. 3.8 except for Pan-Chiao on 24-25 June 1987	34
3.10	Hourly PPI radar reflectivity distribution (in dBZ) in relation to the gust front and the Mei-Yu front from 0300 LST until 1800 LST 25 June 1987	36-39
3.11	Rainfall rate in <i>mm</i> per 30 minutes for several surface observation stations within the TAMEX mesonet	41

Figure		Page
3.12	Hourly rainfall rates in <i>mm</i> per 30 minutes in relation to the gust front and the Mei-Yu front from 0300 LST until 1800 LST 25 June 1987	43-46
3.13	The accumulated 24 hour rainfall amounts on 25 June 1987 over Taiwan	48
4.1	Domain of interest for the dual-Doppler analysis rotated by 45 degrees	63
5.1	The system-relative horizontal wind field with reflectivity contours <i>Z</i> superimposed at 0.75 km for 0653 LST 25 June 1987	74
5.2	Horizontal distribution of the horizontal flux divergence (HFD) of kinetic energy at 0.75 km for 0653 LST 25 June 1987	75
5.3	Horizontal distribution of vertical velocity, <i>w</i> , at 0.75 km for 0653 LST 25 June 1987	77
5.4	Horizontal distribution of the vertical flux divergence (VFD) of kinetic energy at 0.75 km for 0653 LST 25 June 1987	78
5.5	Horizontal distribution of thermal buoyancy production (BUO) of kinetic energy at 0.75 km for 0653 LST 25 June 1987	79
5.6	Same as in Fig. 5.1 except for 3.75 km	81
5.7	Same as in Fig. 5.2 except for 3.75 km	82
5.8	Same as in Fig. 5.3 except for 3.75 km	83
5.9	Same as in Fig. 5.4 except for 3.75 km	84
5.10	Same as in Fig. 5.5 except for 3.75 km	85
5.11	Same as in Fig. 5.1 except for 6.75 km	86
5.12	Same as in Fig. 5.2 except for 6.75 km	87

Figure		Page
5.13	Same as in Fig. 5.3 except for 6.75 km	88
5.14	Same as in Fig. 5.4 except for 6.75 km	90
5.15	Same as in Fig. 5.5 except for 6.75 km	91
5.16	Vertical profiles of terms HFD, VFD and TFD (as in 4.18)	92
5.17	The vertical distribution of mean vertical kinetic energy transport	94
5.18	Same as in Fig. 5.16 except for terms VGE, BUP and TFD	95
5.19	Same as in Fig. 5.16 except for terms HGE, FDI and LTK	97
5.20	Vertical profiles of the three mean wind components, U, V and W, averaged over the domain of interest	103
5.21	Vertical profiles of the vertical transports of horizontal momentum for the u-component, averaged over the domain of interest	106
5.22	Same as in Fig. 5.21 except for the v-component	108
5.23	The vertical cross-section showing (a) system-relative wind with reflectivity contours Z superimposed and (b) vertical velocity, w	109
5.24	Vertical profiles of the dominant terms in the momentum-flux budget for the u-component, $\overline{u'w'}$, averaged over the domain of interest	113
5.25	Same as in Fig. 5.24 except for the v-component	117
5.26	Plan view of horizontal vorticities ($\hat{i}\xi + \hat{j}\eta$) with vertical velocity, w , contours superimposed at 0.75 km for 0700 LST 25 June 1987	120
5.27	Plan view of the vertical vorticity, ξ , field superimposed on the system-relative horizontal wind field at 0.75 km for 0700 LST 25 June 1987	121
5.28	Same as in Fig. 5.26 except for 3.75 km	124

Figure		Page
5.29	Same as in Fig. 5.27 except for 3.75 km	125
5.30	Same as in Fig. 5.26 except for 6.75 km	127
5.31	Same as in Fig. 5.27 except for 6.75 km	128
5.32	The mean horizontal vorticity vectors ($i\bar{\xi} + j\bar{\eta}$) determined from $\bar{\xi}$ and $\bar{\eta}$ values contained in Table 6	131
5.33	Horizontal distributions of the horizontal advection (HAD) of the x-component of vorticity, ξ , at 3.75 km for 0700 LST 25 June 1987	134
5.34	Horizontal distributions of the vertical advection (VAD) of the x-component of vorticity, ξ , at 3.75 km for 0700 LST 25 June 1987	135
5.35	Horizontal distributions of the divergence/convergence (DIV) of the x-component of vorticity, ξ , at 3.75 km for 0700 LST 25 June 1987	136
5.36	Horizontal distributions of the tilting/tipping (TILT) of the x-component of vorticity, ξ , at 3.75 km for 0700 LST 25 June 1987	138
5.37	Same as in Fig. 5.36 except for 0.75 km	139
5.38	Same as in Fig. 5.33 except for the y-component of vorticity, η	140
5.39	Same as in Fig. 5.34 except for the y-component of vorticity, η	141
5.40	Same as in Fig. 5.35 except for the y-component of vorticity, η	143
5.41	Same as in Fig. 5.36 except for the y-component of vorticity, η	144
5.42	Same as in Fig. 5.33 except for the z-component of vorticity, ζ	145

Figure		Page
5.43	Same as in Fig. 5.34 except for the z-component of vorticity, ζ	147
5.44	Same as in Fig. 5.35 except for the z-component of vorticity, ζ	148
5.45	Same as in Fig. 5.36 except for the z-component of vorticity, ζ	149
5.46	Vertical profiles of the vorticity budget terms for the x-component averaged over the domain of interest	154
5.47	Same as in Fig. 5.46 except for the y-component	156
5.48	Same as in Fig. 5.46 except for the z-component	157

Chapter 1

Introduction

Over the past several decades, the mountainous island country of Taiwan has experienced a number of flash floods resulting in a substantial amount of property damage. Each of two events in June of 1984 caused between 400-600 million U.S. dollars in losses to the Taiwanese economy (Chen and Kuo, 1991). Most of the floods occurred late spring and early summer in what is known to the natives as the Mei-Yu season. A transition phase occurs between the Asian northeast monsoon and southwest monsoon flow regimes that plays a key role in affecting the weather in China, Taiwan and Japan during the late spring and early summer. During this transition period, a quasi-stationary front forms in the deformation wind field along the boundary between the migratory high to the north and the Pacific high to the south (Chen, 1983). This front is commonly referred to as the Mei-Yu front in China and Taiwan and the Baiu front in Japan.

The Mei-Yu front is a highly active weather-producing phenomenon. The mesoscale convective systems (MCSs) triggered by and/or along the front are difficult to study using conventional data alone. With the awareness that the prediction of flash floods is greatly hampered by a lack of data and lack of understanding of the mesoscale processes responsible for producing heavy rainfall, in 1985 the National Science Council (NSC) of the Republic of China (ROC) in Taiwan (the peer organization to the National Science Foundation in

the United States) established a mesoscale meteorological research program designated as the Taiwan Area Mesoscale Experiment (TAMEX). In the interest of science, the United States joined Taiwan scientists in this endeavor. During May and June of 1987, the field phase of TAMEX was conducted to investigate: 1) the mesoscale circulation of the Mei-Yu front; 2) the evolution of mesoscale convective systems in the vicinity of the Mei-Yu front; and 3) the effects of orography on the Mei-Yu front and on mesoscale convective systems. The long range operational goal of TAMEX is to improve the forecasting of heavy precipitation events that could lead to flash floods by better understanding the dynamic and physical processes involved (Kuo and Chen, 1990).

In order to meet the objectives of the program, an extensive observational network was established in a highly concerted and coordinated effort. This mesoscale network nearly covered the entire island of Taiwan and surrounding small, coastal islands. Scientists from both participating countries were tasked to monitor an array of meteorological instruments and observing sites that consisted of: 1) 12 rawinsonde sites; 2) 10 pibal sites; 3) 126 rain gauges; 4) 75 surface stations; 5) 21 wind towers; 6) three 5-cm Doppler radars and five conventional radars; 7) one VHF wind profiler; 8) three research vessels; 9) one satellite station capable of ingesting data from Japan's GMS-3 geo-stationary satellite and two NOAA polar orbiting satellites; and 10) one P-3 research aircraft (Kuo and Chen, 1990). The three 5-cm Doppler radars were stationed along the northwest coast of Taiwan (Fig 1.1), including the CAA (Civil Aero-

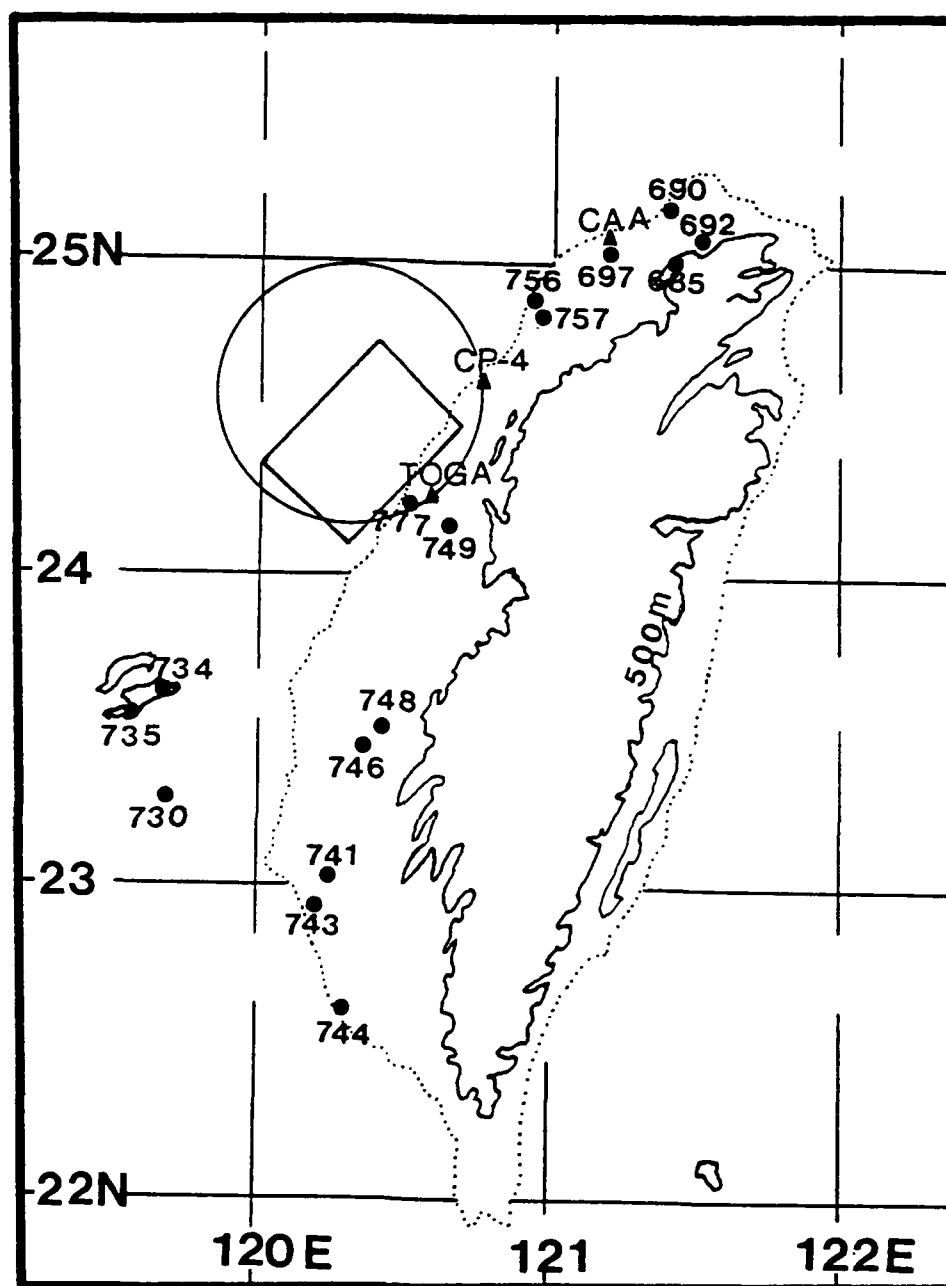


Fig 1.1 TAMEX Doppler network identifying the locations of the CAA, CP-4 and TOGA radars. The circle signifies the dual-Doppler coverage area of the CP-4 and TOGA radars. The box represents the data domain of this study. Numbers represent the location of several observing stations within the TAMEX network. The dotted line outlines Taiwan's coastline and the solid line contours elevations 500m or higher representing the CMR.

nautic Administration), the NCAR (National Center for Atmospheric Research) CP-4 and the TOGA (Office of Tropical Oceans and Global Atmosphere) radars. These radars were strategically positioned so they could provide the best possible coverage, including dual-Doppler coverage, of the approaching weather systems. With this type of network and the outstanding coordinated effort, the field program was highly successful. The program ran from 1 May to 29 June 1987 and experienced 13 intense observing periods (referred to as IOPs). During these IOPs, data were collected more frequently in order to provide the best temporal coverage of the occurring event.

Perhaps the most widely studied IOP during TAMEX is IOP-13. This late season event brought a tremendous amount of precipitation to central Taiwan, especially in the Taichung (749) area where around 175 mm of rainfall (nearly 6.6 inches) was recorded in a 10 hour period. When TAMEX data became readily available, many researchers have extensively studied the kinematics, dynamics and thermodynamics associated with IOP-13. Lin *et al.* (1992), Beeson (1991) and Miglioranza (1992) in separate studies involving both single- and dual-Doppler radar data sets discovered many important features about the front and the convective rainband associated with it during IOP-13. Significant findings include: 1) the convective rainband was about 5-10 km wide and 50 km long and was a prefrontal rainband; 2) the ENE-WSW oriented front was shallow in depth, the cool and drier air was generally less than 2 km, and it moved very slowly, about 2.5 m s^{-1} ; and 3) convection was deep but moderate

with maximum updraft velocities less than 10 m s^{-1} in a broad area ahead of the front. These updrafts exhibited a downstream tilt along the normal axis toward the southeast thus allowing precipitation and cool downdrafts to occur where they did not inhibit the flow of moisture rich air from the southwest into the system, thus, allowing for new convection to take place. Chang (1992) studied several dynamic and thermodynamic features of the IOP-13 case. He found that the retrieved pressure and temperature fields were closely related to each other and were nearly in hydrostatic balance at low levels. He also found that vertical transports of horizontal momentum normal to the rainband were upward, probably due to the southeast-tilt of convective updrafts ahead of the Mei-Yu front. This feature is different from that observed in a subtropical squall line during IOP-2 (Wang *et al.*, 1990; Lin *et al.*, 1990).

It is important to pursue further the study of the dynamics and thermodynamics of the convective rainbands during IOP-13. Budget studies of several types can be determined using the dual-Doppler data from TAMEX. Such studies would help gain further insight into the internal structure of the rainbands and their dominant processes and how these processes could influence the Mei-Yu front and its environment. This research is concerned with three important meso- γ -scale budget studies: 1) the total kinetic energy budget; 2) the momentum-flux budget; and 3) the vorticity budget. Dual-Doppler observations centered at 0653 and 0700 LST (local standard time) on 25 June 1987 will be used in deriving the horizontal system-relative wind components at ten

levels. The horizontal domain of $25 \times 40 \text{ km}^2$ is chosen so that the prefrontal convective rainband is adequately covered by the TOGA and CP-4 Doppler radars. Vertical velocities are derived from the anelastic continuity equation by integrating downward from the top. The three momentum equations are used to retrieve fields of deviation pressure and temperature using the thermodynamic retrieval method of Gal-Chen (1978). From this information, the aforementioned budgets are calculated.

The main objective of this research is to study and determine the important processes controlling the three budgets and how those processes influence the Mei-Yu front and its surroundings. The overall goal is to gain better understanding of the structure and dynamics of the prefrontal convective rainband during IOP-13.

Chapter 2

Literature Review

A review of previous studies pertaining to the three types of budgets analyzed in this thesis research is contained in this chapter. It is important to gather as much information about each subject in order to gain insight. Although methods and types of meteorological events studied may be different from the one I analyzed, it helps provide basic information needed to assist in this research. I will first discuss studies related to kinetic energy, then momentum flux and finally vorticity budgets.

2.1 Kinetic Energy Budget Studies

Only a limited number of studies exist in literature that describe how intense convection modifies the mesoscale environment. This is mainly because the upper air data sets were primarily rawinsonde data sets, which usually only provided spatial resolution on the meso- α -scale and only with exception on the meso- β -scale. One earlier mesoscale study examined how large areas of convection influence the larger synoptic-scale kinetic energy amounts. Kung and Tsui (1975, 1977) studied the meso- α -scale storm environment using rawinsonde data from the National Severe Storms Laboratory (NSSL). Their findings showed that environments containing intense convection were characterized by large generation and dissipation of kinetic energy mainly at the jet stream level. In contrast, they found that in non-convective areas, there

was large destruction of kinetic energy due to transfer of energy from the sub-grid to grid scales of motion. As finer resolution data sets became available for the study of mesoscale motions, kinetic energy studies became much easier to determine and analyze.

Two major projects in the late 1970s, the Atmospheric Variability Experiments (AVE) and the AVE Severe Environmental Storms and Mesoscale Experiments (AVE-SESAME) provided these much needed finer scale data sets. Fuelberg and Scoggins (1978) used AVE IV rawinsonde data in computing the kinetic energy balance of a Mesoscale Convective Complex (MCC). They found that large energy changes in the storm environment were due to several factors: 1) generation of kinetic energy by cross-contour flow; 2) horizontal flux divergence at the jet stream level; and 3) upward transport of kinetic energy due to large scale upward motion. From AVE-SESAME data collected during a tornado outbreak in the Red River Valley, Fuelberg and Printy (1984) showed that the convective environment was energetically very active when compared to the entire storm domain. Their study emphasized the importance of studying the kinetic energy balance at these finer scales of motion.

Lin and Coover (1988) analyzed the kinetic energy budget of a microburst-producing thunderstorm during the 1982 Joint Airport Weather Studies (JAWS) project using dual-Doppler derived winds and retrieved thermodynamic fields. Their data set provided a spatial resolution of 0.5 km in both the horizontal and the vertical. They evaluated each term of the kinetic

energy equation by taking an ensemble mean in the storm domain. Results showed that the horizontal generation and horizontal flux divergence were main sources of kinetic energy, while dissipation was the main sink. The vertical generation and total buoyancy production terms had the same order of magnitude but were opposite in sign at most levels. The vertical flux divergence and horizontal flux divergence terms were nearly in balance at all levels. Transport of kinetic energy was found to be downward in the lower levels, where the microburst dominated, and upward in the middle and upper levels, where the storms strong convective updrafts were dominant.

Using TAMEX data collected during IOP-2, Lin *et al.* (1991) studied the kinetic energy budget of a subtropical squall line located over the Taiwan Strait. They determined the budget using similar methodology to Lin and Coover (1988) except the grid spacing was 1.0 km in all directions instead of 0.5 km. Results showed that, at most levels, horizontal flux divergence (convergence) of kinetic energy was nearly balanced by the vertical flux convergence (divergence). The horizontal generation term and the total buoyancy production term acted as sources of kinetic energy, while the dissipation term and the vertical generation term were sinks.

2.2 Momentum-flux Budget Studies

Deep convection tends to be organized into lines. These lines can increase or decrease the wind shear depending upon their structure (e.g.,

LeMone and Jorgensen, 1991). Thus, how momentum is transported within a convective line is of particular interest. It shows how the system may affect the large-scale dynamics. Several studies investigate momentum fluxes within several types of MCSs.

LeMone (1983) investigated the momentum transport by a line of cumulonimbus off the coast of west Africa using aircraft observations taken during the GARP (Global Atmospheric Research Program) Atlantic Tropical Experiment (GATE). She found that the vertical transport of horizontal momentum parallel to the axis of the convection band was along the vertical momentum gradient as predicted by mixing length theory. However, the vertical transport of horizontal momentum normal to the line was found to be against the vertical momentum gradient, thus making it contrary to the mixing length theory. Furthering her own study, LeMone *et al.* (1984) determined that the mesoscale tropical convective line increased front-to-rear momentum at heights above 4 km and increased rear-to-front horizontal momentum below 4 km. The vertical transport of horizontal momentum parallel to the convective line was downgradient and the vertical flux of horizontal momentum normal to the line was independent of the vertical shear of the horizontal wind.

Rao and Hor (1991) studied an eastern Arabian Sea convective band's momentum fluxes using aircraft data gathered by NCAR's Electra on 24 June 1979. Their findings were similar to those of LeMone *et al.* (1984). Additionally, Rao and Hor (1991) determined the budgets and found that the dominant

terms were found to be the vertical shear, the buoyancy and the pressure terms. The buoyancy term produced negative u-momentum flux ($\overline{u'w'}$) following the sign of $\overline{u'w'}$, while vertical shear provided a positive flux. Pertaining to the v-momentum flux $\overline{v'w'}$, the buoyancy and vertical shear terms exhibited similar vertical profiles, positive flux below the low-level westerly jet (LLWJ) and negative above the LLWJ. The ability to determine perturbation winds, like u' , from the rapid accumulation of observations using aircraft equipped with highly sensitive instruments made these studies possible. Unfortunately, this method is quite expensive. However, with the availability of Doppler radar data becoming more and more a reality, studies can be accomplished at a more frequent rate and be accomplished on the meso- γ -scale.

Lin and Condray (1988) calculated the momentum-flux budget of a middle latitude microburst-producing storm observed during the JAWS project. The dominant processes contributing to the generation/dissipation of horizontal momentum flux were total buoyancy production, pressure effects, vertical mean wind shear and vertical transport of momentum. The buoyancy and pressure terms dominated in the low levels where the microburst prevailed. Conversely, above 1 km, the shear and transport terms became more significant. Overall, they found that the buoyancy and pressure terms tended to balance each other and likewise, the transport and shear terms were in balance. Another study involving dual-Doppler derived parameters, Lin *et al.* (1991) studied the momentum-flux budget of a subtropical squall line during TAMEX

IOP-2. Using procedures similar to those described in Lin and Coover (1988), they found the same four processes dominated the momentum-flux budget of their case. In the horizontal momentum flux normal to the squall line ($\overline{u'w'}$), the pressure and buoyancy terms were nearly in balance at all levels of the system. They also found that the shear production term was well balanced by the vertical transport term. Total buoyancy production acted as an overall sink for $\overline{u'w'}$ generation in the lower and middle levels, while the pressure term was the main source. The reverse was true for the $\overline{v'w'}$ flux, the parallel component.

2.3 Vorticity Budget Studies

Vorticity budgets have been used in studies of extratropical and tropical weather systems for many years. Most of these studies were conducted using specialized data sets from various meteorological field experiments.

Stevens (1979) analyzed the vorticity budget for the average synoptic-scale wave using composited data from Phase III of GATE. He expanded the vorticity equation in pressure coordinates and separated the budget of mean vorticity and that for the wave component by decomposing the synoptic fields into time mean and time varying portions. The dominating forces of the mean vorticity budget were the advection of mean vorticity by the three-dimensional wind, the advection of planetary vorticity by the mean wind and the divergence of the mean motion. The tilting/tipping term was much smaller in magnitude than the other terms. The divergence term was a large sink of vorticity

in the lower levels, while in the upper levels the advection and divergence terms were sources. Townsend and Scoggins (1983) studied the vorticity budget of several middle latitude convective areas using the NASA's AVE VII and AVE-SESAME I data sets. They found in almost all of their cases they analyzed that, on the synoptic scale, the horizontal advection and the divergence terms of vorticity were the dominating processes contributing to the production/destruction of vorticity. The horizontal advection term exhibited positive vorticity advection aloft in the convective areas and negative vorticity advection in the non-convective areas. The divergence term underwent the greatest vertical change with convergence in the lower levels and divergence in the upper levels within the convective areas and vice versa in the non-convective areas. Once again, the tilting/ tipping terms contribution was negligible.

Douglas (1992) calculated the vorticity budget of two tropical depressions observed during the Summer Monsoon Experiment (SMONEX). Expanding the vorticity equation in isobaric coordinates, he determined the budget in terms of horizontal advection of absolute vorticity (HADV), the generation of vorticity by convergence/divergence (DIVTM), the vertical advection of absolute vorticity (VADV), the generation of vorticity by horizontal gradients of vertical motion in the presence of vertical shear (the tilting term, TILTT), and a residual term due to surface friction and sub-grid scale processes. The last term, Z as he called it, was determined to be smaller in magnitude than the other terms. In both cases, DIVTM was a large source of vorticity generation

due to strong convergence (divergence) in the low and middle levels (upper level) and HADV was generally smaller than DIVTM and opposite in sign. VADV and TILTT were both small below 700 mb but increased with height reaching maximum values near 400 mb. In both cases, they were opposite in sign and in near balance at most levels. Because of the mean upward motion over the rain areas, VADV contributed negatively to the vorticity tendency below the vorticity maxima (near 600 mb) and positively above.

In two separate studies using JAWS data, Lee *et al.* (1992) and Lin and LaPointe (1991) determined vorticity budgets of a bow-echo-microburst event and a multiple microburst-producing storm, respectively, using dual-Doppler derived winds. Lee *et al.* (1992) found that a vertical vorticity couplet was generated primarily through the tilting of ambient horizontal vorticity by the microbursts downdraft. The positive vorticity was enhanced by both the stretching effect (due to the divergence term) and the downward advection of positive vorticity from aloft that was produced by the updraft through the same mechanism. Lin and LaPointe (1991) computed the vorticity budgets of all three vorticity components by expanding the vorticity equation in z -coordinates. The friction term was found to be one order of magnitude smaller than the other terms and the solenoid term was not computed in the budget study due to the higher uncertainty of the retrieved information derived from the dual-Doppler winds. Thus, only the derived wind information was needed and used for their study. They studied the vorticity budget within the domain

of the system and within the domain of the microburst. Within the microburst domain, results showed that for the x-component of vorticity (ξ), the horizontal advection term (HAD) acted as a sink, while the vertical advection term (VAD), the divergence term (DIV) and the tilting/tipping term (TILT) were all sources. For the y-component of vorticity (η), HAD and VAD were overall sources and TILT and DIV were sinks. For the z-component of vorticity (ζ), VAD and TILT dominated the budget with VAD the main source and TILT the main sink. Thus, in their detailed study, the authors were able to assess the vorticity budget in terms of all three components of vorticity. In these last two studies, the tilting term became an important factor in the generation/destruction of vorticity on the meso- γ -scale.

It is easy to see from this brief yet detailed review of applicable literature that the various budgets and the forces that dominate within them are highly dependent upon the data set used, the scale of motion of the interested event and the methodology used in their determinations.

Chapter 3

Environmental Summary

TAMEX IOP-13 began at 14 UTC (Coordinated Universal Time) or 22 LST (local standard time) on 24 June 1987 and it lasted for nearly 25 hours. This chapter is a summary of the environmental conditions and features associated with IOP-13.

3.1 Synoptic Conditions

Several researchers (Beeson, 1991; Chang, 1992; Miglioranza, 1992) have presented highly-detailed discussions describing the synoptic conditions associated with this event. They depict numerous synoptic-scale surface and upper air charts that aid in their discussions. Only a brief description of the synoptic conditions will be presented here. For complete details, see the above-mentioned papers.

The synoptic conditions that triggered IOP-13 showed that a low pressure center was located to the southwest of Japan at 12 UTC 24 June. A cold front extended from this low southwestward into southeast mainland China. Ahead of this west-to-east oriented front a southwest low-level jet (LLJ) of 15 m s^{-1} prevailed over the northern tip of Taiwan. Warm, moist air was being advected from the southwest by monsoon flow. Upper levels displayed a large diffluent zone over the Taiwan Strait. Coupled with low-level confluence, the synoptic

conditions were highly favorable for development of convective activity within the warm sector. This front moved slowly southward over a 30 hour period and developed a prefrontal convective rainband, which caused a massive amount of precipitation on the west coast of Taiwan. The central mountain range (CMR) of Taiwan caused the front to split into two parts. Figure 3.1 (a) shows approximate positions of the Mei-Yu front (solid lines) in 3-h intervals. The interior hatched contours represent the CMR. The solid lines in Fig. 3.1 (b) depict the position of the squall-line gust front in hourly increments (LST) as the leading edge of the squall line slowly progressed southward during IOP-13. The dotted line outlines Taiwan's coastline and the solid thin line within the interior represent elevations of 500 meters or greater within the CMR. The circle encompasses the dual-Doppler radar coverage area for the TOGA (T) and NCAR CP-4 (N) radars. Positions of the Mei-Yu front and the gust front (GF) were determined by careful analysis of surface observations in 30-min intervals from the TAMEX network.

3.2 Satellite Display

Figure 3.2 shows a series of infrared (IR) imagery from Japan's Geostationary Meteorological Satellite (GMS) beginning at 0200 LST 25 June. Observe the east-to-west oriented band of smaller MCSs just north of Taiwan. By 0800 LST, the MCS that was near northern Taiwan had grown and covered the entire island of Taiwan. This MCS caused extremely heavy precipitation

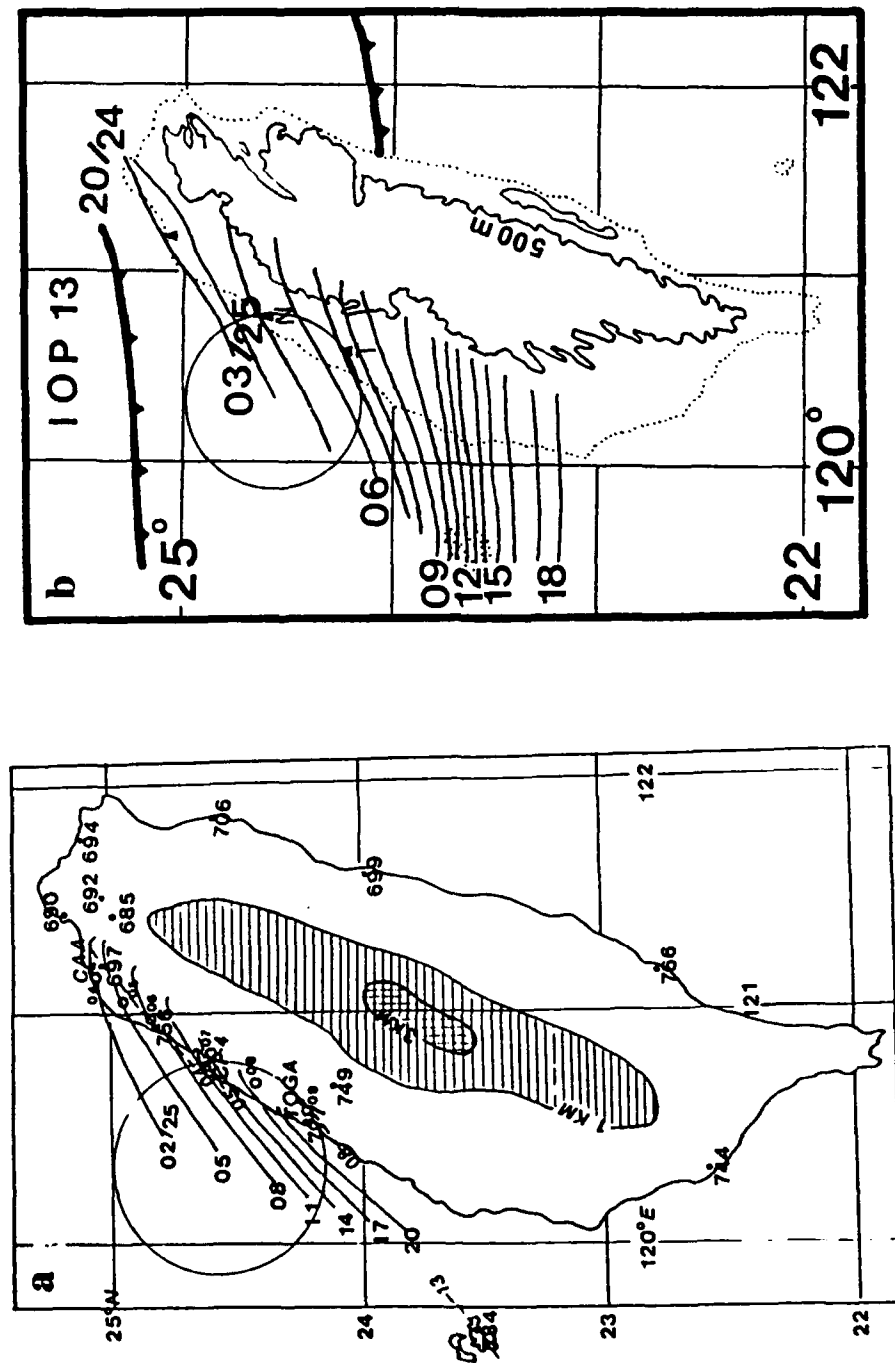


Fig. 3.1 Progressive positions of the (a) Mei-Yu front from 0200 to 2000 LST 25 June in 3-h intervals (after Lin *et al.*, 1993) and (b) the squall-line gust front (GF) from 0300 through 1800 LST 25 June 1987 in hourly intervals. The position of the Mei-Yu front at 2000 LST 24 June is also shown in (b). The circle denotes dual-Doppler coverage area of the CP-4 (N) and TOGA (T) radars.

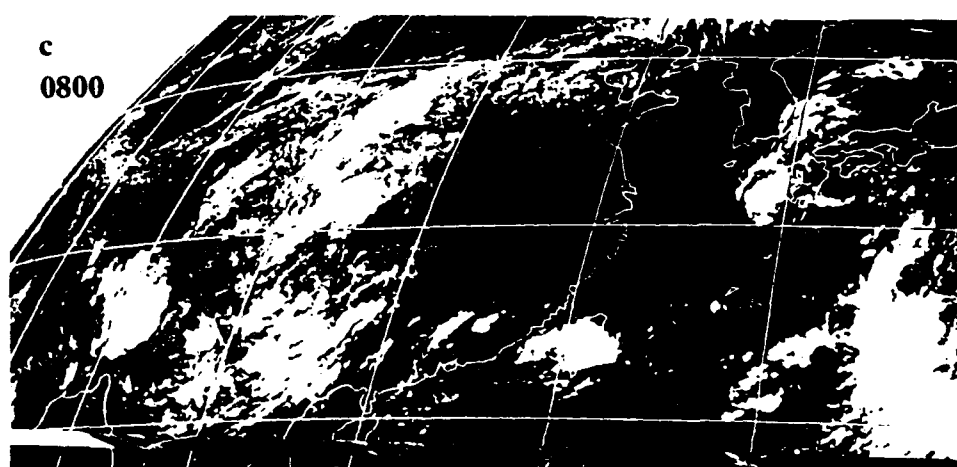
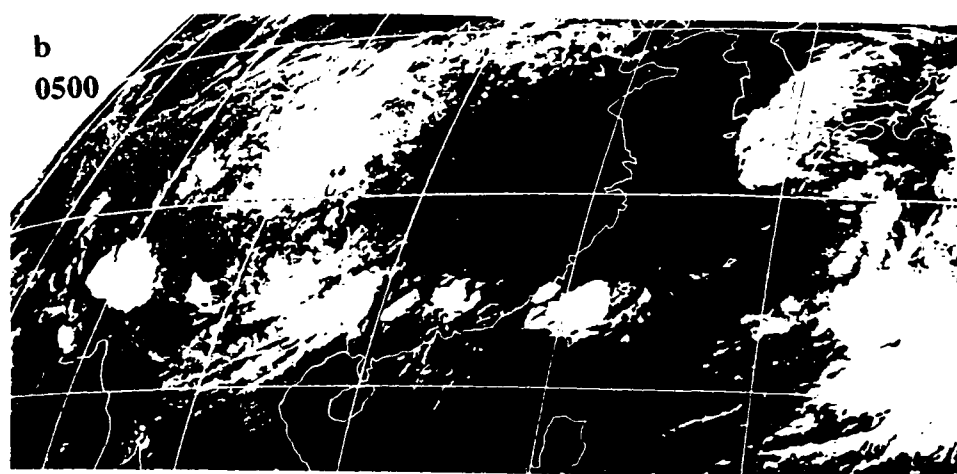
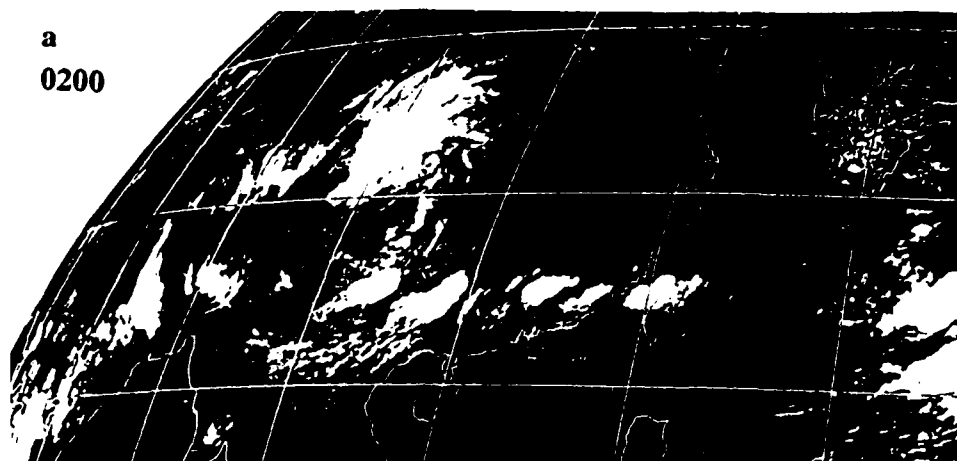


Fig 3.2 IR imagery from Japan's GMS satellite for (a) 0200 LST, (b) 0500 LST and (c) 0800 LST on 25 June 1987.

(Chiou, 1990) over northern Taiwan. Chi and Scofield (1991) observed the following satellite features. A Mei-Yu front signified the synoptic-scale boundary. The coldest cloud tops were in the northern portion of the MCS with anvil debris in the southern area of the MCS. The MCS produced an out-flow boundary which interacted with the surface front. Convergence was enhanced by the southerly winds at the surface. The heaviest convection occurred on the west coast of Taiwan.

3.3 Surface Observations

The conventional surface network immediately began taking observations at 30-min intervals after IOP-13 commenced. With this volume of data available for analysis, several features can be determined with an excellent confidence level in their accuracy. Figure 3.1 is one example. Figures 3.3 and 3.4 show several meteorological parameters at several surface stations located throughout the western portion of Taiwan. The GF and F (and their associated arrows) represent the passage of the gust front and Mei-Yu front, respectively, during IOP-13 at the specific location. The numbers in the parentheses are the station code identifiers (minus the first two digits of 46) and location of these can be found on Fig 1.1 as well as on several figures presented throughout this thesis.

I will begin by looking at the observations of the northern most stations, shown in Fig 3.3, since the front (F) and gust front (GF) approached the island

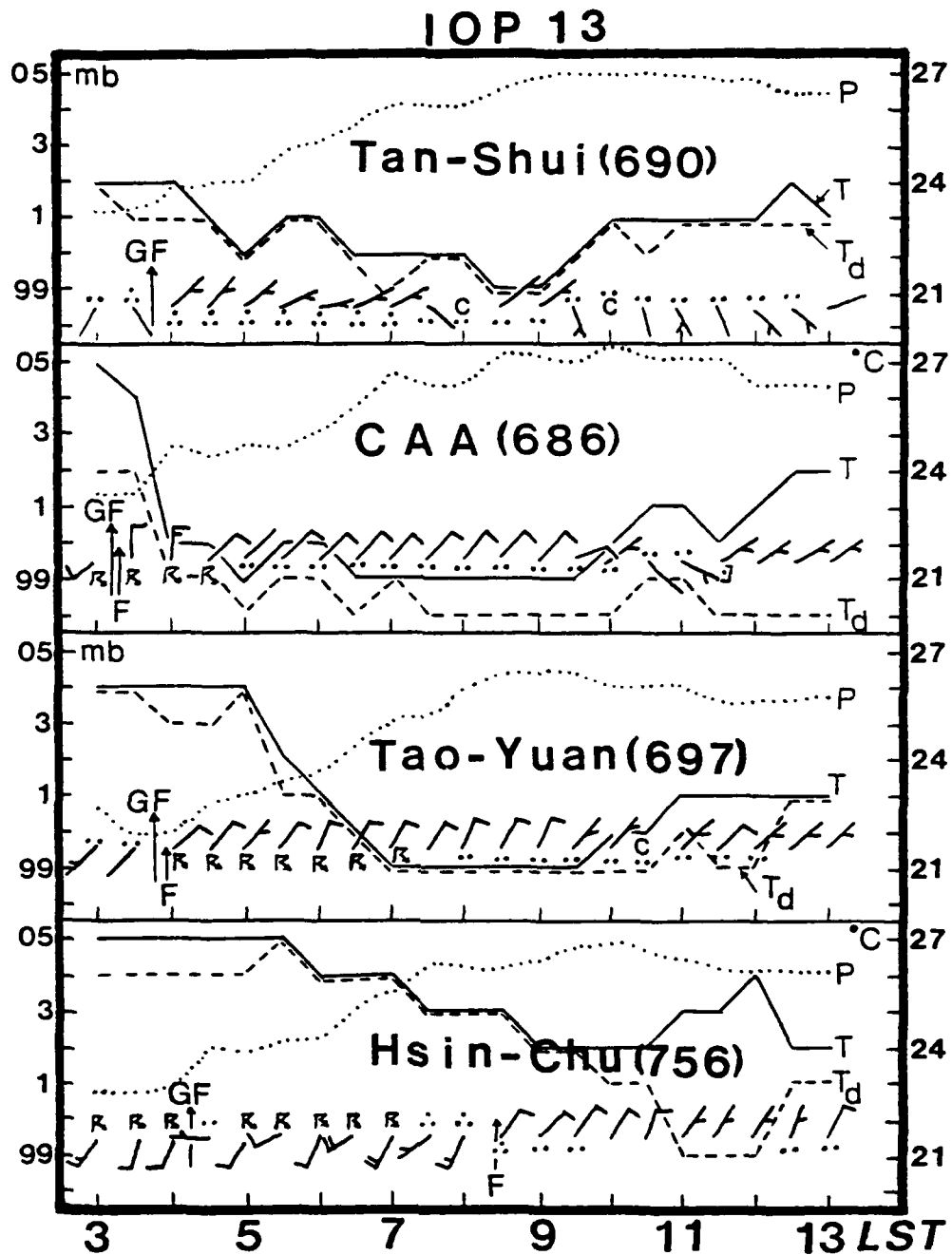


Fig 3.3 Surface observations reported at several northern Taiwan stations on 25 June 1987. Displayed are wind direction, wind speed in knots, pressure in mb (dotted line), temperature in °C (solid line), dewpoint temperature in °C (dashed line), and significant weather. The GF and F (and corresponding arrows) represent passage of the gust front and Mei-Yu front at that location.

from the northwest. Tao-Yuan (697) observations depict GF and F passage almost simultaneously at 0400 LST 25 June. There was a rapid wind shift from southwesterly winds to northeasterly winds and convective activity did not commence until after the passage of the cold front. Both temperature (T) and dewpoint temperature (T_d) decreased by nearly 5°C within three hours of frontal passage. Pressure (P) rose steadily after frontal passage and increased nearly 4 mb. Dewpoint depression did not decrease until 6-8 hours after the Mei-Yu front passed, thus it took several hours for the low- θ_e air from northern China to arrive. Turning our attention 40 km to the southwest, we can visualize the features at the Air Force Hsin-Chu station (756). Immediately we can see a distinct difference from the Tao-Yuan observations. The gust front passed Hsin-Chu about a half hour later (0430 LST) but the front did not pass until about 0830 LST, a four hour difference from Tao-Yuan despite the close proximity of the two stations. Southwest flow was able to feed moisture-rich air along the gust front, thus enabling convection to sustain itself for nearly three hours. Upon frontal passage, we see the wind shift in a similar fashion to the Tao-Yuan station. There was only a gradual decrease of 3°C in T and T_d from gust front passage until one hour after frontal passage. However, it took two hours after frontal passage before the dewpoint depression dropped significantly ($4\text{-}5^\circ \text{C}$).

West coast stations of central Taiwan are represented in Fig 3.4. Note that the time along the x-axis are later times than those in Fig 3.3. Wu-Chi (777) is

located right along the coast and displays several interesting features. The gust front passage and the Mei-Yu front passage were nearly 15 hours apart with convection lasting only a couple of hours. However, several reports of heavy rain after the convective activity ceased indicates substantial moisture advection into the system thus enhancing heavy precipitation. Temperature, dewpoint temperature and dewpoint depression all maintained a quasi-steady observation until the frontal passage. Ching-Chung-Kang, commonly referred to as CCK (770), is where the TOGA radar is located. This station is slightly farther inland than Wu-Chi. The gust front passed at about 0730 LST with convective activity being reported for nearly six hours. Like at Wu-Chi, frontal passage was about 15 hours after the gust front passage. Persistent strong southerly winds (nearly 20 knots) obviously transported moist air into the convective area, enhancing the chance for new cells to develop ahead of the front. At Tai-Chung (749), convection preceded gust front passage (at 0845 LST) but heavy rains were consistently reported for five hours. Thus leading to the credence that it was the slow movement and the persistent rains leading to flash floods and not the intensity of the convection (Lin *et al.*, 1992).

Looking at two coastal island stations over the strait, Peng-Hu (735) and Tung-Chi-Tao (730), notice that the gust front passage and the Mei-Yu front passage were much closer together than at the central stations (only 4-5 hours apart). Most likely the speed of the front was not influenced as much by the CMR in these locations. Especially note the lack of convective activity and

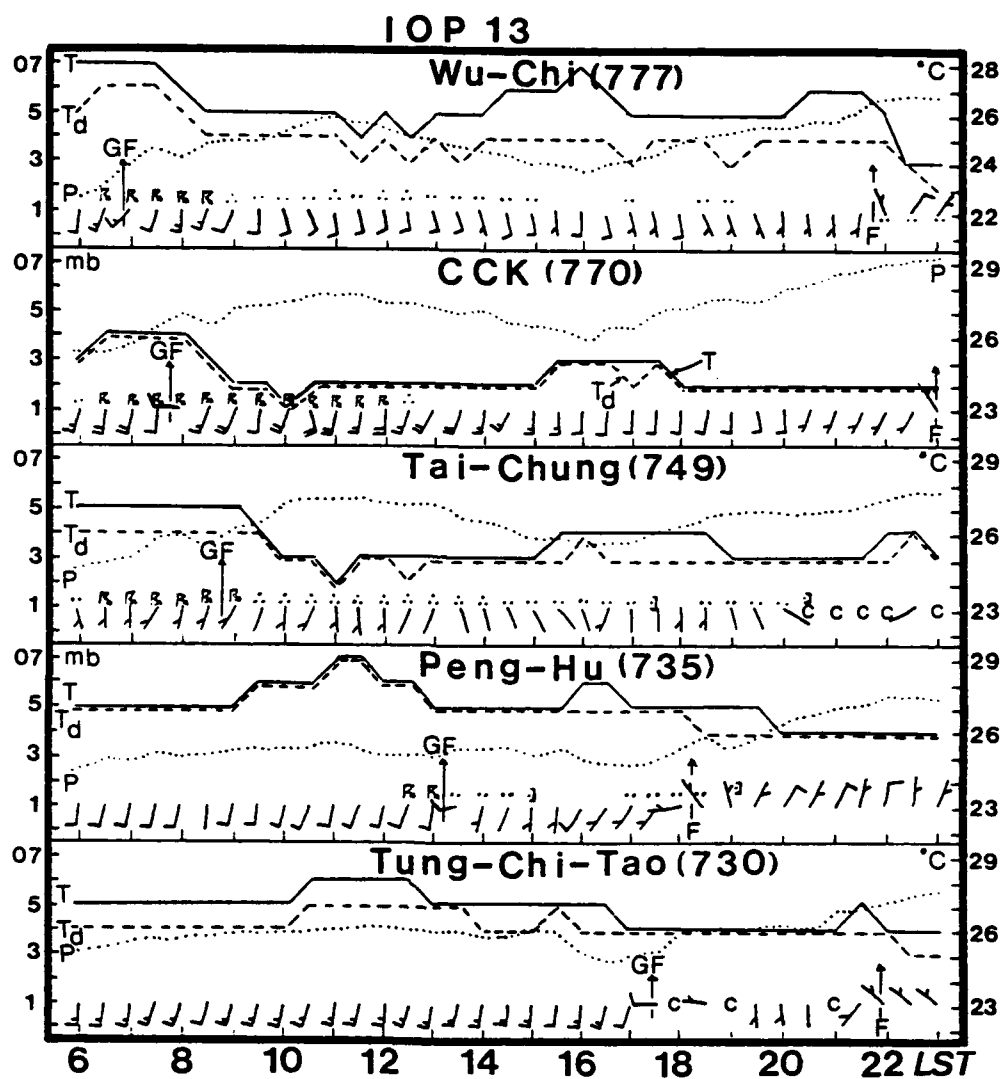


Fig 3.4 Same as in Fig 3.3 except for central west coast and coastal island stations.

the overall short duration of the precipitation. Temperature, dewpoint temperature and pressure all remained steady throughout the passage of the system indicating that the southern portion of the front underwent more air mass modification than the other regions.

A synopsis of 16 TAMEX surface stations is contained in Table 1. The stations are displayed such that as you read down the table, you are heading south in direction pertaining to the location of each station. It is interesting to note the time differential between gust front and Mei-Yu front passage between the northern and the central stations. The gust front progressed steadily southward along the coast, while the front moved much slower. As an example, time after the gust front passage at all stations except the northern most where wind direction shifted about 180 degrees. Table 1 also indicates that southerly winds dominated thus enabling moist air to feed the system. Temperature changes were almost null after gust front passage but there was generally a 2-5 ° C drop in temperature after the front passed, which indicates there was not a strong temperature gradient across this Mei-Yu front.

3.4 Vertical Characteristics

Vertical profiles of several features can give us a good idea of what is taking place in the atmosphere. Upper air soundings were simultaneously released at 0200 LST 25 June at Makung and Pan-Chiao in order to capture features of the prefrontal and postfrontal environmental conditions associated

Table 1

Synoptic characteristics of TAMEX IOP-13 25 June 1987.

Station Name	Station Code	Passage (LST)		Surface Traces during Squall Passage				
		Squall line (GF)	Mei-Yu front	Wind dir	Wind S (m/s)	Pres (mb)	Temp (°C)	Sig Wea
Tan-Shui	46690	0345	---	SE→NE	1→3	01.2→01.9	24→24	••
CKS Airport (CAA)	46686	0315	0330	SW→N	3→5	01.4→02.7	27→26	℞
Tao-Yuan	46697	0400	0415	SW→NE	2→5	99.9→00.7	26→26	℞
Hsin-Chu (AF)	46756	0415	0830	SW→W	5→3	00.8→01.9	27→27	℞
Hsin-Chu	46757	0445	0915	SSW→SW	2→3	00.7→01.6	27→26	℞
CP-4	---	0530	1300	SW→W	---	---	---	℞
CCK (TOGA)	46770	0745	2300	SSW→W	4→7	04.0→04.8	26→26	℞
Wu-Chi	46777	0700	2145	SSW→SW	6→8	02.6→03.5	28→28	℞
Tai-Chung	46749	0845	---	SSW→SW	2→3	03.5→04.4	27→27	℞
Ma-Kung	46734	1300	1800	SSW→SW	5→6	03.0→03.6	27→27	℞
Peng-Hu	46735	1315	1815	SSW→SW	5→6	03.0→03.3	27→27	℞
Tung-Chi-Tao	46730	1700	2200	SW→W	5→6	02.9→03.9	26→26	••
Chia-Yi (AF)	46746	1615	---	S→SSW	2→3	03.7→03.8	28→28	℞
Chia-Yi	46748	1600	---	SSE→S	2→3	03.0→03.4	28→28	••
Tai-Nan	46741	2200	---	WSW→S	2→3	05.0→05.2	27→27	••
Tai-Nan (AF)	46743	2245	---	WSW→S	2→3	05.1→05.4	28→27	••

with IOP-13. The Makung (734) station is located in the Taiwan Strait where the influence of topography is minimal. In contrast, Pan-Chiao (685) is located over northern Taiwan near the city of Taipei and is surrounded by mountains with heights varying from 250 to 1000 m. Figures 3.5 and 3.6 display these prefrontal (Makung) and postfrontal (Pan-Chiao) upper air soundings. The Makung sounding (Fig 3.5) indicates that veering of the winds with height occurred through a deep layer thus large-scale warm air advection was likely occurring. The low level was fairly moist and the middle level was somewhat drier, representative of a conditionally unstable type sounding. Using parcel theory, lifting an unsaturated air parcel to its lifting condensation level (LCL) and then continuing to lift the same air parcel (which is now saturated) to its level of free convection (LFC), we find the LFC to be approximately at 800 mb. Following the dotted line, which represents the saturated parcel's moist adiabat, the parcel is free to ascend to its equilibrium level (EL), near the 150 mb level. The area between the dotted line bounded by the LFC and EL and the environmental sounding is essentially the storm's convective available potential energy (CAPE). CAPE can be defined as the amount of buoyant energy available to a parcel rising through an undisturbed environment. Magnitudes of CAPE can be as large as $4500 \text{ m}^2 \text{ s}^{-2}$ but generally range between 1500 and $2500 \text{ m}^2 \text{ s}^{-2}$ for moderately unstable convective environments. A CAPE value of $2500 \text{ m}^2 \text{ s}^{-2}$ could translate to a maximum possible updraft strength (including water loading, perturbed vertical pressure gradients, and mixing effects) of 35 m s^{-1} (Weisman and Klemp, 1986). The value of CAPE

Makung 0200 LST 25 June 1987

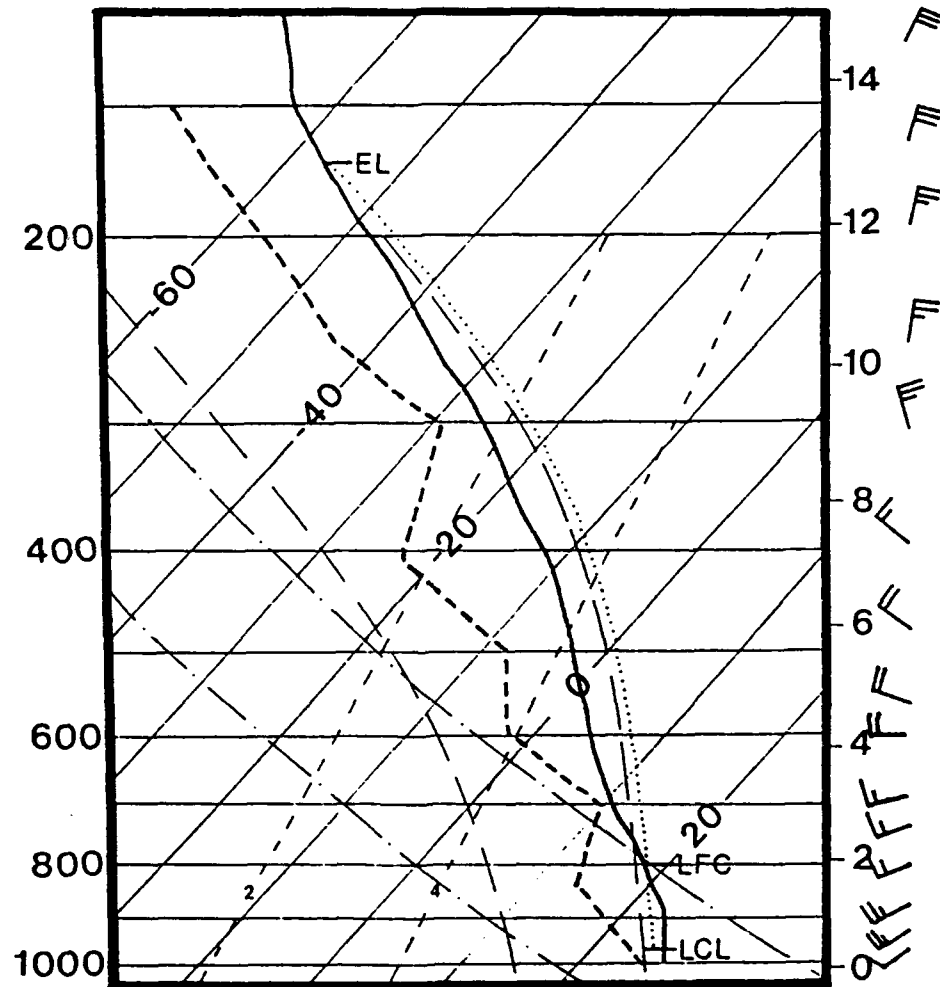


Fig. 3.5 The environmental sounding at 02 LST 25 June 1987 for the pre-frontal atmosphere at Makung in the Taiwan Strait. The lifting condensation level (LCL), the level of free convection (LFC) and the equilibrium level (EL) are indicated.

for IOP-13 was $1045 \text{ m}^2 \text{ s}^{-2}$ suggesting only weak and moderate updrafts within this rainband (Lin *et al.*, 1992). Like all stability parameters, essentially what CAPE is, proper use should only be in conjunction with all other available tools.

The postfrontal sounding (see Fig. 3.6) displays that a significant change took place in the environment. This sounding indicates that the environment became conditionally stable. Even though there is a deep layer of moisture, convection was capped by the higher LFC (now at 650 mb) and the lower EL (now at 510 mb) and also inhibited due to the lack of a forcing mechanism. Low-level winds were from the northwest indicating the arrival of much cooler air from northern China.

How equivalent potential temperature (θ_e) varies with height is a good indicator of the stability of the environment. Figure 3.7 pictures the vertical profile of θ_e during both the prefrontal and postfrontal environments at Pan-Chiao. In the prefrontal environment, θ_e decreased with height to about 800 mb indicating a convectively unstable atmosphere. After the front passed, θ_e at the lower levels dramatically changed from the prefrontal conditions decreasing by 10-15 ° K. This indicates the air after frontal passage was much cooler and drier. The profile shows that θ_e increased with height up to about 800 mb, thus the postfrontal atmosphere was convectively stable.

Figures 3.8 and 3.9 display time-height variations of the environmental

Pan-Chiao 0200 LST 25 June 1987

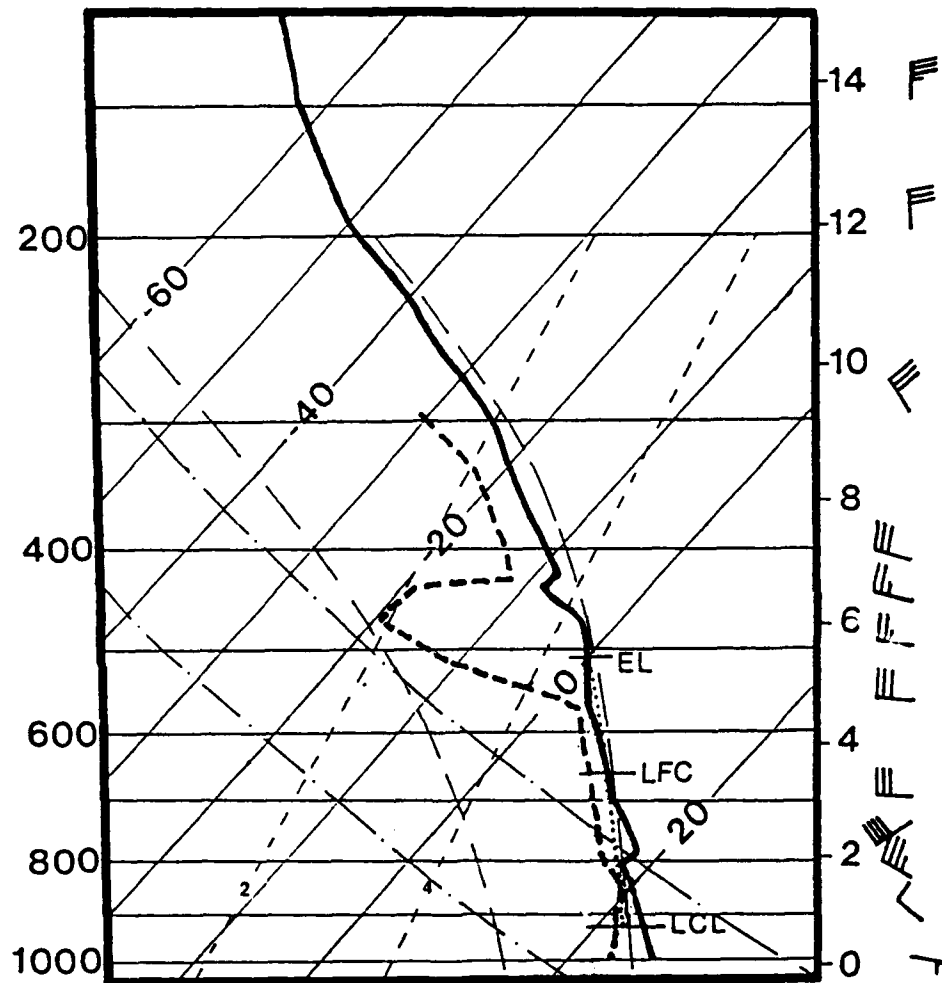


Fig. 3.6 Same as in Fig. 3.5 except for the postfrontal atmosphere at Pan-Chiao in northern Taiwan.

TAMEX IOP-13 Pan-Chiao Station

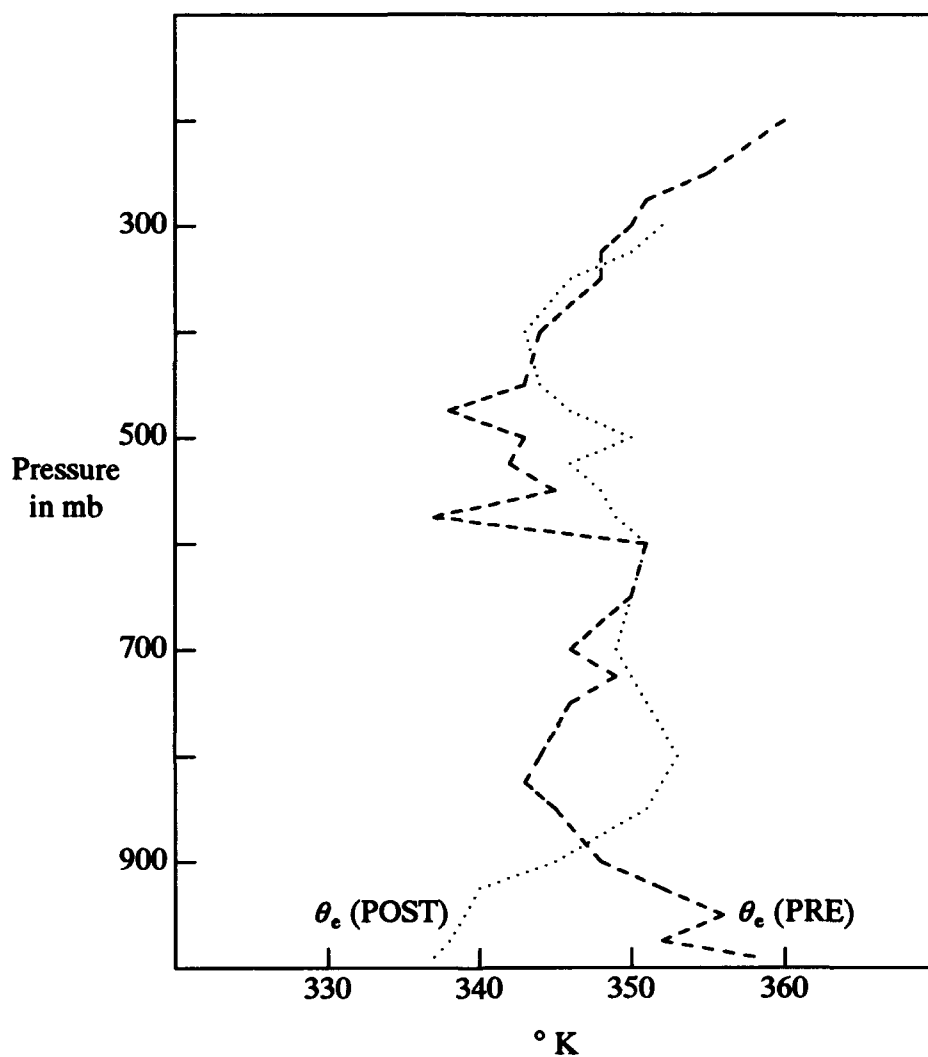


Fig. 3.7 Vertical profile of equivalent potential temperature (θ_e) for the pre-frontal environment (θ_e (PRE)) for Pan-Chiao at 20 LST on 24 June 1987 and for the postfrontal environment (θ_e (POST)) for Pan-Chiao at 08 LST on 25 June 1987.

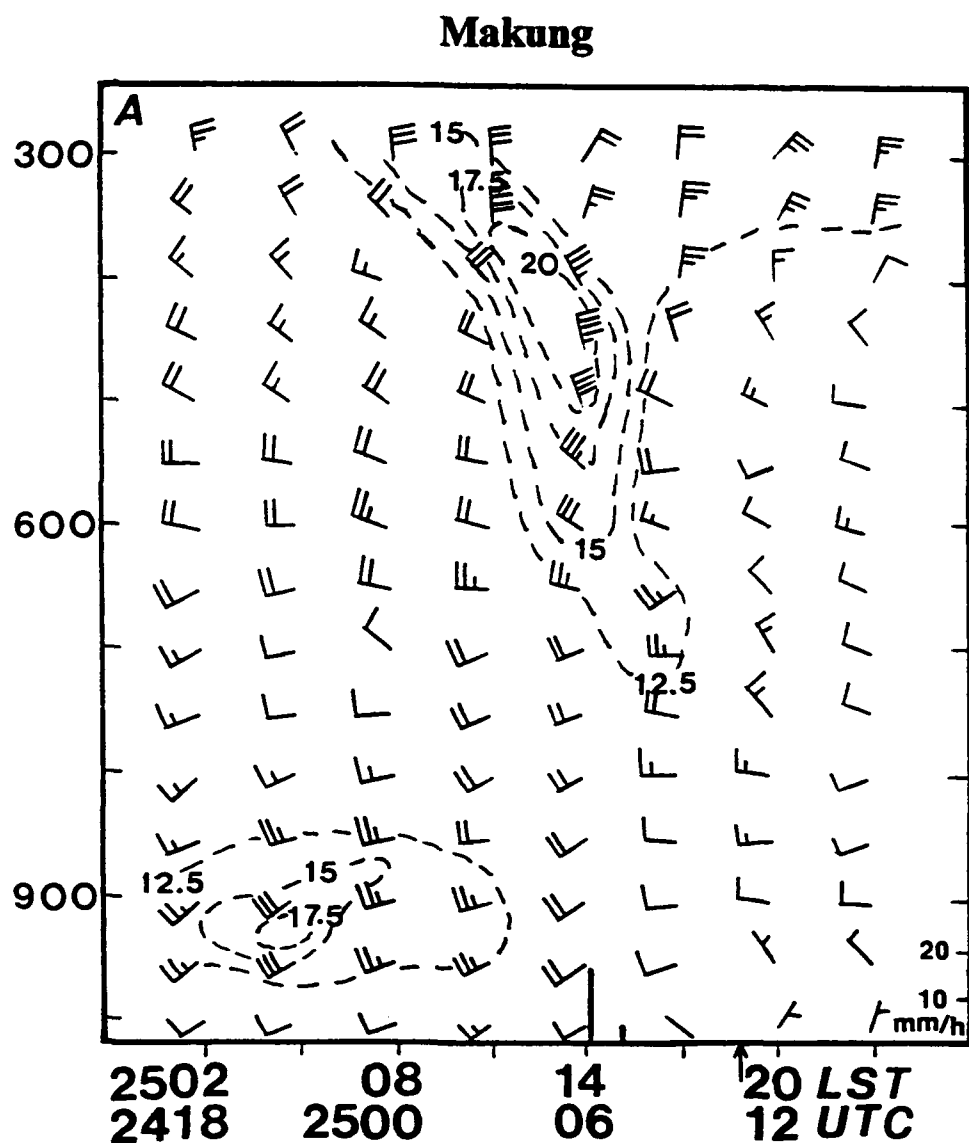


Fig. 3.8 Time-height variations of rawinsonde winds at Makung on 25 June 1987. Times are in both LST and UTC. Isotachs (in $m s^{-1}$) are contoured by the dashed lines. The arrow denotes the time of Mei-Yu frontal passage. The vertical solid bar along the time axis shows the precipitation rate (in $mm h^{-1}$) (after Lin *et al.*, 1992).

winds at Makung and Pan-Chiao. At Makung (Fig. 3.8), rawinsonde winds are plotted in intervals of every 3 h starting from 0200 LST and ending at 2300 LST 25 June. Recall that the cold front passed through the station by 1900 LST (see the arrow in Fig. 3.8). During the prefrontal period, the southwest monsoon flow prevailed in the lower troposphere. By 0500 LST, the LLJ with a maximum speed of 18 m s^{-1} (36 knots) was evident at the 930 mb level. The orientation of this jet was nearly parallel to the Mei-Yu front described earlier. Strong vertical wind shear occurred at levels above and below the LLJ. However, in the middle and upper troposphere, however, no apparent middle and upper level jets were visibly present. As the convective rainband approached the station, a significant variation in wind speed occurred at heights above 600 mb. By 1400 LST, the LLJ was no longer evident in the lower layer. Instead, a middle level jet (MLJ) with maximum speeds in excess of 20 m s^{-1} (40 knots) developed in the layer between 350 and 500 mb. This time coincided with the convective activity at Makung.

Figure 3.9 depicts time-height variations of the environmental winds at Pan-Chiao from 0800 LST 24 June to 1700 LST 25 June. Prior to frontal passage, the LLJ with a maximum speed up to 25 m s^{-1} (50 knots) prevailed at the 900 mb level. This speed was stronger than that observed at Makung (Fig. 3.8). Notice that the observational times of the LLJ at two stations were different. Examination of Fig. 3.9 further reveals that no middle and upper level jets were visible before the convection. After the convective rainbands reached the

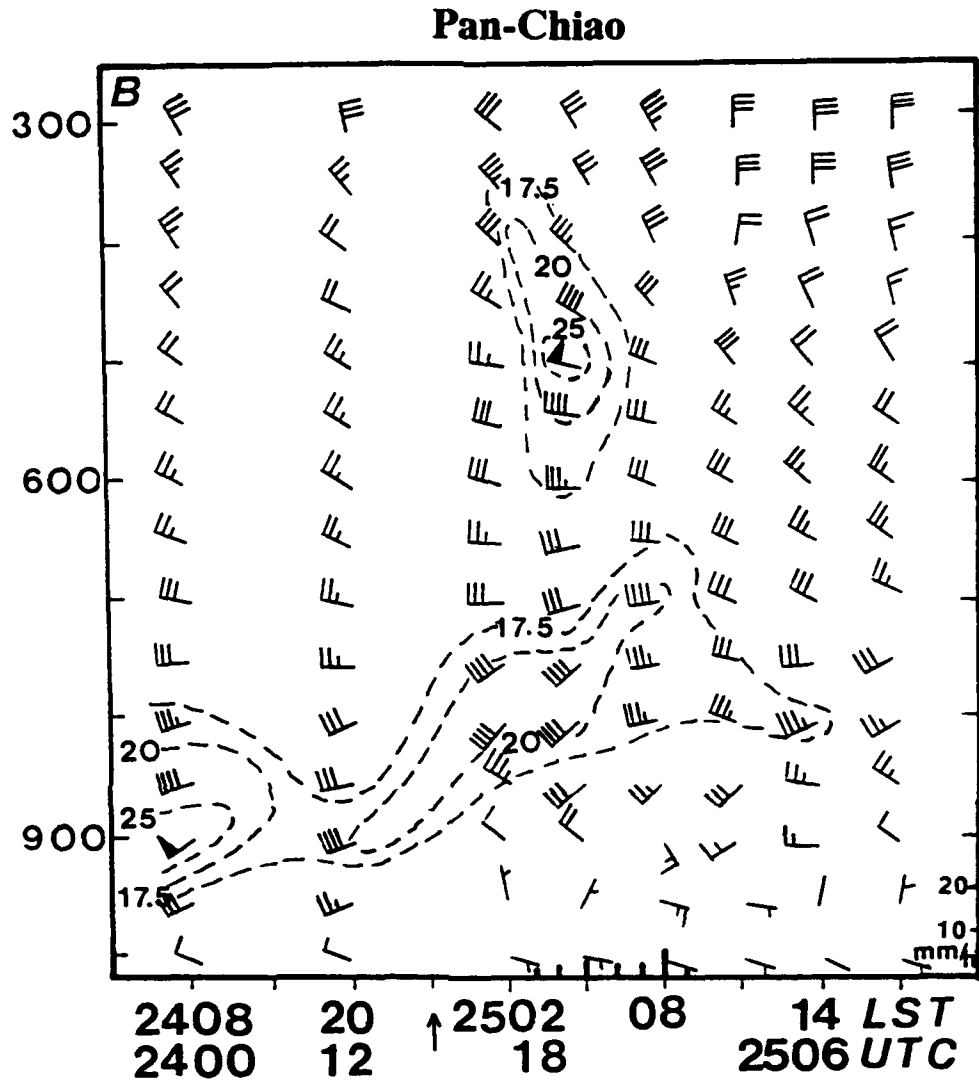


Fig. 3.9 Same as in Fig. 3.8 except for Pan-Chiao on 24-25 June 1987 (after Lin *et al.*, 1992).

station, the LLJ was lifted to the 700-800 mb layer. Additionally, the MLJ formed at 500 mb with a maximum speed of 25 m s^{-1} by 0500 LST 25 June, a feature similar to that observed at Makung (Fig. 3.8). Both the MLJ and LLJ then weakened substantially after convection ceased.

3.5 Radar Summary

Figure 3.10 illustrates the radar reflectivity distribution in relation to the gust front (indicated by the heavy dashed line) and the Mei-Yu front (denoted by the heavy solid line) on an hourly basis beginning at 0300 LST 25 June. The hourly plan-position indicator (PPI) scans were recorded by the 10-cm Koahsiung (744) conventional radar located over southern Taiwan (see Fig. 1.1). The gust front and Mei-Yu front locations were based on synoptic observations (some of those discussed in section 3.2). The circle represents the dual-Doppler coverage area of the CP-4 and TOGA radars. Reflectivity contours are every 10 dBZ beginning with 15 dBZ. The lined areas within the contours represent 25 dBZ or greater, while the hatched areas are 35 dBZ or higher. The completely darkened areas are 45 dBZ or greater. Notice how the spatial difference between the location of the gust front and the Mei-Yu front slowly increases as time progresses and how the northern portion of the Mei-Yu front remains quasi-stationary.

At 0300 LST, the precipitation signatures are located along and behind both the gust front and Mei-Yu front. By 0400 LST, the signatures start to

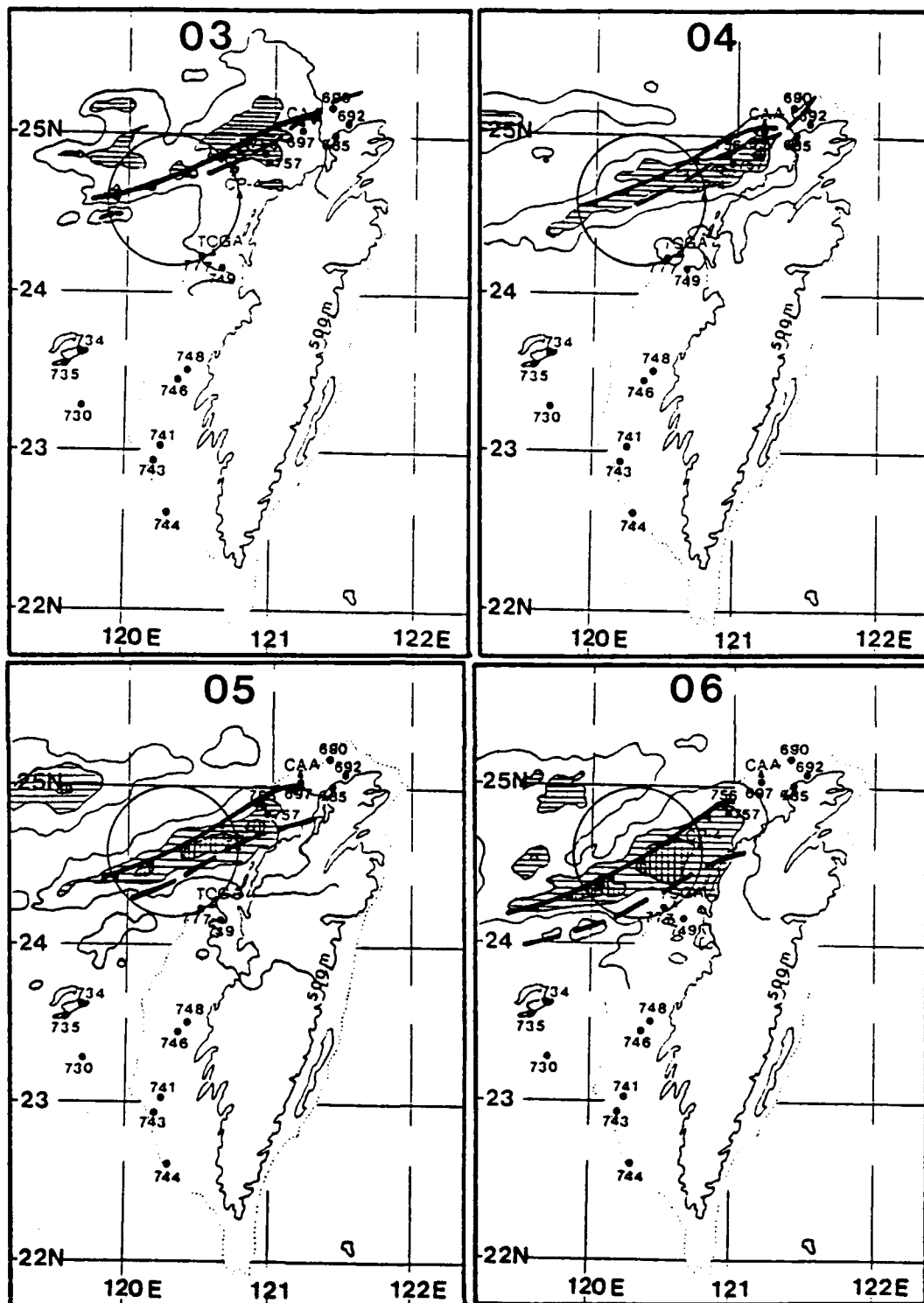


Fig. 3.10 Hourly PPI radar reflectivity distribution (in dBZ) in relation to the gust front (heavy dashed lines) and the Mei-Yu front (heavy solid lines) from 0300 LST until 1800 LST 25 June 1987. Lined areas of reflectivity denote 25-34 dBZ, hatched areas 35-44 dBZ and solid dark areas represent 45 dBZ or higher.

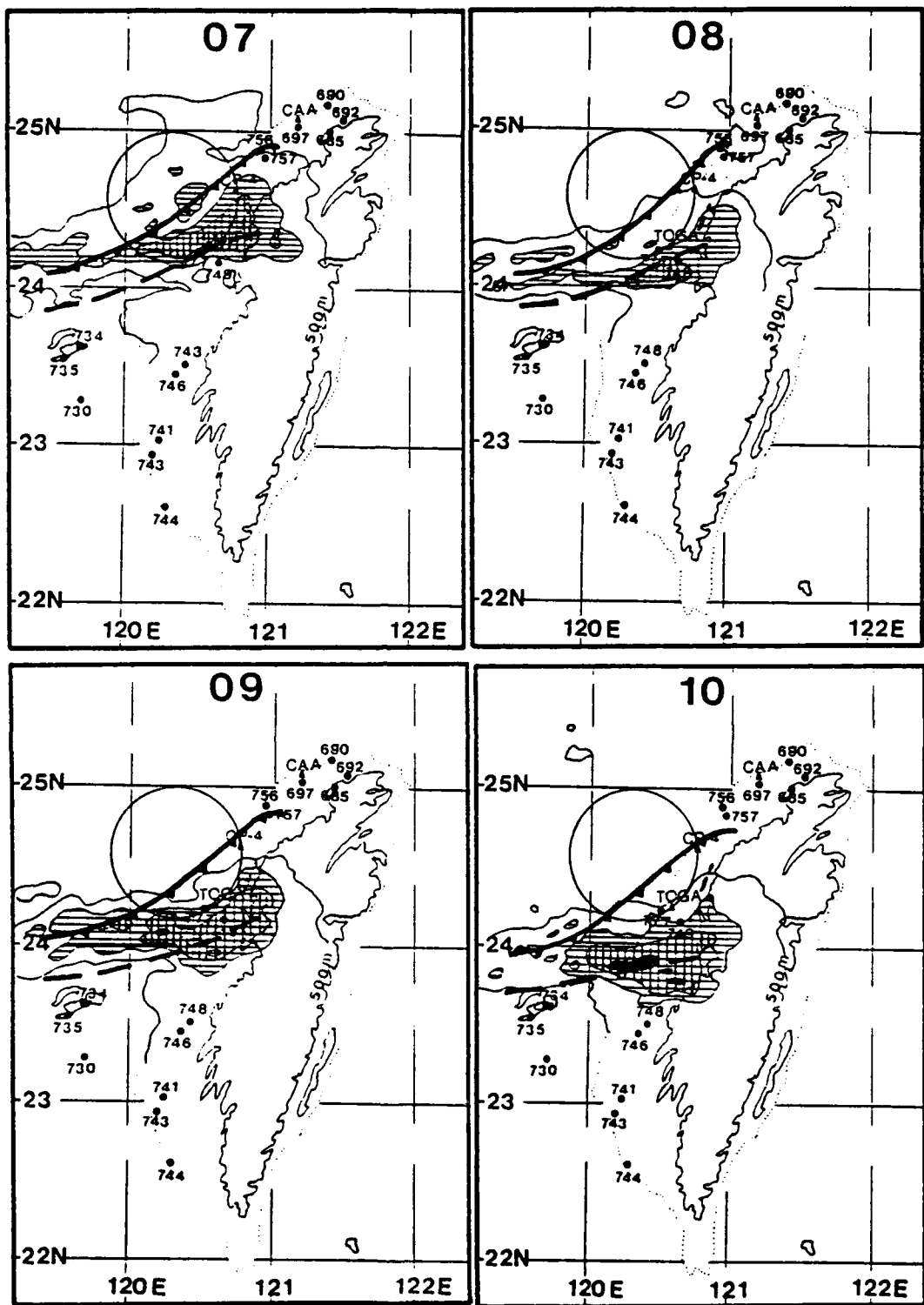


Fig. 3.10 Continued.

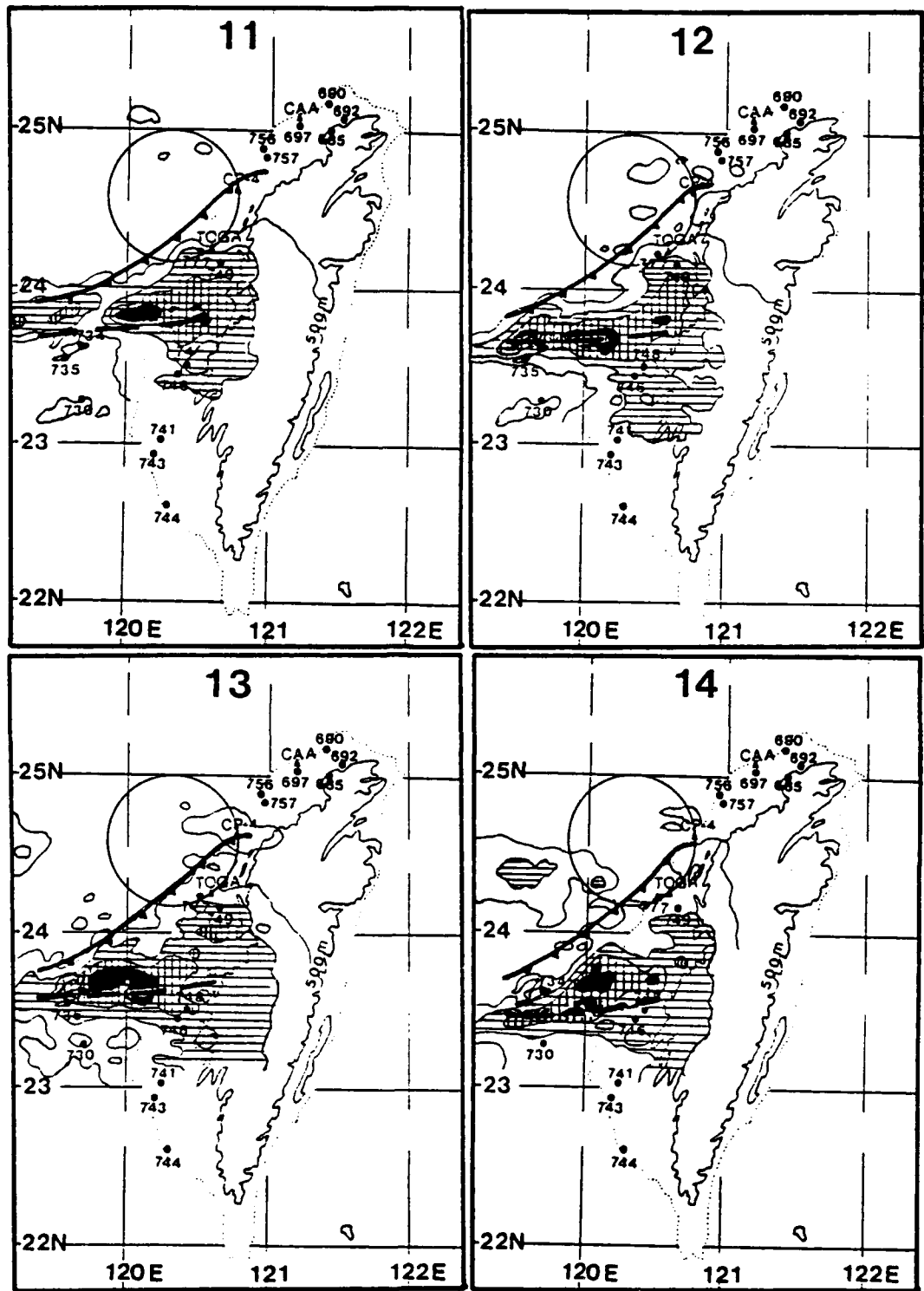


Fig. 3.10 Continued.

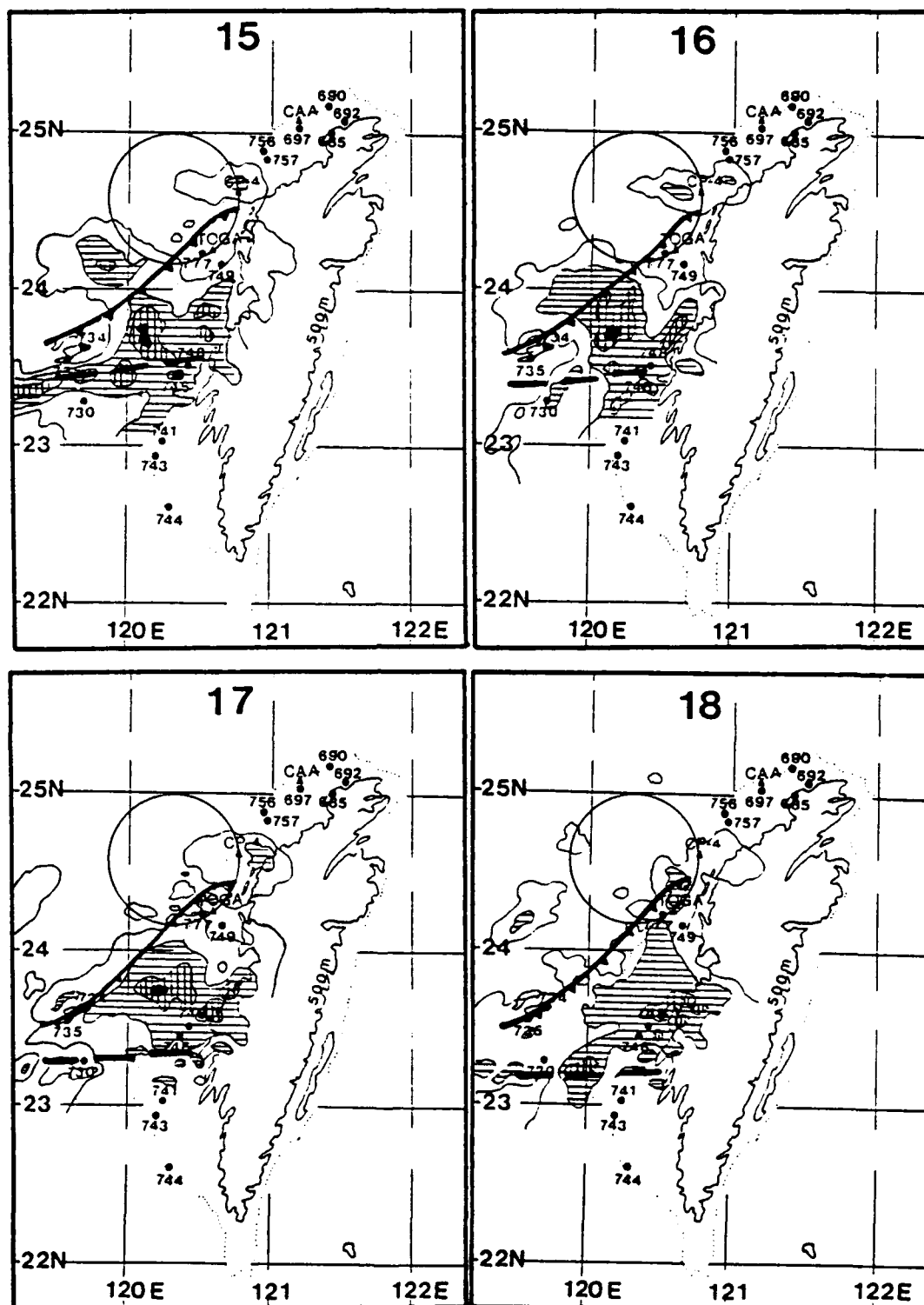


Fig. 3.10 Continued.

elongate in an eastnortheast-west southwest (ENE-WSW) orientation ahead of the front with a cell located near the CAA radar. By 0500 LST, a line of cells (constituting the first semblance of a prefrontal rainband) developed in the area between the gust front and Mei-Yu front. At 0600 LST, the gust front moved to along the coast of west central Taiwan. Several stronger cells developed within the dual-Doppler coverage area and were again, located ahead of the Mei-Yu front. By 0700 LST, a distinctive prefrontal rainband has developed along this coast. At this time, the rainband was located in the southeast corner of the dual-Doppler coverage area. By 0800 LST, we see the convective cells begin to dissipate, however, a new line of cells appear to be developing along the gust front from 0900 to 1000 LST. These new cells continued to grow over the next several hours and perhaps a new gust front formed to the south of these cells due to their outflow. Unfortunately, these cells were outside the dual-Doppler coverage area. By 1800 LST, almost all convective activity had dissipated as the front pushed onto land thus cutting off its moisture source.

3.6 Rainfall Distribution

As noted earlier, extensive precipitation fell on the west coast of Taiwan. The rainfall amount was recorded at 30-min intervals over most of the TAMEX mesonet network. Figure 3.11 displays rainfall rate (in *mm* per 30 minutes) for several stations discussed in section 3.2. CAA (686) and Tao-Yuan (697) received their heaviest amount of rainfall (30-50 *mm*) within one and a half

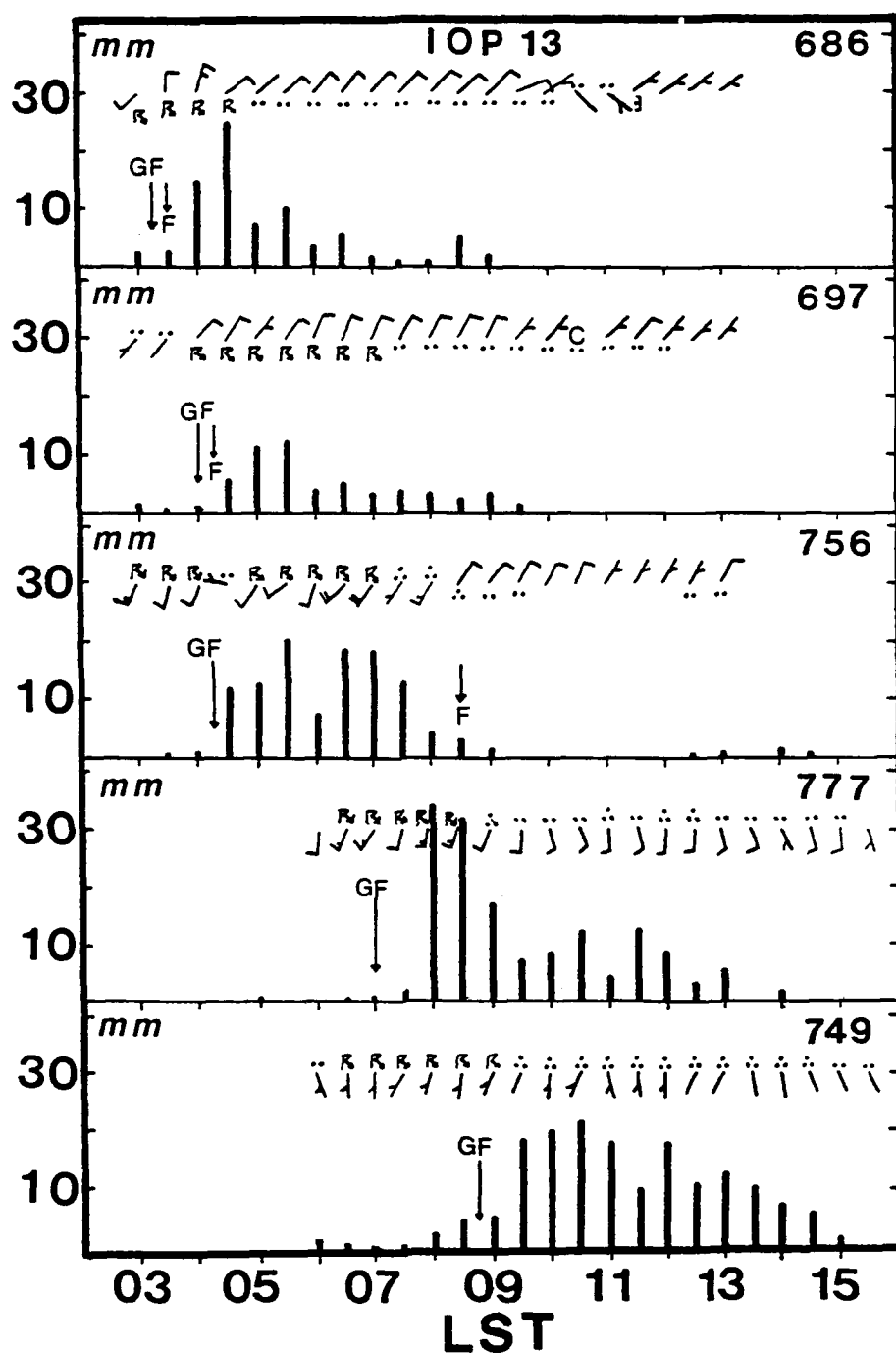


Fig. 3.11 Rainfall rate in *mm* per 30 minutes for several surface observation stations within the TAMEX mesonet. Also displayed are wind direction, wind speed in knots, and significant weather. GF and F (and corresponding arrows) represent passage of the gust front and Mei-Yu front, respectively.

hours after the Mei-Yu front passed. However, these totals were small compared to some of the other stations.

Hsin-Chu (756) received 10-20 *mm* of rain every half hour from the time the gust front passed until one hour prior to frontal passage. This totalled nearly 100 *mm* of rainfall within three and a half hours. Wu-Chi (777) reported approximately 80 *mm* of rainfall between the period of 0730-0900 LST. Moderate to heavy rain continued for several hours adding nearly 65 *mm* more to their total. The most amount of rainfall was received by Tai-Chung (749) where convection followed by five hours of heavy rain dumped about 170 *mm* of rain. Between 0900 and 1100 LST alone, 80 *mm* (about 3.1 inches) was reported. Coupled with the drainage from the mountainous regions nearby, it is easy to see why extensive flash flooding occurred in the central west coast region of Taiwan.

It is also beneficial to look at the entire area of the 30 minute rainfall rate as depicted by Fig. 3.12. Note that the display are at hourly segments even though the rates are based upon 30 minute intervals. The dashed rainfall distribution are displayed with relation to the gust front and the Mei-Yu front in a similar manner to reflectivities in Fig 3.10. Dashed contours are every 5 *mm* and represent rainfall rates beginning with 5 *mm* per 30 minutes. In the higher concentrated precipitation areas, contours are every 10 *mm*. Hatched areas represent 20 *mm* or greater rainfall rates. Note how the precipitation rates in the northern region are at most 15 *mm* per 30 minutes for the time periods

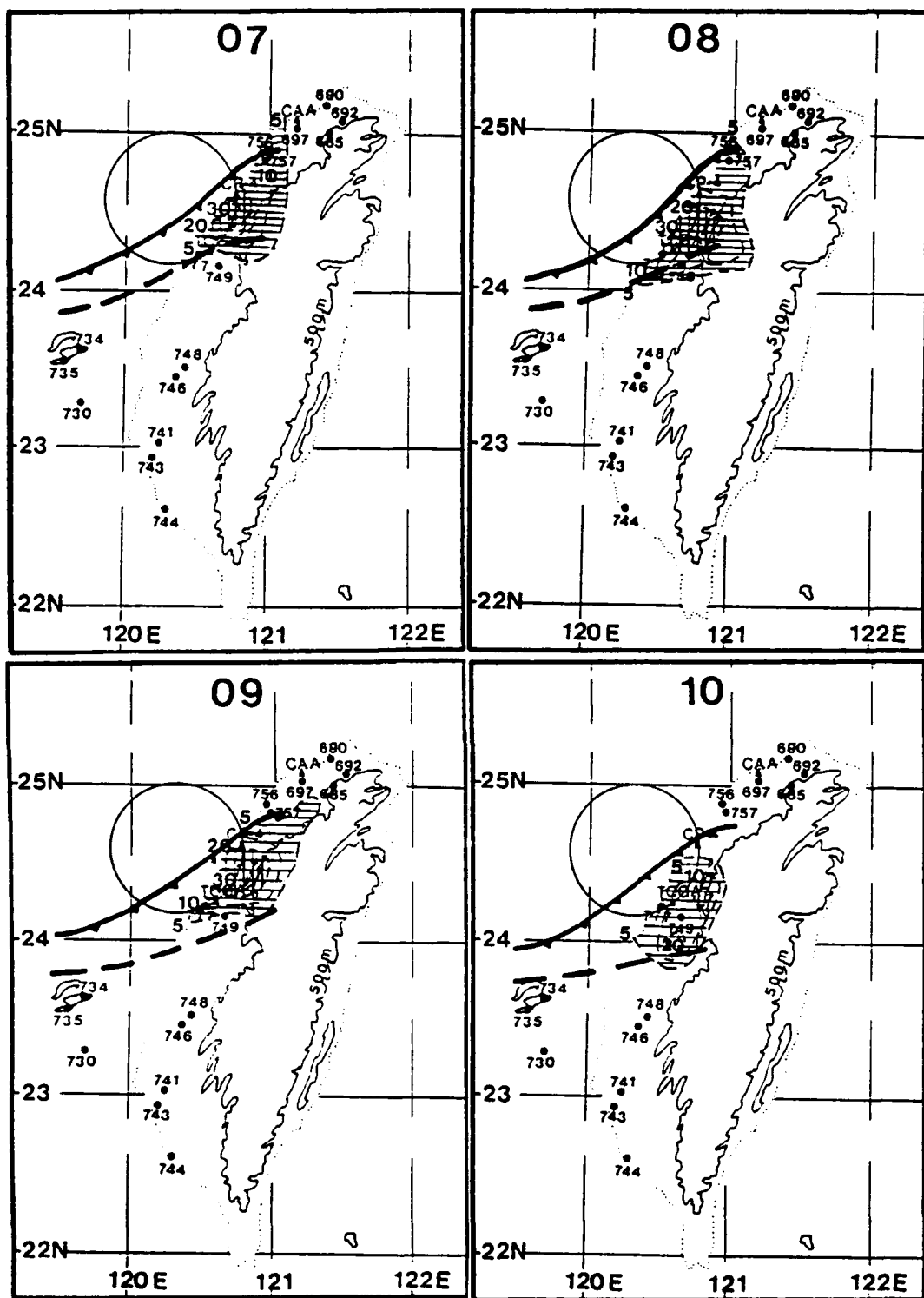


Fig. 3.12 Continued.

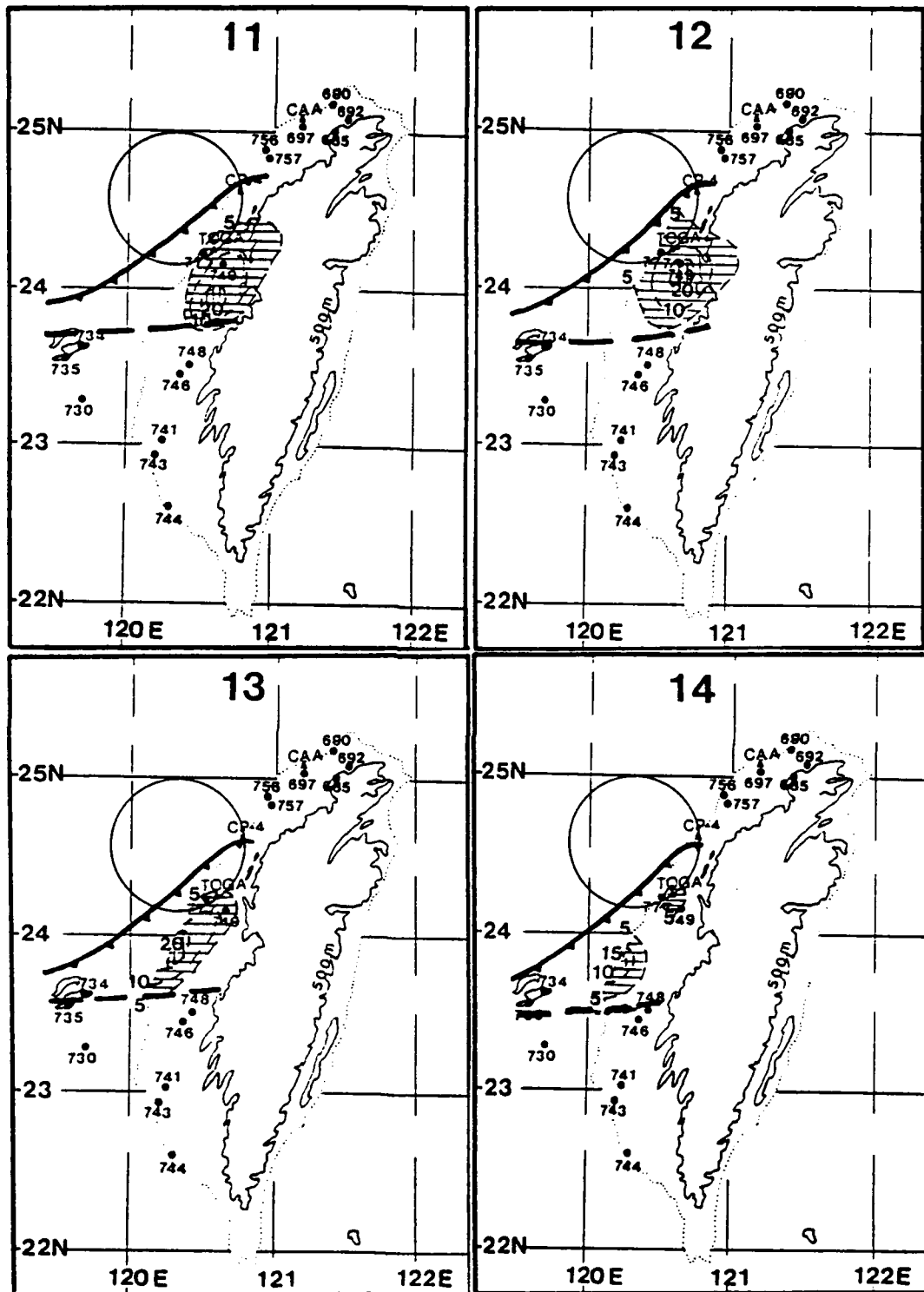


Fig. 3.12 Continued.

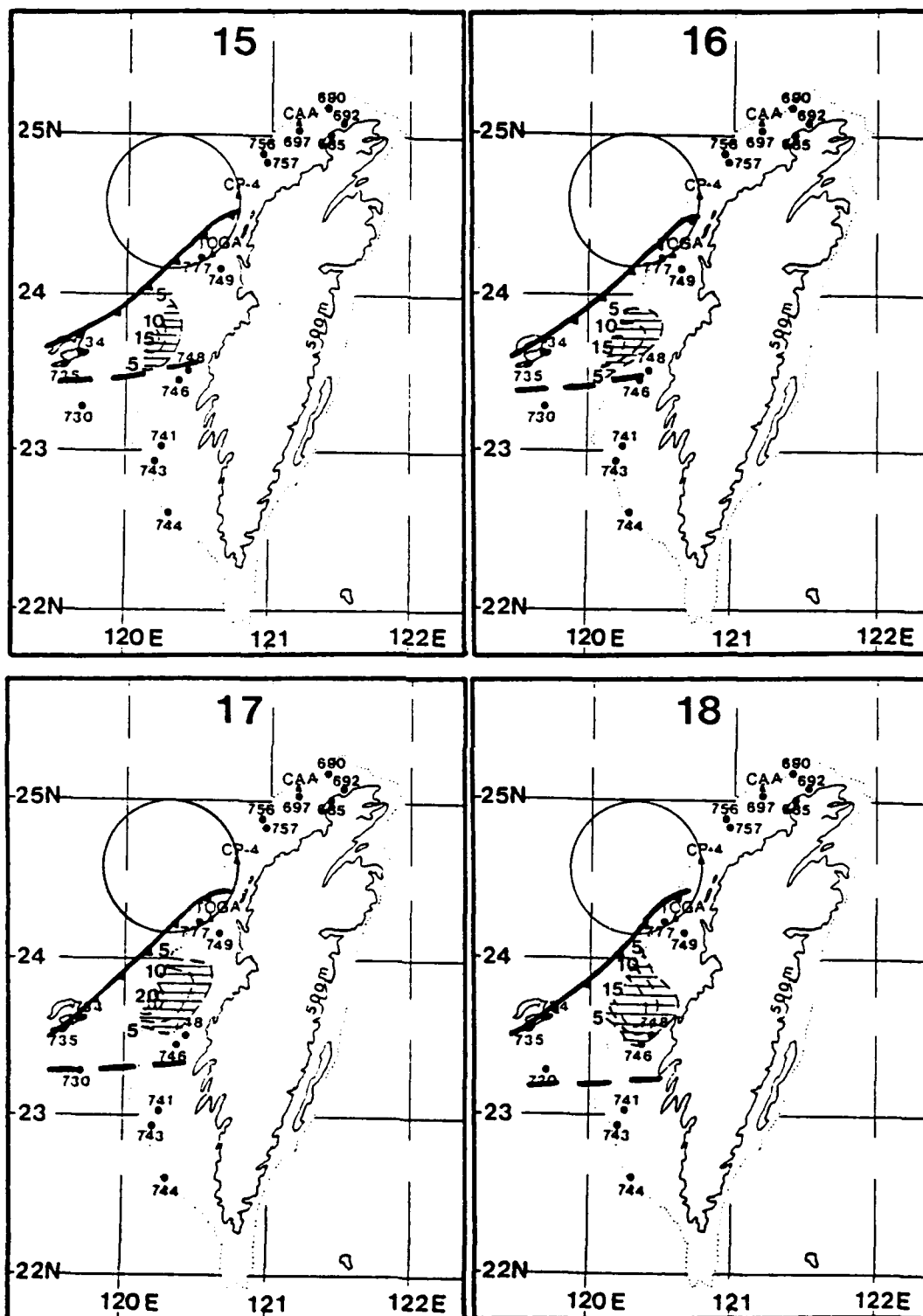


Fig. 3.12 Continued.

between 0300 and 0500 LST. By 0700 LST, rates between the CP-4 and TOGA exceeded 30 *mm* per 30 minutes. The 30 *mm* rate bullseye remained in an area along the west coast of central Taiwan for several hours with the center near the TOGA radar. Between 1000 and 1200 LST, the largest precipitation rates were being recorded south of the TOGA radar and more inland. Then as new cells developed, rates between 15 and 20 *mm* were recorded along the coast and near the stations of Chia-Yi (746) and the Air Force station at Chia-Yi (748). In almost all the hourly segments, largest recorded rainfall rates were located between the gust front and the Mei-Yu front. This also gives credence to the statement that the rainband was prefrontal. Figure 3.13 shows the 24 hour accumulated rainfall distribution for 25 June over all Taiwan. Contour interval is 40 *mm* per 24 hours. Two areas of up to 200 *mm* occurred near the TOGA radar. The northern and central west coasts of Taiwan received the most rain.

TAMEX IOP-13

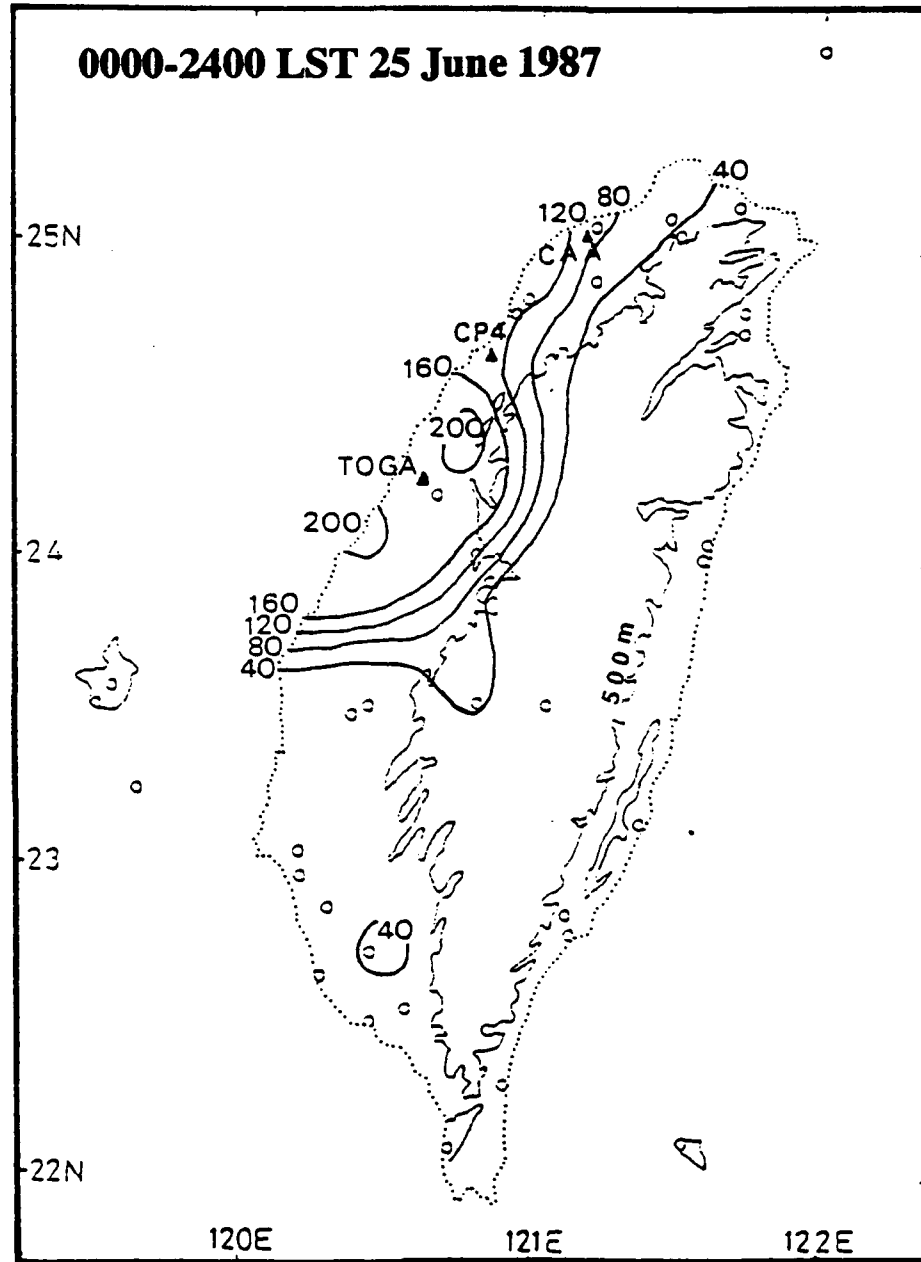


Fig. 3.13 The accumulated 24 hour rainfall amounts on 25 June 1987 over Taiwan. Contour interval is 40 mm per 24 hours (after Chang, 1992).

Chapter 4

Methodology

The methodology of this thesis research consisted of several steps. The initial steps were to collect rawinsonde, satellite, mesonet, conventional radar, Doppler radar and synoptic data applicable to this case. Then study published papers which pertain to this thesis. Carefully analyze the environmental conditions of this case. This provided sound background information in order to start the data research portion. In the data research portion, I used and modified the Saint Louis University Doppler Radar Analysis System (SLU DRAS) which was developed by Lin *et al.* (1982, 1986, 1987, 1988, 1990, 1992) to process the dual-Doppler data of IOP-13, check the results of computation, then interpret and compare these results with other related studies.

4.1 Data Reduction

As described in Chapter 1, three 5-cm Doppler radars were positioned along the northwest coast of Taiwan (Fig. 1.1) with the baseline between CP-4 and TOGA at 45 km. Dual-Doppler data collected from these two radars are the main data source considered in this study. Table 2 shows some basic characteristics of CP-4 and TOGA for comparison purposes. Both radars used 64 pulses to estimate the measure quantities and both had a maximum range of 120 km. However, the most significant difference between these two radars is the half-power beamwidth which is 1.02° for CP-4 and is 1.60° for TOGA.

Table 2

Characteristics of the TOGA and CP-4 radars (after Wang *et al.*, 1990).

Characteristics	CP-4	TOGA
Wavelength (cm)	5.49	5.38
Frequency (GHz)	5.46	5.57
Peak Power (Kw)	400	250
Pulse Duration (microsec)	1.0	2.0
Pulse Repetition Frequency (Hz)	1,250	1,250
Antenna Diameter (m)	3.70	2.44
Antenna Gain (dB)	41	38
Beamwidth (Deg)	1.02	1.60
Noise Power (dBm)	-114	-111
No. of Samples (Pulses)	64	64
Pulse Length (m)	150	300
Maximum Velocity ($m s^{-1}$)	17.16	16.81
Maximum Range (Km)	120	120
Min. Detectable Reflectivity (dBZ)	-16	-12

Thus, the radar beam resolution at 57.3 km away from each radar is 1.02 km for CP-4 and 1.60 km for TOGA which shows that CP-4 has a better resolution than that of TOGA at the same distance. This must be taken into account when domain of interest and grid spacing are selected.

Raw TAMEX Doppler data were archived for researchers at the National Center for Atmospheric Research (NCAR). The data must be properly processed to minimize the errors and extract the physical information. With the aid of NCAR's Research Data Support System (RDSS), an interactive computing system, we can edit Doppler data. Enhanced color graphics allows the user to be interactive with the editing software and with color display of radar data. In the editing process, only those data which satisfy certain objective criteria, derived from the radar theory and physical limitation, were accepted. Range and velocity foldings were properly corrected and ground clutter was removed using RDSS.

After the Doppler data for each radar were properly edited, the data analysis and reduction procedures developed at Saint Louis University were used to process dual-Doppler data. The procedures of SLU DRAS include: 1) data converting; 2) data editing; 3) objective analysis; 4) synthesis of Doppler data; 5) three-dimensional wind field calculation; 6) perturbation pressure and virtual temperature derivation retrievals; and 7) computations of the total kinetic energy budget, momentum-flux budget and vorticity budget.

Two volume scans at 0653 and 0700 LST 25 June were obtained from the CP-4 and TOGA radars. These data were collected into 10 slabs of varying vertical depth whose mean altitudes range from 0.35 to 8.75 km. All variables within a slab were objectively interpolated onto horizontal Cartesian grids using the Barnes (1973) objective analysis scheme with a 2.5 km scan radius. Filtering is inherent in this objective analysis scheme, especially for mesoscale perturbations with wavelength < 3 km. Grid spacing was 1 km in both the horizontal and vertical directions except at the lowest two levels where the vertical grid spacing was chosen to be 0.5 km. The data reduction procedures provide a regular three-dimensional field of three variables, i. e., two radial velocity components (V_{r1} , V_{r2}) and the radar reflectivity (Z). There are four unknown variables including three Cartesian wind components (u , v , w) and the terminal fall speed of precipitation particles in the distributed target (V_T). The V_T value is empirically related to reflectivity via a V_T - Z relationship. Two horizontal wind components (u , v) are related to the two radial velocity equations from two radars. The fourth equation is the anelastic continuity equation for calculation of the vertical wind component (w).

4.2 Three-dimensional Winds

The scheme in computing the horizontal velocity components was proposed by Armijo (1969), and used by Brandes (1977, 1978), and Lin *et al.* (1986). Following these studies, the u - and v -components can be expressed as

$$u = \frac{R_1 V_{r1}(y - y_2) - R_2 V_{r2}(y - y_1) - [(y_1 - y_2)(w + V_T)z]}{(x - x_1)(y - y_2) - (x - x_2)(y - y_1)} \quad (4.1)$$

$$v = \frac{R_1 V_{r1}(x - x_2) - R_2 V_{r2}(x - x_1) - [(x_1 - x_2)(w + V_T)z]}{(y - y_1)(x - x_2) - (y - y_2)(x - x_1)} \quad (4.2)$$

where R_i is the radial distance from radar i to the target measured by radar i , $(x_i, y_i, 0)$ is the i th radar location, $i = 1$ or 2 , and (u, v, w) are the true winds in Cartesian coordinates.

The terminal fall speed is estimated from the formula proposed by Sekhon and Srivastava (1971). A simple density-height correction suggested by Foote and du Toit (1969) is added, i.e.,

$$V_T = -4.32 Z^{0.052} \left(\frac{\rho_{\infty}}{\rho_o} \right)^{0.4} \quad (4.3)$$

where $\rho_o(z)$ is the environmental air density, ρ_{∞} is the standard surface air density, and V_T is the mean terminal fall speed of hydrometeors within the target.

Finally, the anelastic continuity equation can be written as:

$$\frac{\partial[\rho_{oa}(z)w]}{\partial z} = -\rho_{oa}(z) \nabla_h \cdot \mathbf{V} \quad (4.4)$$

where ρ_{oa} is the density in an adiabatic-hydrostatic atmosphere. It is approximately equal to the environmental density ρ_o (Brandes, 1984; Lin *et al.*, 1986;

etc).

The aforementioned four equations form a complete set of equations to solve three Cartesian wind components within a convective system as long as the boundary value of w is known. Vertical velocities were computed from the anelastic continuity equation by integrating downward from the storm top, assuming $w = 0$ at the top. Ray *et al.* (1980) showed that a downward integration from storm top accumulates less error in w calculation than an upward integration from the surface. Other Doppler studies, e.g., Chong and Testud (1983), Lin *et al.* (1986), etc, also showed the same result.

A variational method for computing vertical velocities was detailed in Ray *et al.* (1980), Ziegler *et al.* (1983), Roux *et al.* (1984), Lin *et al.* (1986), etc. The method used in this study is similar to that of Ziegler *et al.* (1983) and Lin *et al.*, (1986). The governing analysis equations are:

$$u - u^o = \frac{\rho_o}{2\alpha^2} \frac{\partial \lambda}{\partial x} \quad (4.5)$$

$$v - v^o = \frac{\rho_o}{2\beta^2} \frac{\partial \lambda}{\partial y} \quad (4.6)$$

$$\int_{z_i}^0 \nabla_3 \cdot \rho_o \mathbf{V} \, dz = 0 \quad (4.7)$$

where λ is the Lagrange multiplier, α and β are weighting factors to be

determined from the natural distribution of errors in the observed wind fields. Equations (4.5) and (4.6) are Euler-Lagrange equations of the variational form, (4.7) is the constraint equation, where z_t is the storm top.

Differentiating (4.5) with respect to x and (4.6) with respect to y and adding, we arrived at the following elliptic equation:

$$\int_{z_t}^0 \rho_o \left\{ \frac{\partial}{\partial x} (\rho_o \sigma_u^2 \frac{\partial \lambda}{\partial x}) + \frac{\partial}{\partial y} (\rho_o \sigma_v^2 \frac{\partial \lambda}{\partial y}) \right\} dz = (\rho_o w^o)_{sfc} \quad (4.8)$$

where $\sigma_u^2 = (2\alpha^2)^{-1}$ and $\sigma_v^2 = (2\beta^2)^{-1}$. The field of λ can be solved from (4.8) by successive overrelaxation (SOR) with the natural boundary condition (i.e., λ is zero along the lateral boundary). Subsequently, the horizontal components of true winds (u, v) are obtained from the observed wind (u^o, v^o) using (4.5) and (4.6). The vertical velocity (w) at a given height, z_l , is calculated from the following formula:

$$w_l = w_l^o - \frac{(\rho_o w^o)_{sfc}}{\rho_{ol}} \frac{\int_{z_t}^{z_l} \rho_o dz}{\int_{z_t}^0 \rho_o dz} \quad (4.9)$$

4.3 Error Analysis

All meteorological measurements are subject to some uncertainties. Error analysis is necessary to determine the level of confidence of the data measured.

In this study, the derived wind field is subject to both random and non-random errors. Error sources in the horizontal and vertical wind components were discussed in studies by Bohne and Srivastava (1976), Doviak *et al.* (1976), Ray *et al.* (1978, 1980), Parsons *et al.* (1983), Roux *et al.* (1984), Lin *et al.* (1986), Nelson and Brown (1987), etc. For random errors which are independent of height, Bohne and Srivastava (1976) showed theoretically that the horizontal wind components are reasonably accurate to about 1 m s^{-1} . Other sources of non-random errors in the derived wind field are due to: 1) the advection/ evolution problem; 2) the ground clutter; 3) the side lobes; 4) inaccurate boundary conditions; etc.

Many researchers investigated error analyses of horizontal winds for Doppler radar observations. Wilson *et al.* (1984) conducted error estimates for the statistical uncertainty of the dual-Doppler derived winds obtained from the JAWS (Joint Airport Weather Studies) project. They determined that the combined errors due to statistical uncertainty in the radial velocity estimates and geometrical considerations are approximately $1\text{-}2 \text{ m s}^{-1}$ in the horizontal winds. Lin *et al.* (1990) and Wang *et al.* (1990) conducted an error analysis following the same procedures using the TAMEX dual-Doppler data in IOP-2. They found that the upper limits for random errors in the derived horizontal winds are about $1.5\text{-}2.0 \text{ m s}^{-1}$.

Regarding vertical velocity calculations, Bohne and Srivastava (1976) and Ray *et al.* (1980) found theoretically that an error variance in w can be

significantly reduced by integrating the mass continuity equation downward from the storm's top. In addition, the Doppler studies by Ray *et al.* (1980), Ziegler *et al.* (1983), Roux *et al.* (1984), Hane and Ray (1985) and Lin *et al.* (1986) have demonstrated that errors in w due to random and non-random errors can be greatly minimized by using a variational approach. Therefore, both downward integration and variational techniques are employed in this study. Another source of error which could contribute to the uncertainty of w is a result of the advection problem (Gal-Chen, 1982; Chong and Testud, 1983). Parsons *et al.* (1983) employed an advection correction scheme suggested by Gal-Chen (1982) to account for the temporal differences in scanning the storm volume. They found that velocity errors were reduced by an order of magnitude as a result of the correction. However, when a moving coordinate system is considered, the advection error can be substantially reduced.

The local steady state assumption in the momentum equations will contribute errors to the retrieval of thermodynamic variables (Hane *et al.*, 1981). This assumption is commonly made in Doppler studies. It implies that there is no evolution within the convective system during the entire volume scan, typically 6-7 min. Simulation studies by Gal-Chen (1978) and Hane *et al.* (1981) showed that the only way to reduce the evolution error is to scan the storm more rapidly. Additional sources of error which could contribute to thermodynamic retrieval include methods used for estimating precipitation loading and friction. A sensitivity study is conducted to determine the impact of these

errors on the retrieved fields of pressure and buoyancy perturbations.

4.4 Thermodynamic Retrieval

Following the studies by Gal-Chen (1978) and Parsons *et al.* (1987), the momentum equations can be written as

$$\frac{\partial \pi}{\partial x} = - \frac{1}{c_p \theta_{vo}} \left(\frac{Du}{Dt} + f_1 \right) = F \quad (4.10)$$

$$\frac{\partial \pi}{\partial y} = - \frac{1}{c_p \theta_{vo}} \left(\frac{Dv}{Dt} + f_2 \right) = G \quad (4.11)$$

$$\frac{\partial \pi}{\partial z} = - \frac{1}{c_p \theta_{vo}} \left(\frac{Dw}{Dt} - g\beta' + f_3 \right) = H \quad (4.12)$$

where $\frac{Du}{Dt}$, $\frac{Dv}{Dt}$ and $\frac{Dw}{Dt}$ are accelerations along the x-, y- and z-axes, respectively; f_1 , f_2 and f_3 are the forces other than pressure gradients; $\pi = (P'/P_{\infty})^{R/C_p}$ is a perturbation Exner function; θ_{vo} is the mean virtual potential temperature, R is the specific gas constant and C_p is the specific heat at constant pressure. The buoyancy parameter, β' , is approximated as

$$\beta' \approx \frac{\theta'}{\theta_o} + 0.61q'_v - q_l \quad (4.13)$$

where θ_o denotes the mean potential temperature, θ' the perturbation potential temperature, q'_v the perturbation water vapor mixing ratio, and q_l the

condensate mixing ratio.

Generally, the condensate mixing ratio (q_t) consists of the rainwater mixing ratio (q_r) and cloudwater mixing ratio (q_c). Values of q_r can be estimated from radar reflectivity factor (Z) using an empirical formula derived by Hauser and Amayenc (1986):

$$q_r = \frac{(1.73 \times 10^{-3} Z^{0.613})}{\rho_o} \quad (4.14)$$

where q_r is in units of $g\ kg^{-1}$ and Z in $mm^6\ m^{-3}$. The relationship was derived from data collected by an optical spectropluriometer (Hauser *et al.*, 1984) in tropical convection. On the other hand, the cloudwater mixing ratio, q_c , is difficult to estimate accurately. In the TAMEX project, the mean cloudwater content in oceanic convective clouds, measured by P-3 aircraft, was only about $0.5\ g\ kg^{-1}$ (Jorgensen and LeMone, 1989). Therefore, the q_c term is not explicitly treated in this study. Instead, it is combined with the perturbation virtual potential temperature (θ'_v) to yield a virtual cloud potential temperature (Roux *et al.*, 1984), i.e., $\theta'_{vc} = \theta'_v - \theta_{vo} q_c$.

Once the F and G functions are obtained, the horizontal nondimensional perturbation-pressure equation at a given level can be derived from (4.10) and (4.11) to yield

$$\frac{\partial^2 \pi}{\partial x^2} + \frac{\partial^2 \pi}{\partial y^2} = \frac{\partial F}{\partial x} + \frac{\partial G}{\partial y} \quad (4.15)$$

This equation can be solved by using successive overrelaxation with the Neumann boundary condition. The unique solution of (4.15) exists only if the horizontal average is removed from each horizontal plane of π in (4.15), see Gal-Chen (1978). The pressure deviation, P'_d , can then be determined from the nondimensional quantity using the relationship $P'_d = P_{oo}\pi^{C_p/R}$.

Once the field of π is obtained, the deviation-perturbation virtual potential temperature field, θ'_{vd} , can be calculated from the buoyancy equation, i.e.,

$$\theta'_{vd} = \frac{\theta_{vo}}{g} \left\{ c_p \theta_{vo} \frac{\partial \pi}{\partial z} + \left[\frac{Dw}{Dt} - \langle \frac{Dw}{Dt} \rangle \right] + g(q_r - \langle q_r \rangle) + (f_3 - \langle f_3 \rangle) \right\} \quad (4.16)$$

VPG VAC RWL VFF

where terms VPG, VAC, RWL and VFF represent the contributions of vertical perturbation-pressure gradient, vertical acceleration, rainwater loading, and friction to θ'_{vd} where $\langle \rangle$ denotes the horizontal area mean. With the aid of the perturbed potential temperature equation, we obtain $T'_{vd}/T_{vo} = \theta'_{vd}/\theta_{vo}$. Lin *et al.* (1990) justified this approximation since the P'_d/P_o term is much smaller than the other two terms based on their results obtained in the earlier TAMEX study. The retrieved temperature represents a virtual cloud temperature since it accounts for both deviation of virtual temperature perturbation and cloudwater content (Roux *et al.*, 1984).

4.5 Verifications of the Derived Fields

Since the retrieval method proposed by Gal-Chen (1978) is indirect, its effectiveness to a large extent depends on the degree of accuracy in input data. Verifications of the recovered field of pressure and buoyancy perturbations are therefore highly critical. While direct verifications are desirable, they are often difficult to obtain. Consequently, some indirect verifications are needed to justify the derived fields. Gal-Chen and Hane (1981) suggested three indirect verifications: 1) numerical simulations; 2) momentum checking; and 3) time continuity and physical plausibility. Numerical simulations as a guide to verification were performed by Hane *et al.* (1981), while momentum checking and time continuity were used in Doppler studies by Gal-Chen and Kropfli (1984), Roux *et al.* (1984), Brandes (1984), Hane and Ray (1985) and Lin *et al.* (1986) to verify the retrieved fields of thermodynamic variables. The relative error in pressure retrieval is given by the formula:

$$E_r = \frac{\iint \left[\left(\frac{\partial \pi}{\partial x} - F \right)^2 + \left(\frac{\partial \pi}{\partial y} - G \right)^2 \right] dx dy}{\iint (F^2 + G^2) dx dy} \quad (4.17)$$

Momentum checking is often used as a measure of how viable the retrieved pressure gradients are within the domain. If the E_r value exceeds 0.5, the retrieved fields are sometimes considered useless. However, Hane and Ray (1985) pointed out that fields even with E_r values in the neighborhood of 1 can contain highly relevant information. Thus, E_r should only be considered as a relative measure of "goodness" of the perturbation pressure gradients and the

known functions F and G . In this study, values of E_r range from 0.34 to 0.39. It is equally important to examine the physical consistency of thermodynamic perturbations with respect to the storm's kinematic structure at various times and levels. The retrieved fields must be in overall agreement with the fields of vertical velocity, convergence/divergence and vorticity. Further, the retrieved fields should maintain a time continuity from one analysis time to the other. Therefore, one must check the internal consistency of the retrieved fields to determine the level of confidence prior to any physical interpretation.

4.6 Rotated Coordinate System

It is sometimes necessary to orient the domain of interest in a fashion other than the normal 90 degrees plane. Since this rainband had a northeast to southwest alignment at the periods of investigation, it is of necessity to rotate the coordinates with the x' -axis normal to the band, positive in the direction of line movement, and the y' -axis parallel to the band similar to that used by LeMone (1983), see Fig. 4.1. This type of coordinate system is particularly useful for calculation of the total kinetic energy budget, the momentum-flux budget and the vorticity budget in the domain of interest.

4.7 Kinetic Energy Budget

Following the study by Lin and Coover (1988), the kinetic energy equation for a nonhydrostatic system can be written as:

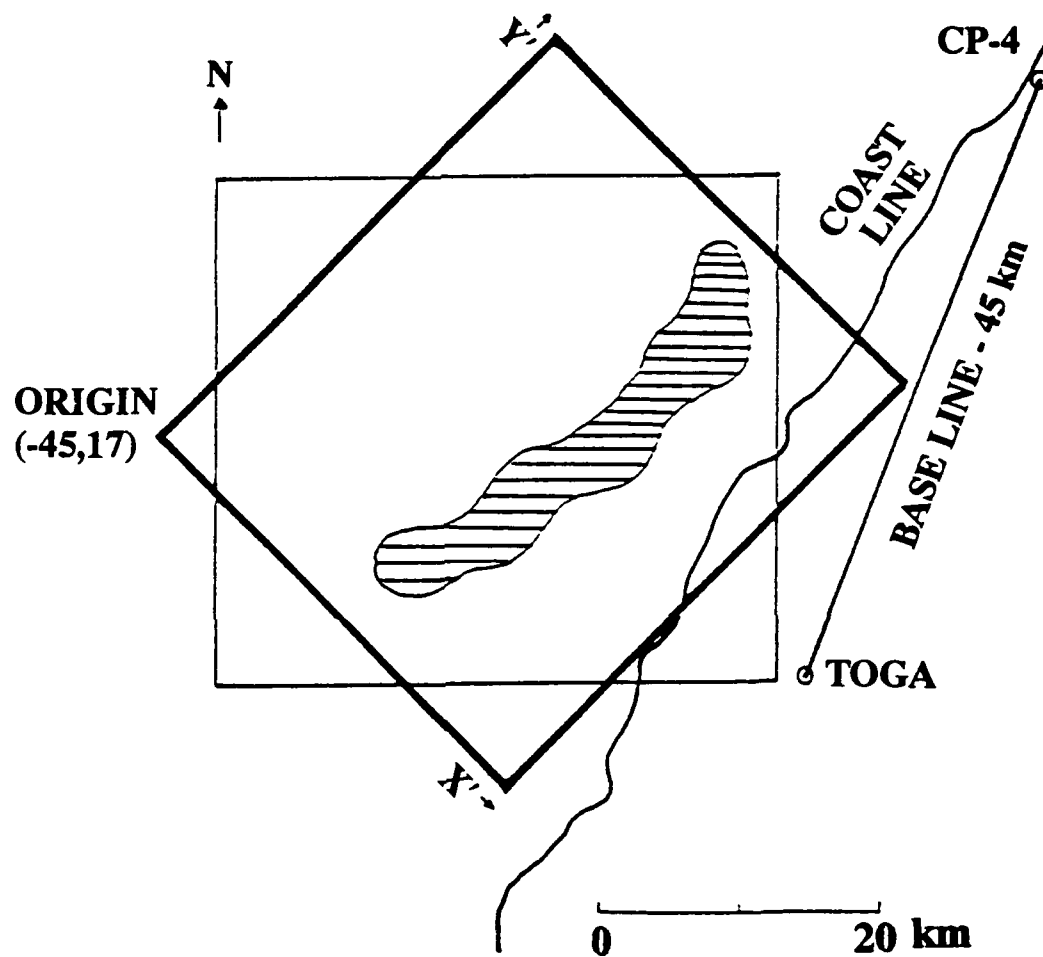


Fig. 4.1 Domain of interest (heavy lined box) for the dual-Doppler analysis rotated by 45 degrees. The origin is located 17 km north and 45 km west of the TOGA radar. The lined contour area represents the pre-frontal convective rainband at the time of investigation. The thin box represents a non-rotated domain in the dual-Doppler coverage area of the CP-4 and TOGA radars. Adapted from Lin *et al.* (1993).

$$\begin{aligned}
 \frac{\partial \overline{\rho_o K_3}}{\partial t} = & \underbrace{- \nabla_h \cdot (\rho_o K_3 \mathbf{V}_h)}_{\text{HFD}} - \underbrace{\frac{\partial \rho_o K_3 w}{\partial z}}_{\text{VFD}} - \underbrace{\nabla_h \cdot \nabla_h P'}_{\text{HGE}} - \underbrace{w \frac{\partial P'}{\partial z}}_{\text{VGE}} \\
 & + \underbrace{\overline{\rho_o g w \left(\frac{T'_v}{T_w} - q_l \right)}}_{\text{BUP}} + \underbrace{\overline{\rho_o \mathbf{V} \cdot \mathbf{F}}}_{\text{FDI}}
 \end{aligned} \quad (4.18)$$

where $\overline{(\quad)} = \langle (\quad) \rangle = \frac{1}{\text{Area}} \iint (\quad) dx dy$, $K_3 = \frac{(u^2 + v^2 + w^2)}{2}$ is the total kinetic energy per unit mass, the subscript o represents the environmental mean, the prime denotes the deviation from the environmental mean, and other symbols have their conventional meanings. Terms on the right-hand side of (4.18) represent the horizontal flux divergence (HFD), the vertical flux divergence (VFD), the horizontal generation (HGE), the vertical generation (VGE), the total buoyancy production (BUP) (which is comprised of thermal buoyancy (called BUO in later discussions) and precipitation loading (the q_l portion)), and the frictional dissipation (FDI) of kinetic energy, respectively. FDI is determined using Austausch hypothesis with constant exchange coefficients. This allows us to use the dual-Doppler derived wind components for computing friction.

As shown by Lin and Coover (1988), VGE can be approximated by

$$\begin{aligned}
 - \langle w \frac{\partial P'}{\partial z} \rangle & = - \langle w \frac{\partial P'_d}{\partial z} \rangle - \langle w \rangle \frac{\partial \langle P' \rangle}{\partial z} \\
 & = - \langle w \frac{\partial P'_d}{\partial z} \rangle .
 \end{aligned} \quad (4.19)$$

The thermal buoyancy portion (BUO) of the BUP term can be approximated by

$$\begin{aligned} \frac{\rho_o g}{T_{vo}} \langle w T'_v \rangle &= \frac{\rho_o g}{T_{vo}} (\langle w T'_{vd} \rangle + \langle w \rangle \langle T'_v \rangle) \\ &\approx \frac{\rho_o g}{T_{vo}} \langle w T'_{vd} \rangle. \end{aligned} \quad (4.20)$$

where P'_d and T'_{vd} represent deviation perturbation pressure and virtual temperature, respectively and are defined as $P'_d = P' - \langle P' \rangle$ and $T'_{vd} = T'_v - \langle T'_v \rangle$ (Gal-Chen 1978), where $\langle \rangle$ is the height-dependent area mean averaged over the domain of interest.

Since, the unknown area means, $\partial \langle P' \rangle / \partial z$ and $\langle T'_v \rangle$, are nonzero (which vary with height), the validity of (4.19) and (4.20) depends on the area-mean of vertical velocity, $\langle w \rangle$, going to zero or remaining very small. For a typical convective storm with updrafts and downdrafts in coexistence, the $\langle w \rangle$ value, averaged over the whole horizontal domain, should be much smaller than magnitudes of the convective updrafts and downdrafts at a given height. Results have confirmed that the maximum value of $\langle w \rangle$ is only about 1.1 m s^{-1} from 4 to 5 km and becomes much smaller in the layers above and below, whereas the extreme values of w range from -5 to 9 m s^{-1} for most convective cells embedded within the rainband during the time period under investigation.

4.8 Momentum-flux Budget Calculation

Following the study by LeMone (1983) and Lin and Condray (1988), the momentum-flux generation equations can be derived from the momentum equations in a moving coordinate system (x,y,z,t):

$$\begin{aligned}
 \frac{\partial \overline{u'w'}}{\partial t} = & \underbrace{-\overline{w'^2} \frac{\partial \overline{U}(z)}{\partial z}}_A - \underbrace{\frac{1}{\rho_o} \frac{\partial}{\partial z} (\rho_o \overline{u'w'^2})}_B + \underbrace{\left[\frac{g}{T_{\infty}} \overline{u'T'_v} - \overline{gu'q'_l} \right]}_C \\
 & - \underbrace{\left\{ \frac{w'}{\rho_o} \frac{\partial P'}{\partial x} + \frac{u'}{\rho_o} \frac{\partial P'}{\partial z} \right\}}_D - \underbrace{\left\{ \frac{\partial}{\partial x} (\overline{U(z)u'w'}) + \frac{\partial}{\partial x} (\overline{u'^2 w'}) \right\}}_E \\
 & - \underbrace{\left\{ \frac{\partial}{\partial y} (\overline{V(z)u'w'}) + \frac{\partial}{\partial y} (\overline{u'v'w'}) \right\}}_F - \underbrace{\frac{1}{\rho_o} \left\{ \frac{\partial}{\partial z} (\overline{W(z)\rho_o u'w'}) \right\}}_G \\
 & + \underbrace{\left\{ f \overline{v'w'} + f^* (\overline{u'^2} - \overline{w'^2}) \right\}}_H
 \end{aligned} \tag{4.21}$$

where $f = 2\Omega \sin \phi$, $f^* = 2\Omega \cos \phi$. Each wind component is decomposed into two parts, i.e., $u = \bar{U} + u'$, etc. The prime represents the perturbation quantity. The over-bar denotes the quantity of the ensemble mean (which is a function of height only). Term A is the mechanical production of u-momentum flux from

vertical mean shear, term B is the source of momentum flux from the vertical divergence of transport of u-momentum flux, term C is the total buoyancy production (including thermal buoyancy and precipitation loading), term D is the production and destruction of eddy stress by velocity-pressure interactions, term E is the source of momentum flux from the horizontal divergence of u-transport, term F is the source of momentum flux from the horizontal divergence of v-transport, term G is the source of momentum flux from the vertical divergence of w-transport, term H is the contribution due to Coriolis terms. The $\partial \overline{u'w'}/\partial t$ term is the local time change of u-momentum flux and is calculated as a residual term based on the sum of the other terms. According to LeMone (1983) and Lin and Condray (1988), terms A through D in (4.21) are the most dominant terms and are one order of magnitude greater than terms E through H.

Equation (4.21) is a complete form of the u-momentum flux generation equation. Caution must be exercised in interpreting the retrieved field. It is the deviation from the area mean rather than the deviation from the environmental mean as explained in the study by Gal-Chen (1978), i.e.,

$$P'_d = P' - \langle P' \rangle ; \quad T'_{vd} = T'_v - \langle T'_v \rangle \quad (4.22)$$

where $\langle \rangle$ denotes the height-dependent area mean. In this study, the system is nearly in a quasi-steady state, at the times of investigation, hence the ensemble mean $\overline{(\quad)}$ is equivalent to the area mean $\langle \rangle$ at each analysis level.

In a similar manner, the momentum-flux generation equation for the v -component was derived:

$$\begin{aligned}
 \frac{\partial \overline{v'w'}}{\partial t} = & -\overline{w'^2} \frac{\partial \overline{V}(z)}{\partial z} - \frac{1}{\rho_o} \frac{\partial}{\partial z} (\rho_o \overline{v'w'^2}) + \left[\frac{g}{T_{vo}} \overline{v'T'_v} - g \overline{v'q'_l} \right] \\
 & - \left\{ \frac{w'}{\rho_o} \frac{\partial P'}{\partial y} + \frac{v'}{\rho_o} \frac{\partial P'}{\partial z} \right\} - \left\{ \frac{\partial}{\partial x} (\overline{U(z)v'w'}) + \frac{\partial}{\partial x} (\overline{u'v'w'}) \right\} \\
 & - \left\{ \frac{\partial}{\partial y} (\overline{V(z)v'w'}) + \frac{\partial}{\partial y} (\overline{v'^2 w'}) \right\} - \frac{1}{\rho_o} \left\{ \frac{\partial}{\partial z} (\overline{W(z)\rho_o v'w'}) \right\} \\
 & + (f * \overline{u'v'} - f \overline{u'w'})
 \end{aligned} \tag{4.23}$$

The terms of the momentum-flux budget were calculated using finite differencing techniques. Since the budget calculation is sensitive to the computational error from the finite differencing scheme only centered differencing was used in the budget calculation. Values of P' and T'_v (in 4.21 and 4.23) can be replaced by P'_d and T'_{vd} whenever they appear in differentiated form (Lin and Condray, 1988). The environmental virtual temperature, T_{vo} , can be extracted from a nearby environmental sounding, in this case the Makung sounding.

4.9 Vorticity Budget Calculation

The vorticity equation in vector form is obtained by taking the curl of the

equation of motion in vector form. On the convective scale, the effect the rotation of the earth has on the absolute vorticity is small. Thus, one obtains the expression for the relative vorticity along the vertical axis:

$$\begin{aligned}
 \frac{\partial \zeta}{\partial t} = & \underbrace{-\overline{\mathbf{V}_h \cdot \nabla_h \zeta}}_A - \underbrace{\overline{w \frac{\partial \zeta}{\partial z}}}_B - \underbrace{\overline{\zeta \left\{ \nabla_h \cdot \mathbf{V}_h + \frac{\partial w}{\partial z} \right\}}}_C + \underbrace{\overline{\left\{ \xi \frac{\partial w}{\partial x} + \eta \frac{\partial w}{\partial y} + \zeta \frac{\partial w}{\partial z} \right\}}}_D \\
 & - \underbrace{\overline{\left\{ \frac{\partial \alpha}{\partial x} \frac{\partial p}{\partial y} - \frac{\partial \alpha}{\partial y} \frac{\partial p}{\partial x} \right\}}}_E + \underbrace{\overline{\left\{ \frac{\partial f_y}{\partial x} + \frac{\partial f_x}{\partial y} \right\}}}_F
 \end{aligned} \tag{4.24}$$

where $\xi = \frac{\partial w}{\partial y} - \frac{\partial v}{\partial z}$, the x-component relative vorticity;

$\eta = \frac{\partial u}{\partial z} - \frac{\partial w}{\partial x}$, the y-component relative vorticity;

and $\zeta = \frac{\partial v}{\partial x} - \frac{\partial u}{\partial y}$, the z-component relative vorticity.

Terms A through F in (4.24) represent the horizontal vorticity advection term, vertical vorticity advection term, divergence term, tilting/tipping term, solenoid term, and the friction term. The solenoid term requires retrieved information derived from the Doppler-wind data and is subject to larger uncertainty, therefore will not be investigated here. The remaining terms can be determined from the three wind components and their spatial derivatives. The friction term is generally one order of magnitude smaller than the remaining terms but will

be calculated using the three wind components and Austuasch hypothesis with constant exchange coefficients to determine if that is the case.

Similarly, the x- and y- component vorticity equations can be obtained as follows:

$$\begin{aligned} \frac{\partial \xi}{\partial t} = & - \overline{\mathbf{V}_h \cdot \nabla_h \xi} - \overline{w \frac{\partial \xi}{\partial z}} - \overline{\xi \left\{ \nabla_h \cdot \mathbf{V}_h + \frac{\partial w}{\partial z} \right\}} + \overline{\left\{ \xi \frac{\partial w}{\partial x} + \eta \frac{\partial u}{\partial y} + \zeta \frac{\partial u}{\partial z} \right\}} \\ & - \overline{\left\{ \frac{\partial \alpha}{\partial y} \frac{\partial p}{\partial z} - \frac{\partial \alpha}{\partial z} \frac{\partial p}{\partial y} \right\}} + \overline{\left\{ \frac{\partial f_z}{\partial y} + \frac{\partial f_y}{\partial z} \right\}} \end{aligned} \quad (4.25)$$

$$\begin{aligned} \frac{\partial \eta}{\partial t} = & - \overline{\mathbf{V}_h \cdot \nabla_h \eta} - \overline{w \frac{\partial \eta}{\partial z}} - \overline{\eta \left\{ \nabla_h \cdot \mathbf{V}_h + \frac{\partial w}{\partial z} \right\}} + \overline{\left\{ \xi \frac{\partial v}{\partial x} + \eta \frac{\partial v}{\partial y} + \zeta \frac{\partial v}{\partial z} \right\}} \\ & - \overline{\left\{ \frac{\partial \alpha}{\partial z} \frac{\partial p}{\partial x} - \frac{\partial \alpha}{\partial x} \frac{\partial p}{\partial z} \right\}} + \overline{\left\{ \frac{\partial f_x}{\partial z} + \frac{\partial f_z}{\partial x} \right\}} \end{aligned} \quad (4.26)$$

A fourth-order finite differencing scheme will be applied in the horizontal and a second-order finite differencing scheme will be used in the vertical to obtain an estimate for each of the remaining terms. The magnitude of these terms can then be determined by taking their respective area means and standard deviations over the domains of interest. The vorticity budget in three directions can be studied using these results.

HAD is the horizontal advection of the vorticity component in question, while VAD is simply the vertical advection of that quantity. For a given flow in a quasi-steady state flow field, these terms will be largest in the regions of tightest vorticity gradients. DIV represents the generation (positive) of the respective vorticity component through convergence and the last term, TILT, represents the generation of vorticity by tilting the vorticity vector into the respective positive axial direction. These abbreviations for these terms will be used throughout the discussion.

Chapter 5

Discussion of Results

This chapter provides a detailed discussion of the results found in the determination of the three budgets. The first section deals with the total kinetic energy budget. This will include a look at the horizontal variations of several terms within the kinetic energy equation (4.18), an analysis of the budget and a discussion of the vertical totals of the budget terms. Section 5.2 will detail the momentum-flux budget which will also include a section about the u- and v-components of momentum flux and the vertical variation of the mean three-dimensional winds within the domain of interest. The final section will be a discussion pertaining to the vorticity budget. A look at the horizontal vorticity vectors and pertinent local variations of each vorticity component term will be presented to aid in the discussion of the vorticity budget.

The 0653 and 0700 LST 25 June 1987 volume scans of Doppler radar data from the CP-4 and TOGA radars were used as the source of data for these budget studies. A minus 45-degree rotated dual-Doppler data set covering a horizontal domain of 35 km by 40 km with a three-dimensional grid spacing of 1 km was processed for both volume scans. The domain of interest for the budget studies was reduced to a 25 km by 40 km horizontal domain to eliminate some data fields in the stratiform region that would not be representative of the prefrontal convective rainband processes.

5.1 Total Kinetic Energy Budget

This total kinetic energy budget study is based upon the kinetic energy equation (4.18) for a non-hydrostatic system. The non-hydrostatic form of the kinetic energy equation can be used because of the fine resolution of the TAMEX data set. Each term of (4.18) can be determined and studied to evaluate its contribution to the total kinetic energy of the investigated mesoscale convective system, in this case, a prefrontal convective rainband off the northwest coast of Taiwan. A look at the horizontal variations of the most dominant terms will not only unveil several interesting features but provide a sound basis as to the reliability of the budget analysis results.

5.1.1 Horizontal Variations of Kinetic Energy

Horizontal variations of the dominating terms comprising the total kinetic energy equation (4.18) reveal several interesting features. The area of integration in determining these local variations of the terms is one grid space (1 km by 1 km). The three analysis levels chosen for discussion are 0.75 km, 3.75 km and 6.75 km. These levels are well representative of the low, middle and upper levels, respectively. Both volume scans (0653 and 0700 LST) revealed similar features therefore only the 0653 LST volume scan will be displayed. Figures 5.1 and 5.2 show the horizontal system-relative winds with reflectivity contours superimposed and horizontal distributions of HFD at 0.75 km. Positive areas (convergence) of HFD were generally located in high reflectivity

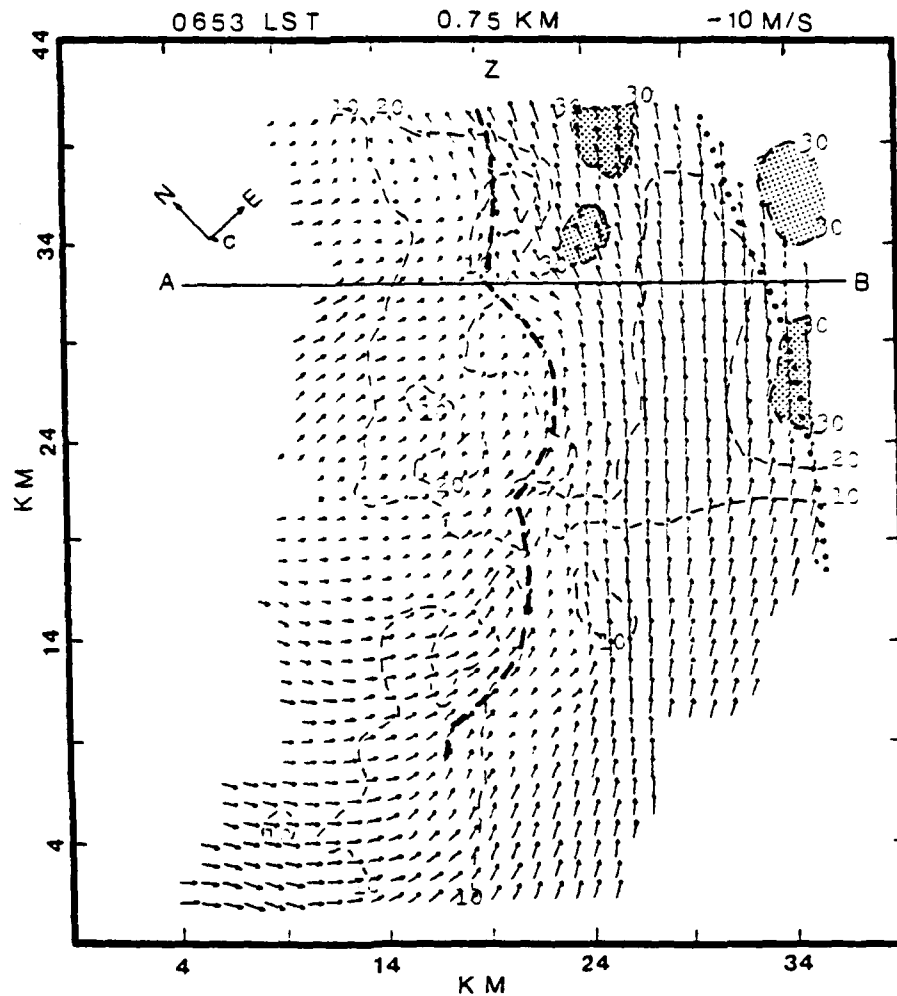


Fig. 5.1 The system-relative horizontal wind field with reflectivity contours Z superimposed at 0.75 km for 0653 LST 25 June 1987. The x-axis is positive towards the southeast and the y-axis is positive towards the northeast. Reflectivities greater than 30 dBZ are shaded. Positions of the Mei-Yu front wind-shift line (heavy dashed line) and the gust front (dotted line) are depicted. North (N), east (E) and system motion (c) are indicated in the top left corner (after Lin *et al.*, 1993).

0653 LST 25 June 1987 Ht = 0.75 km dx = 1.0 km

HFD

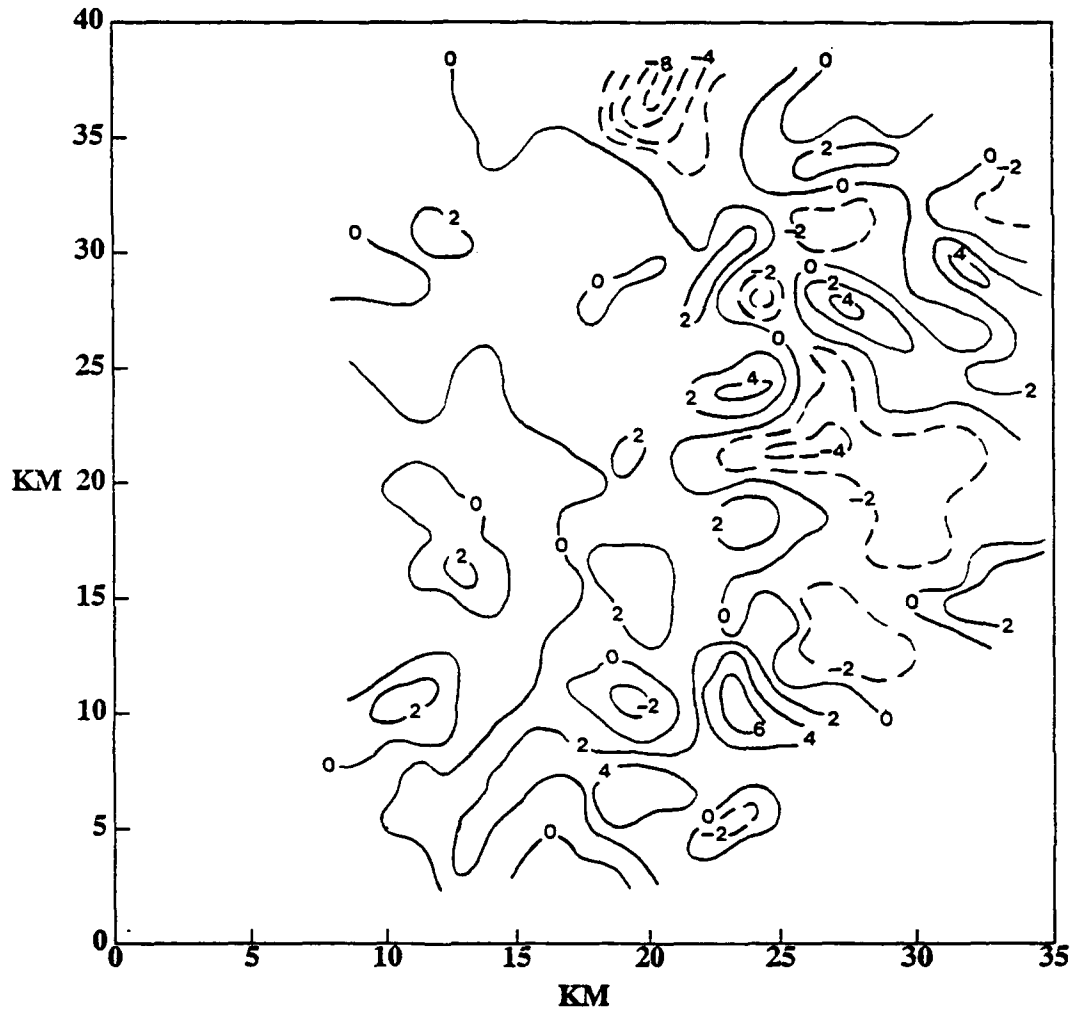


Fig. 5.2 Horizontal distribution of the horizontal flux divergence (HFD) of kinetic energy at 0.75 km for 0653 LST 25 June 1987. The x-axis is positive towards the southeast and the y-axis is positive towards the northeast. Distances from the rotated-domain origin are in kilometers. Units are in $10^{-1} W m^{-3}$. Contour interval is $2 \times 10^{-1} W m^{-3}$ with negative values dashed.

areas and along the windshift line (heavy dashed line in Fig. 5.1) where convergence is taking place. On the other hand, negative values (divergence) of HFD were located between the main cells and behind (to the northwest) the windshift line. Also, at this level, HFD and VFD had the same order of magnitude but were opposite in sign throughout the entire domain of interest. HFD and VFD were found to be in quasi-balance at most levels. This will be discussed later in this section and later in the budget calculations.

Figures 5.3 and 5.4 display vertical velocities and VFD at 0.75 km for 0653 LST. Comparing features in these two figures, VFD is negative (flux divergence) in areas of the upward vertical motion along the windshift line. Analyzing the vertical velocity fields at 1.75 km (not shown), this is where the upward vertical motion increased with height. Flux convergence (positive VFD values) generally occurred in areas of downward vertical motion, mainly to the southeast of the main cells. At this level, positive (negative) centers of HFD matched up well with the negative (positive) centers of VFD. The VFD centers were slightly weaker but this feature displays the quasi-balance of these two terms. The 0.75 km horizontal distribution of the thermal buoyancy (BUO) portion of the total buoyancy production term (BUP) is displayed in Fig. 5.5. Values are generally positive throughout the domain but the overall magnitudes of BUO are weaker than both VFD and HFD at this level.

Examination of the horizontal distributions of HFD and VFD at 3.75 km reveal similar tendencies that were found at the 0.75 km level. Figures 5.6

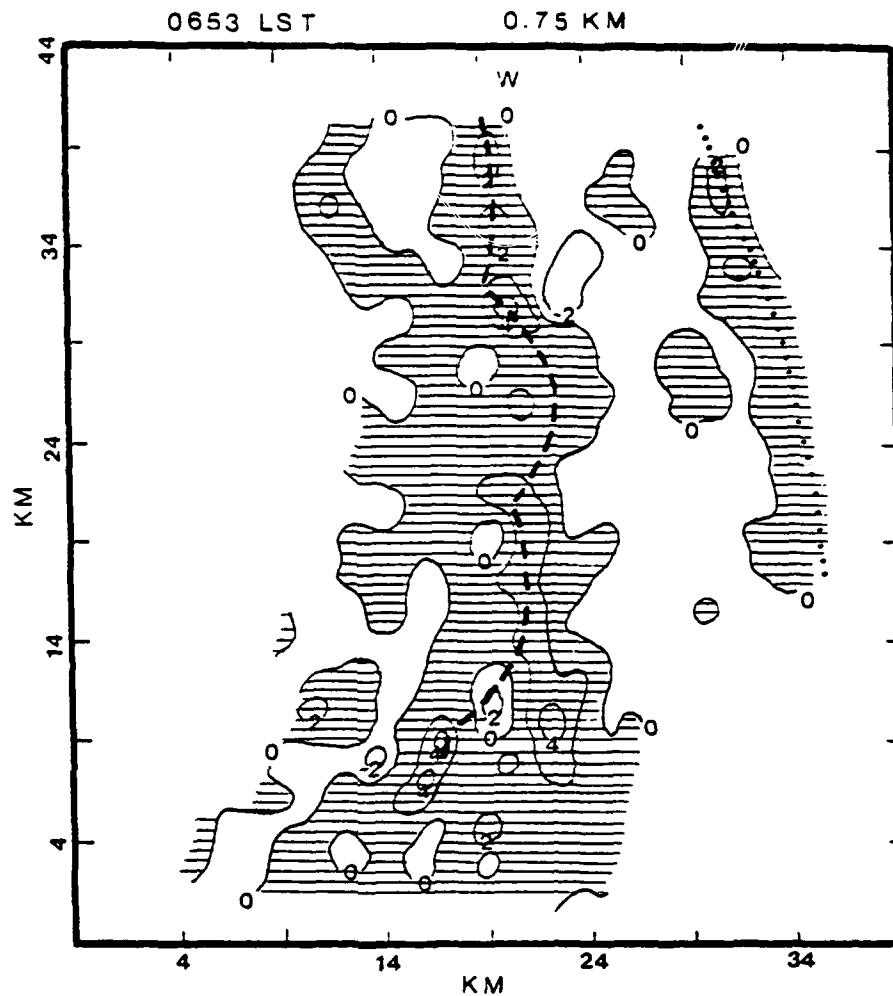


Fig. 5.3 Horizontal distribution of vertical velocity, w , at 0.75 km for 0653 LST 25 June 1987. The x-axis is positive towards the southeast and the y-axis is positive towards the northeast. Contour interval is 2 m s^{-1} with positive values hatched. Positions of the Mei-Yu front wind-shift line (heavy dashed line) and the gust front (dotted line) are depicted. Adapted from Lin *et al.* (1993).

0653 LST 25 June 1987 Ht = 0.75 km dx = 1.0 km

VFD

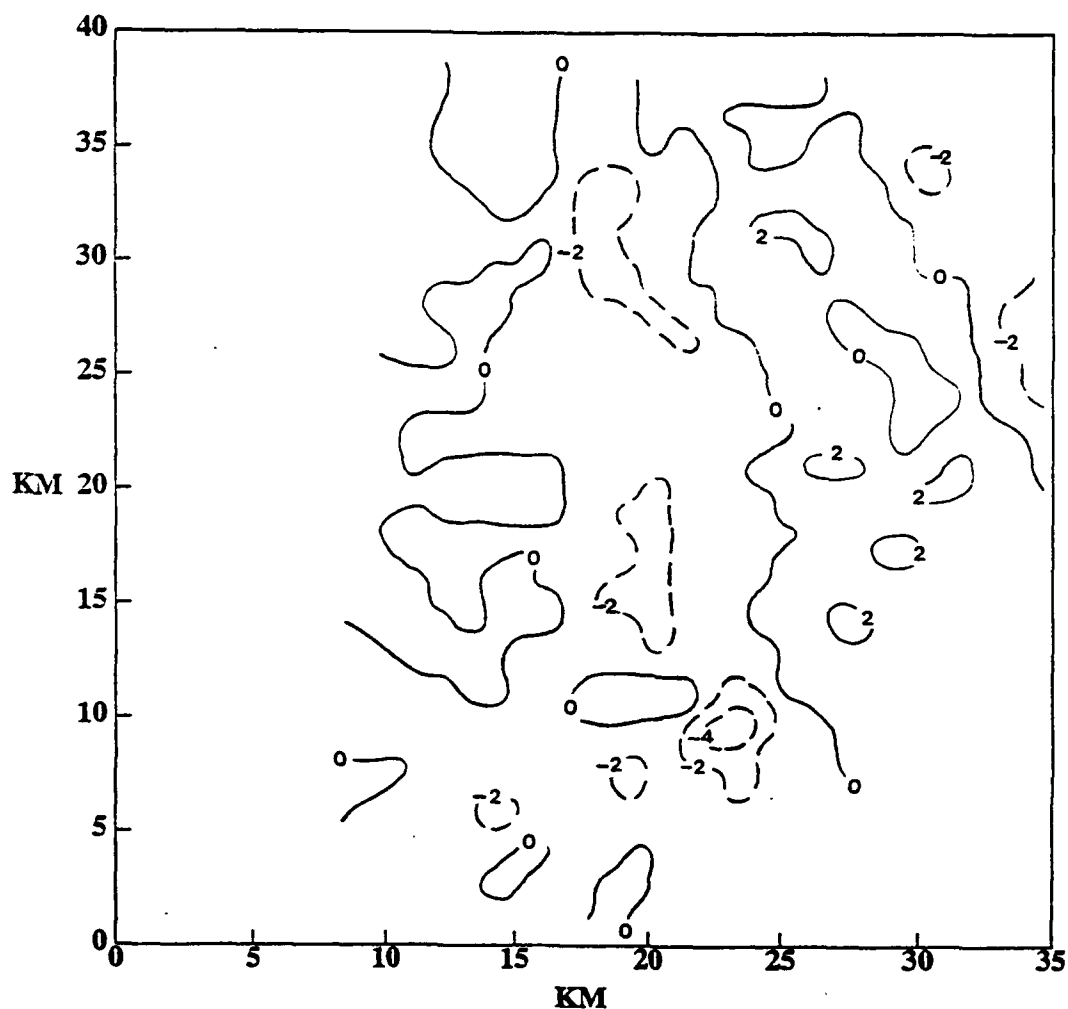


Fig. 5.4 Horizontal distribution of the vertical flux divergence (VFD) of kinetic energy at 0.75 km for 0653 LST 25 June 1987. The x-axis is positive towards the southeast and the y-axis is positive towards the northeast. Distances from the rotated-domain origin are in kilometers. Units are in $10^{-1} W m^{-3}$. Contour interval is $2 \times 10^{-1} W m^{-3}$ with negative values dashed.

0653 LST 25 June 1987 Ht = 0.75 km dx = 1.0 km

BUO

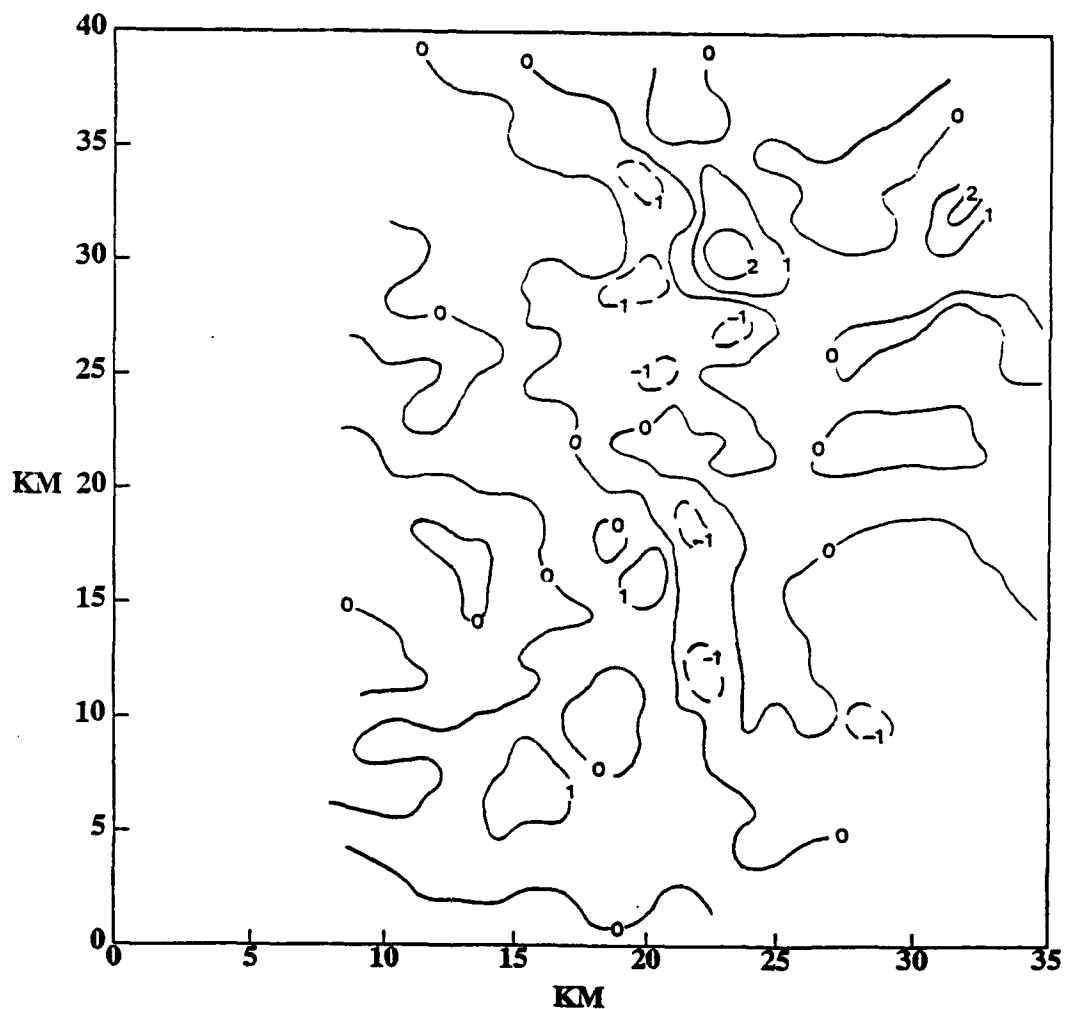


Fig. 5.5 Horizontal distribution of thermal buoyancy production (BUO) of kinetic energy at 0.75 km for 0653 LST 25 June 1987. The x-axis is positive towards the southeast and the y-axis is positive towards the northeast. Distances from the rotated-domain origin are in kilometers. Units are in $10^{-1} W m^{-3}$. Contour interval is $1 \times 10^{-1} W m^{-3}$ with negative values dashed.

through 5.10 show the same basic features for the middle level that Figs. 5.1 through 5.5 displayed for the low levels. Overall values of the positive (negative) centers for both HFD and VFD increased by $\pm 2 \times 10^{-1} W m^{-3}$ as compared to the lower level. Again, careful comparison of these two terms indicate a near balance throughout the domain. The horizontal distribution of BUO is depicted in Fig. 5.10. Positive values dominate through the entire domain with several stronger positive centers ($2-4 \times 10^{-1} W m^{-3}$) located near the updraft cores (see Fig. 5.8 for updraft cores). A positive value of BUO occurs when warm air rises and cool air sinks. Thus, due to the warmer air ascending within the updraft cores (Lin *et al.*, 1993), the BUO term acts as a strong source of kinetic energy at this level. These local variations of HFD, VFD and BUO at the middle levels are similar to those found by Lin *et al.* (1991) in their study of a squall line during TAMEX IOP-2.

Looking at 6.75 km, Figs. 5.11 through 5.14 reveal a significant change in the horizontal variations of HFD and VFD. At this level, negative values (divergence) of HFD (see Fig. 5.12) coincide with the highest reflectivity areas (see Fig. 5.11) and positive values (convergence) of HFD are now upstream (west to southwest) of the main cells, as well as between the cells. This is opposite to the lower and middle levels. The flux divergence from the two main cells is likely the cause of the flux convergence in the area between them. The VFD features illustrated in Fig. 5.14 continues to reveal the quasi-balance between HFD and VFD. VFD is mainly positive at this level implying flux

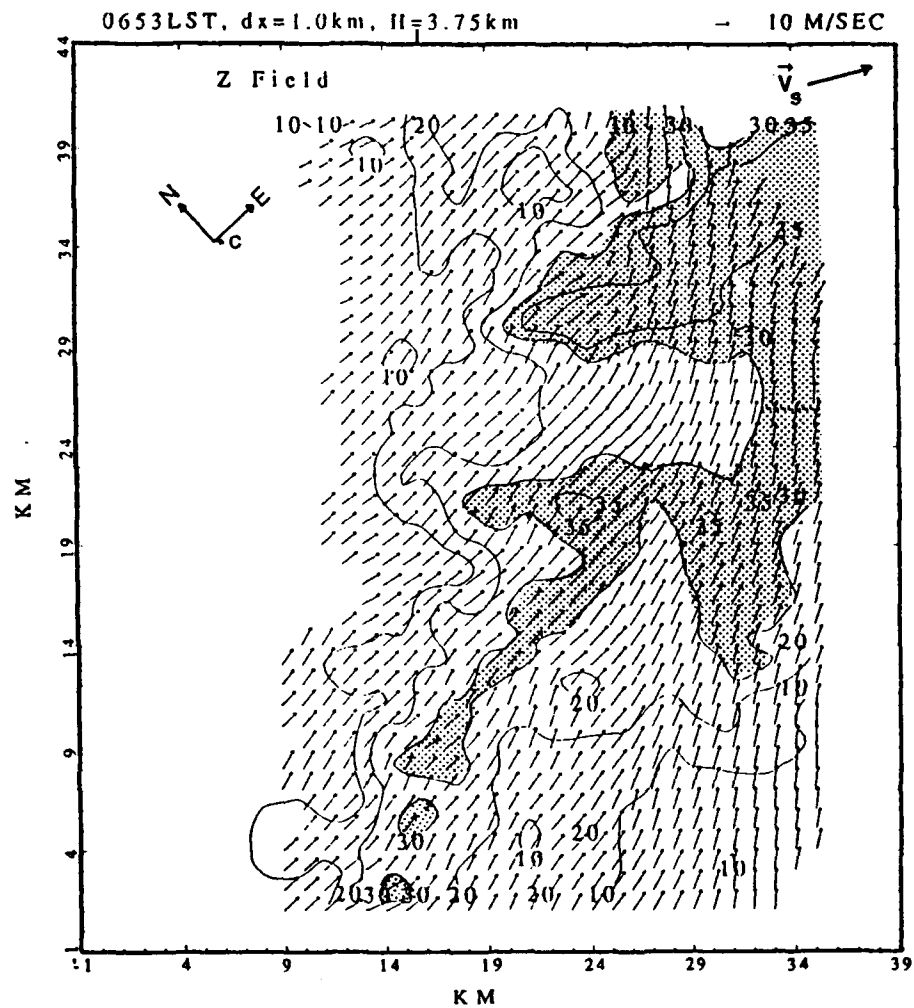


Fig. 5.6 Same as in Fig. 5.1 except for 3.75 km and the positions of the wind-shift line and the gust front are not shown. The environmental shear vector, depicted by the \vec{V}_s in the top right corner, is from 300 ° at this level.

0653 LST 25 June 1987 Ht = 3.75 km dx = 1.0 km

HFD

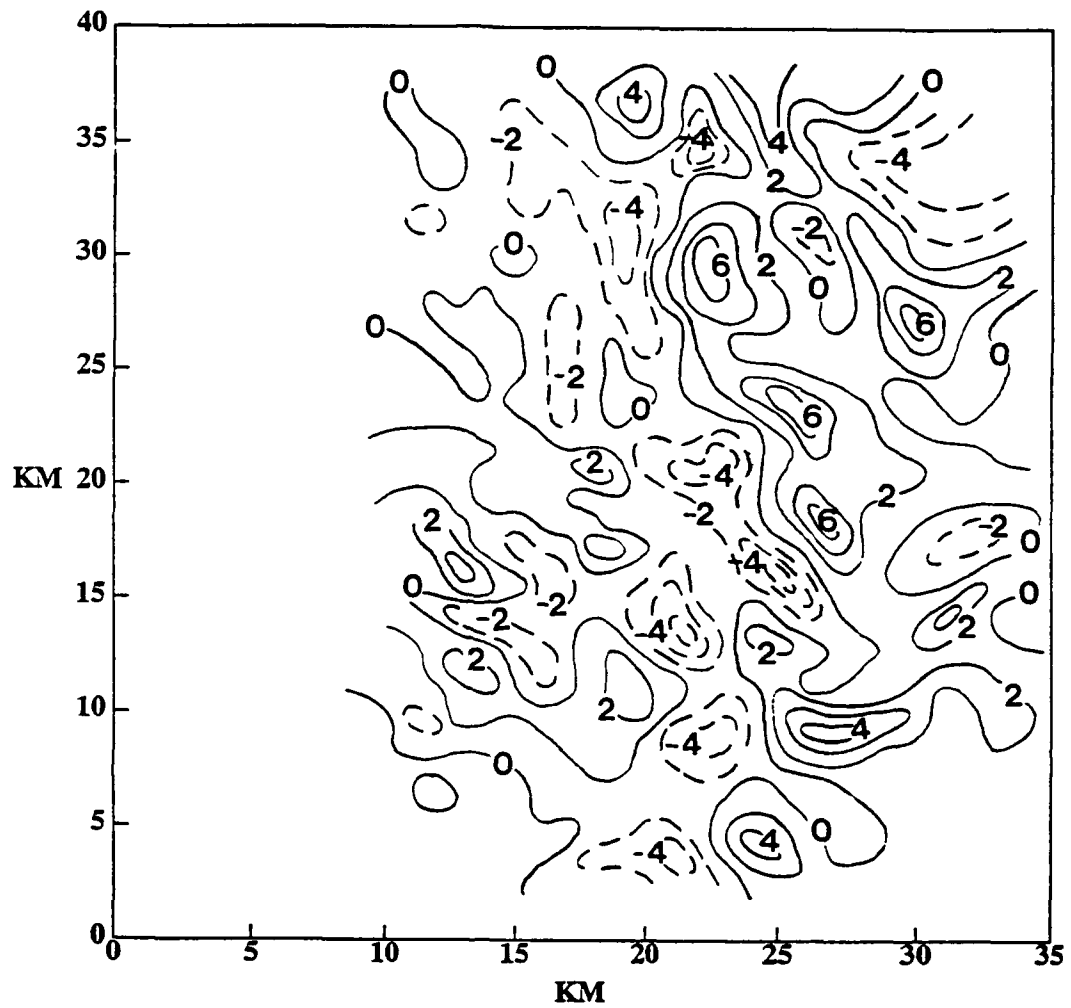


Fig. 5.7 Same as in Fig. 5.2 except for 3.75 km.

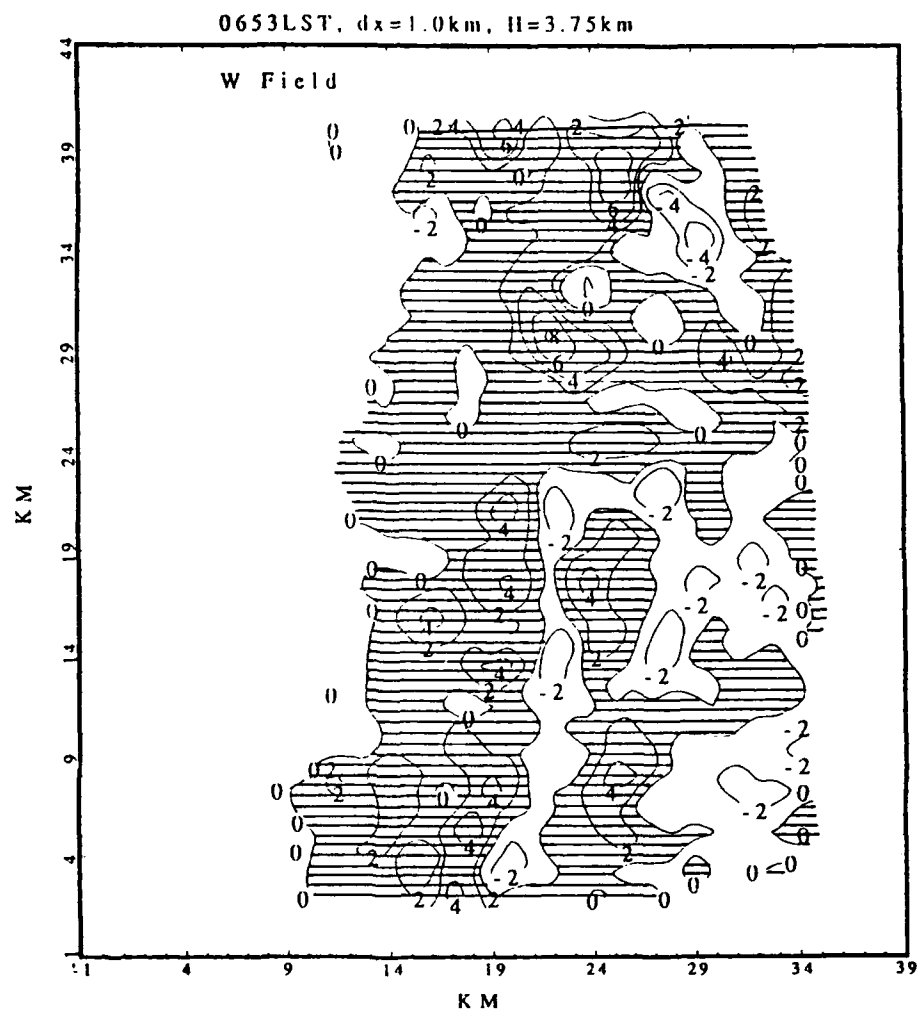


Fig. 5.8 Same as in Fig. 5.3 except for 3.75 km.

0653 LST 25 June 1987 Ht = 3.75 km dx = 1.0 km

VFD

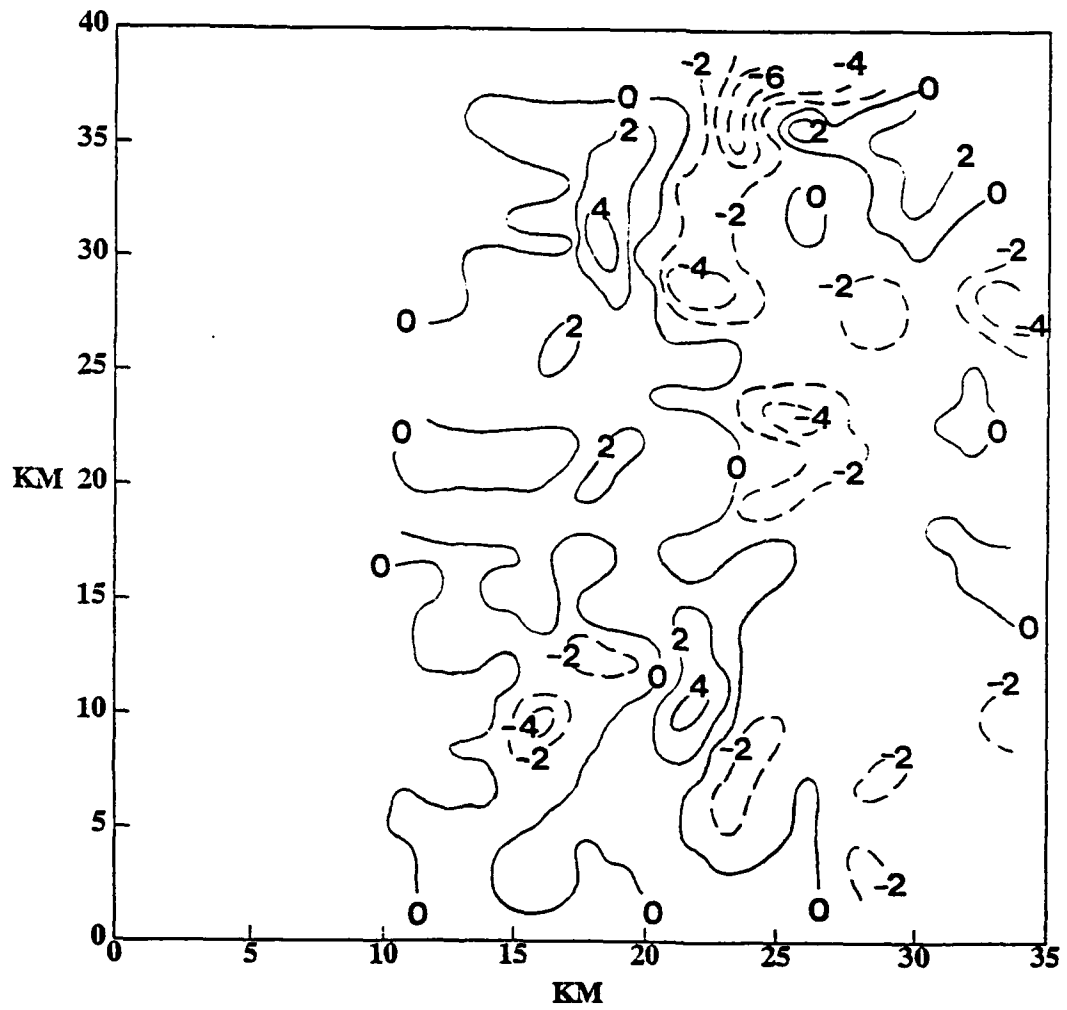


Fig. 5.9 Same as in Fig. 5.4 except for 3.75 km.

0653 LST 25 June 1987 Ht = 3.75 km dx = 1.0 km

BUO

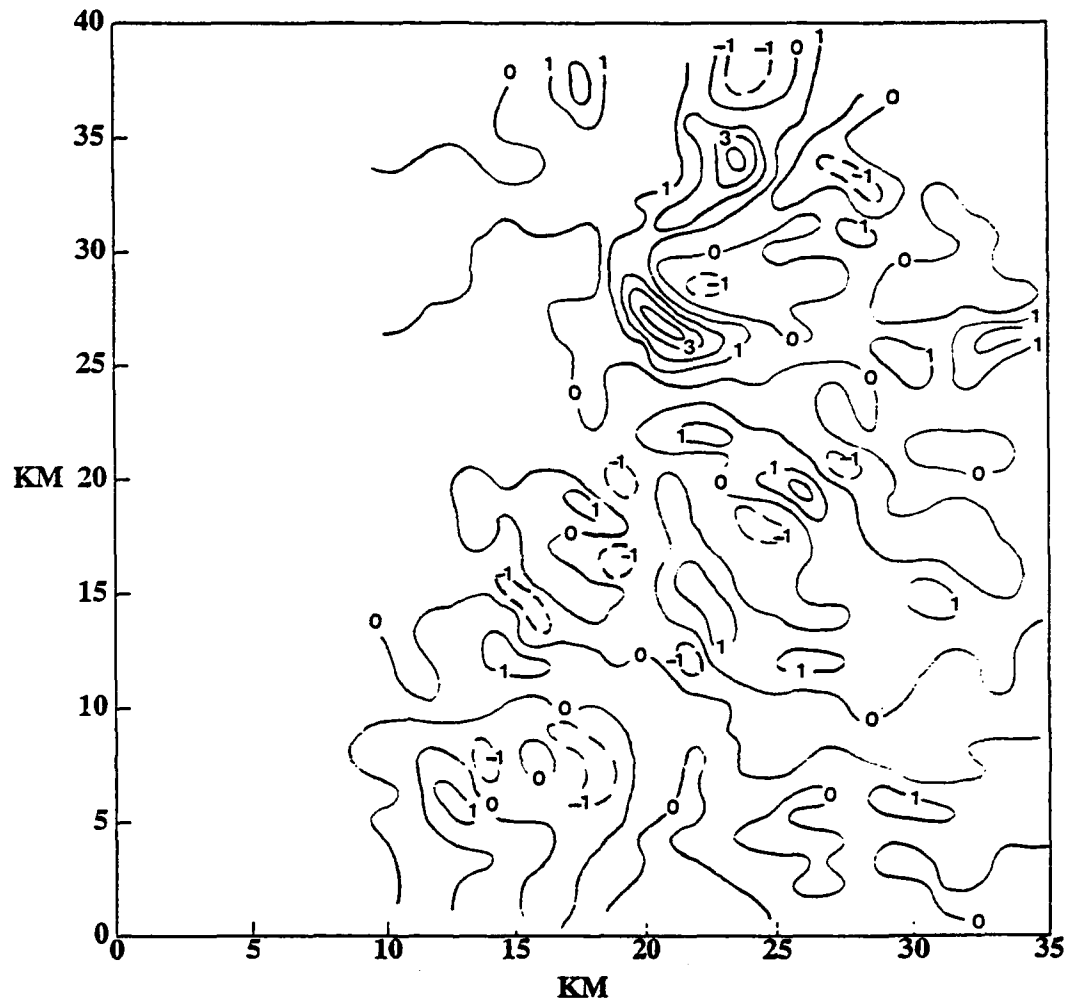


Fig. 5.10 Same as in Fig. 5.5 except for 3.75 km.

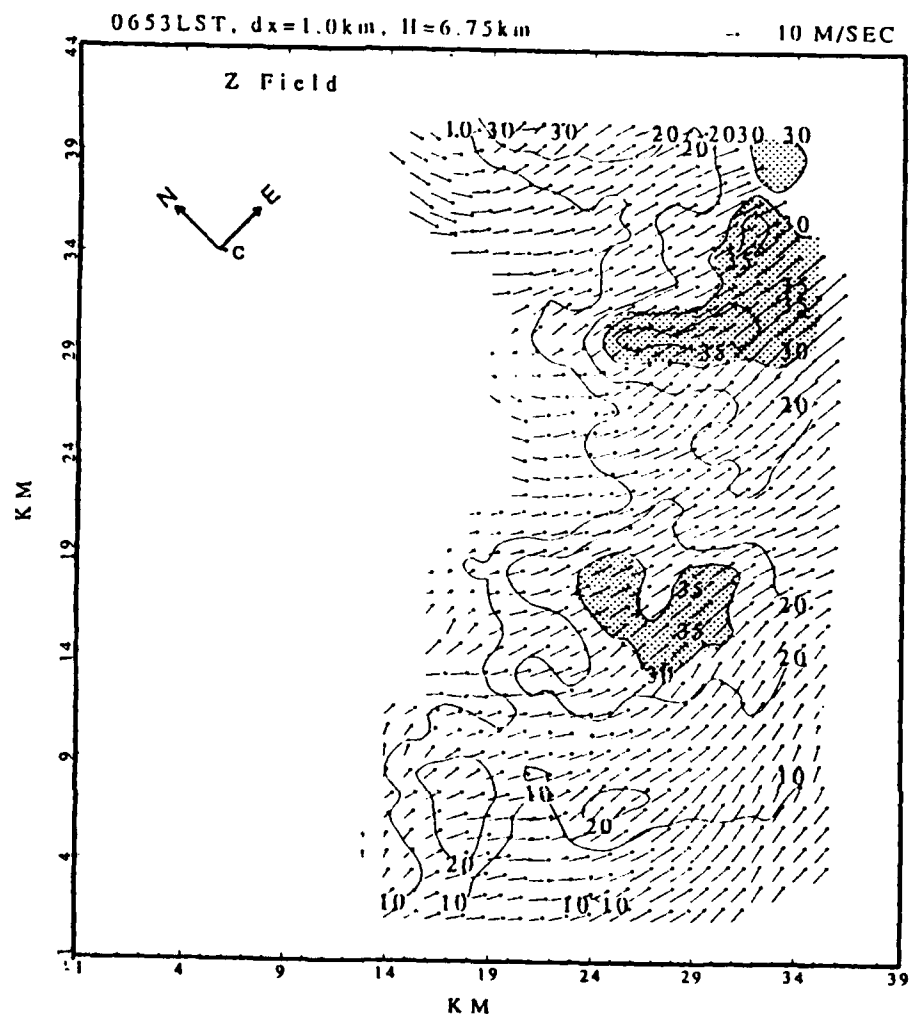


Fig. 5.11 Same as in Fig. 5.1 except for 6.75 km and the positions of the wind-shift line and the gust front are not shown.

0653 LST 25 June 1987 Ht = 6.75 km dx = 1.0 km

HFD

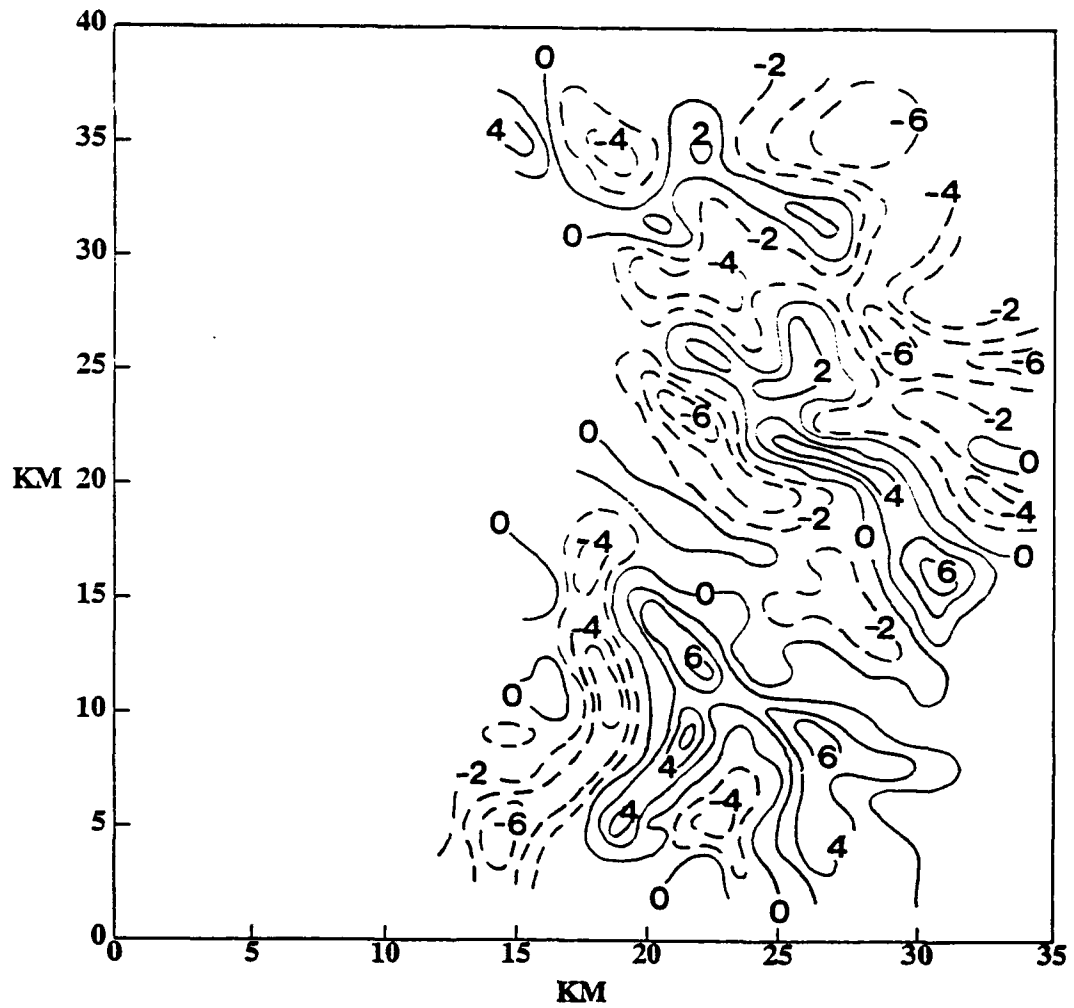


Fig. 5.12 Same as in Fig. 5.2 except for 6.75 km.

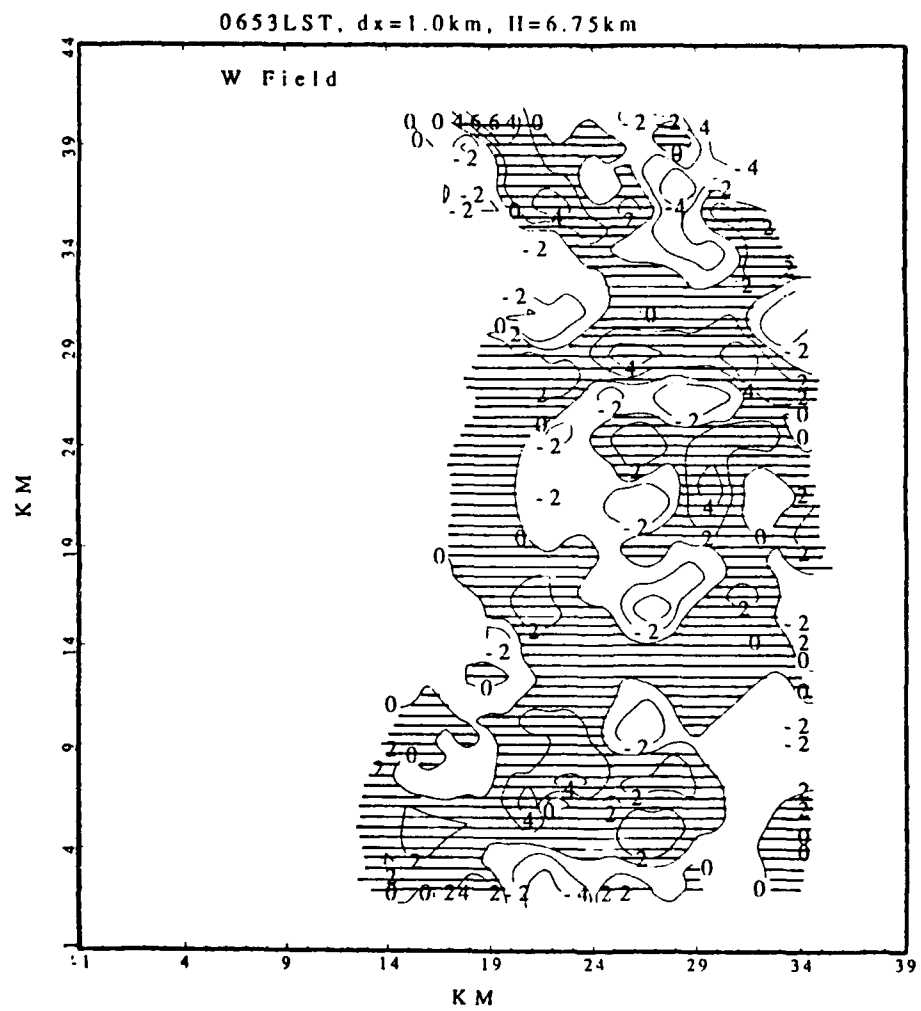


Fig. 5.13 Same as in Fig. 5.3 except for 6.75 km.

convergence throughout the domain. This is likely due to the updrafts becoming weaker towards the storm top (see Fig. 5.14). Figure 5.15 shows the BUO local variation at 6.75 km. Negative values begin to dominate since warmer air is beginning to descend within the downdrafts.

5.1.2 Kinetic Energy Budget Analysis

Budgets of the total kinetic energy, per unit volume, were calculated from (4.18) by integrating over a $25 \times 40 \text{ km}^2$ horizontal domain at each analysis level for both 0653 and 0700 LST volume scans. Findings revealed that the overall kinetic energy budgets were quite comparable and consistent for both analysis times. The following budget results were based upon both volume scans. Figure 5.16 shows vertical profiles of the horizontal flux divergence (HFD) term and the vertical flux divergence (VFD) term of kinetic energy in units of 10^{-3} W m^{-3} . A positive (negative) value represents flux convergence (divergence). The HFD profile indicates flux convergence below 4.25 km and flux divergence throughout the layers above 4.25 km. Conversely, VFD is negative below 4 km indicating flux divergence and positive (flux convergence) above 4 km. Comparing the profiles of HFD and VFD reveals that they are in near balance at almost all levels. The total flux term (TFD) (depicted by the dotted line in Fig. 5.16) is merely the summation of the HFD and VFD terms. TFD is negative in both the lower and upper levels and positive in the middle levels, therefore revealing a net loss of kinetic energy at lower and upper levels

0653 LST 25 June 1987 Ht = 6.75 km dx = 1.0 km

VFD

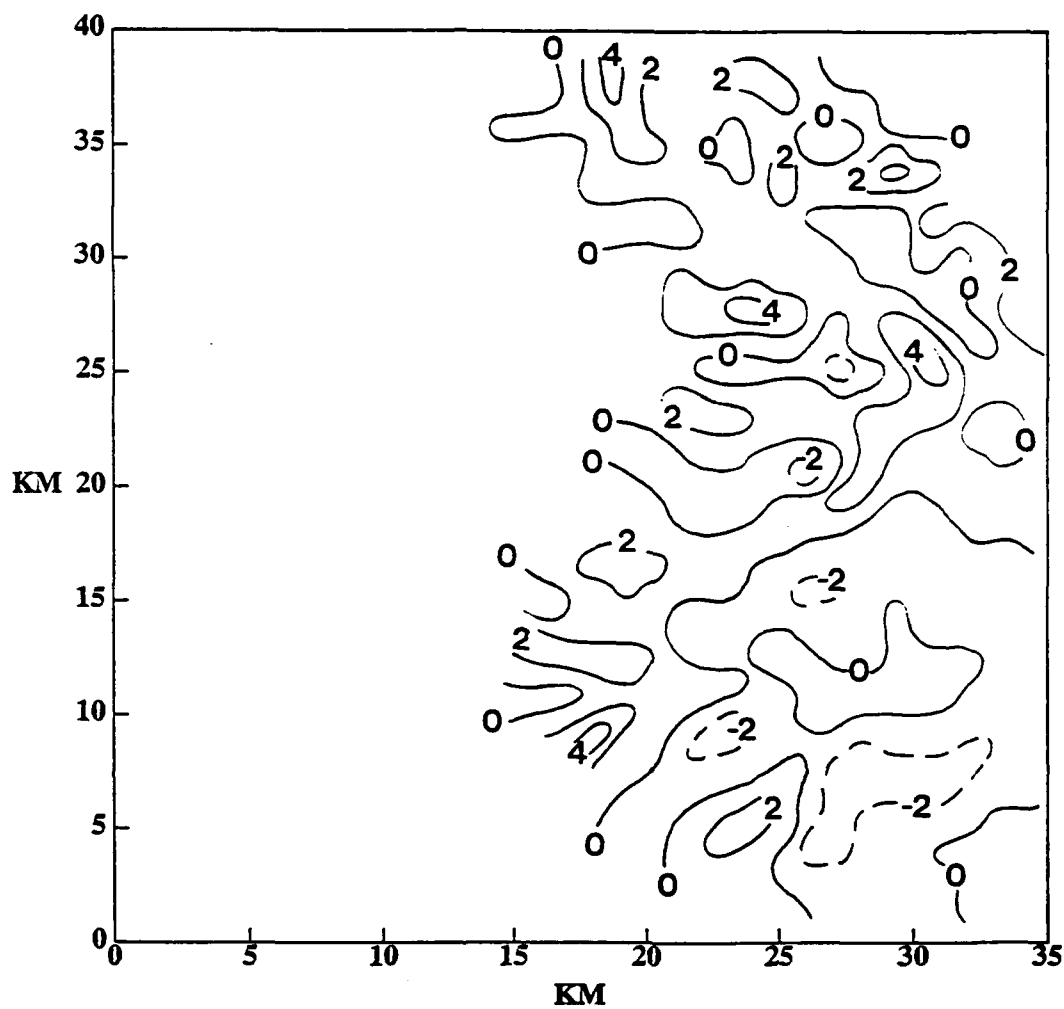


Fig. 5.14 Same as in Fig. 5.4 except for 6.75 km.

0653 LST 25 June 1987 Ht = 6.75 km dx = 1.0 km

BUO

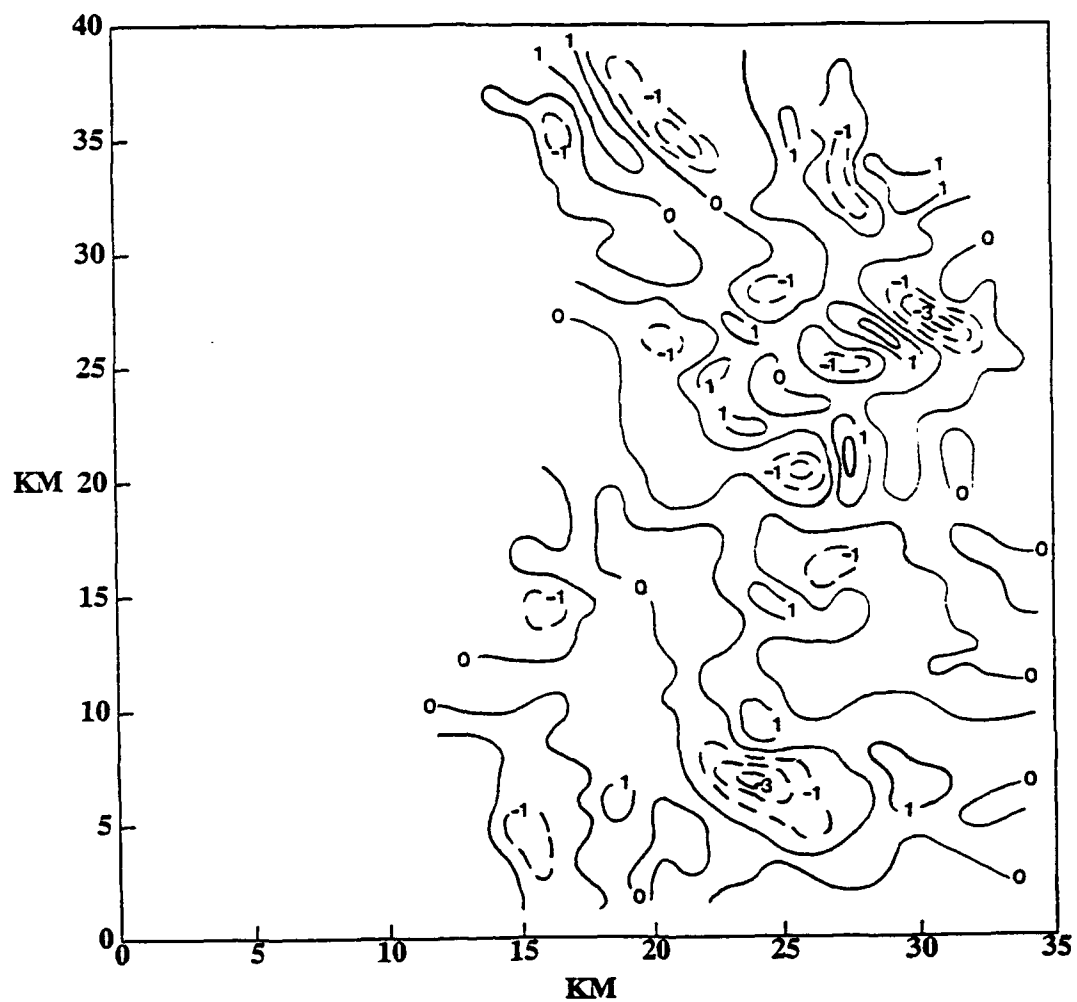


Fig. 5.15 Same as in Fig. 5.5 except for 6.75 km.

TAMEX IOP-13

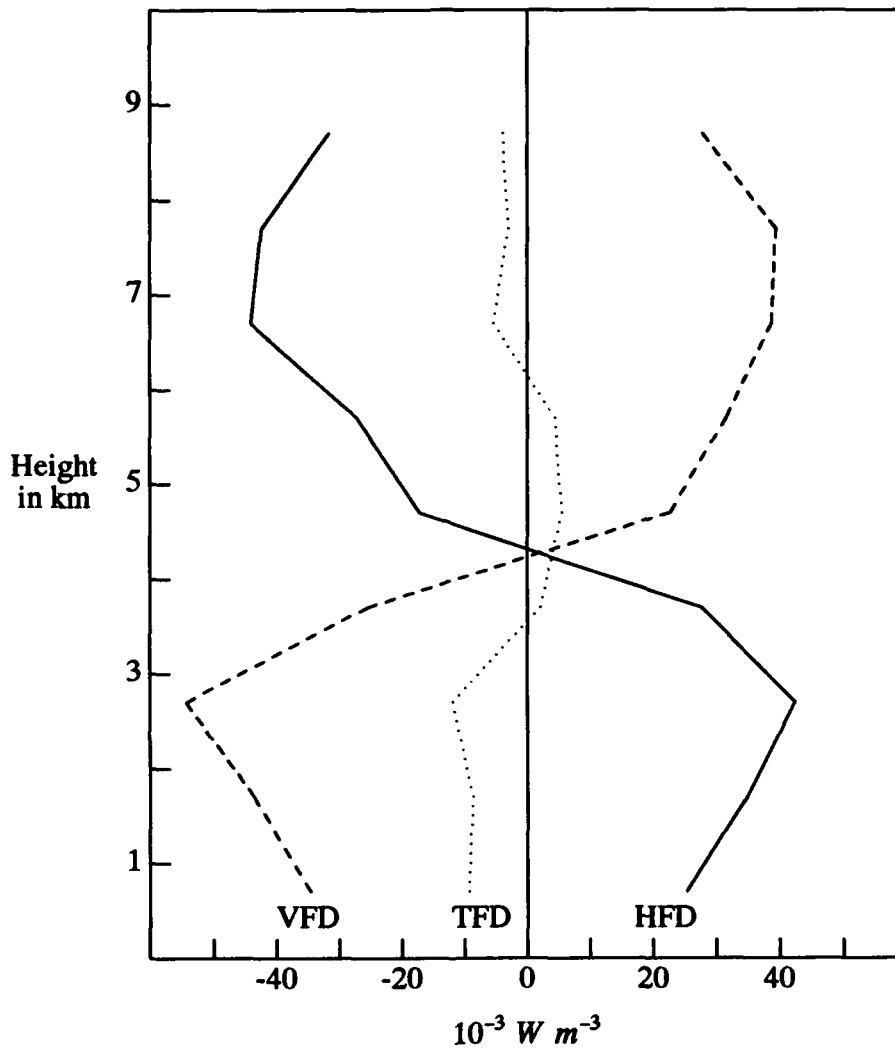


Fig. 5.16 Vertical profiles of terms HFD, VFD and TFD (as in 4.18), averaged over the domain of interest, based upon 0653 and 0700 LST 25 June 1987 data sets. Units are in $10^{-3} W m^{-3}$.

and a gain of kinetic energy in the middle layer (3.5 to 6 km). Figure 5.17 adds credence to the preceding statement. It depicts the mean vertical transport of kinetic energy, $\langle \rho_o K_3 W \rangle$, associated with IOP-13. The organized convection within IOP-13's rainband lends to a predominantly positive transport from the surface to 8.5 km with the maximum (157 W m^{-2}) occurring within the 3-4 km layer. Frontal lifting in the boundary layer combined with positive buoyancy aloft are the mechanisms responsible for this upward transport of kinetic energy within the domain of interest. The largest transport occurred in the layer where the strongest convective updrafts were located.

Vertical variations of the vertical generation term (VGE) and the total buoyancy production term (BUP) are illustrated in Fig. 5.18. Also displayed in Fig. 5.18 is the previously discussed TFD. Note that the scale along the x-axis is less than that in Fig. 5.16. In comparison to HFD and VFD, both VGE and BUP are smaller in magnitude. The VGE term is a sink of kinetic energy (negative value) below 5.25 km and a source (positive value) above 5.25 km. This term is well balanced by the BUP term at most levels. This finding is consistent with those reported in Lin and Coover (1988) and Lin *et al.* (1991). The BUP term is comprised of two processes, thermal buoyancy (BUO) and precipitation loading. Precipitation was found to be a small negative contribution to the total buoyancy production of kinetic energy thus BUP is primarily dependent upon the contribution of thermal buoyancy. Notice that the values of BUP are positive below 5.25 km and negative above 5.25 km. This was evident in

TAMEX IOP-13

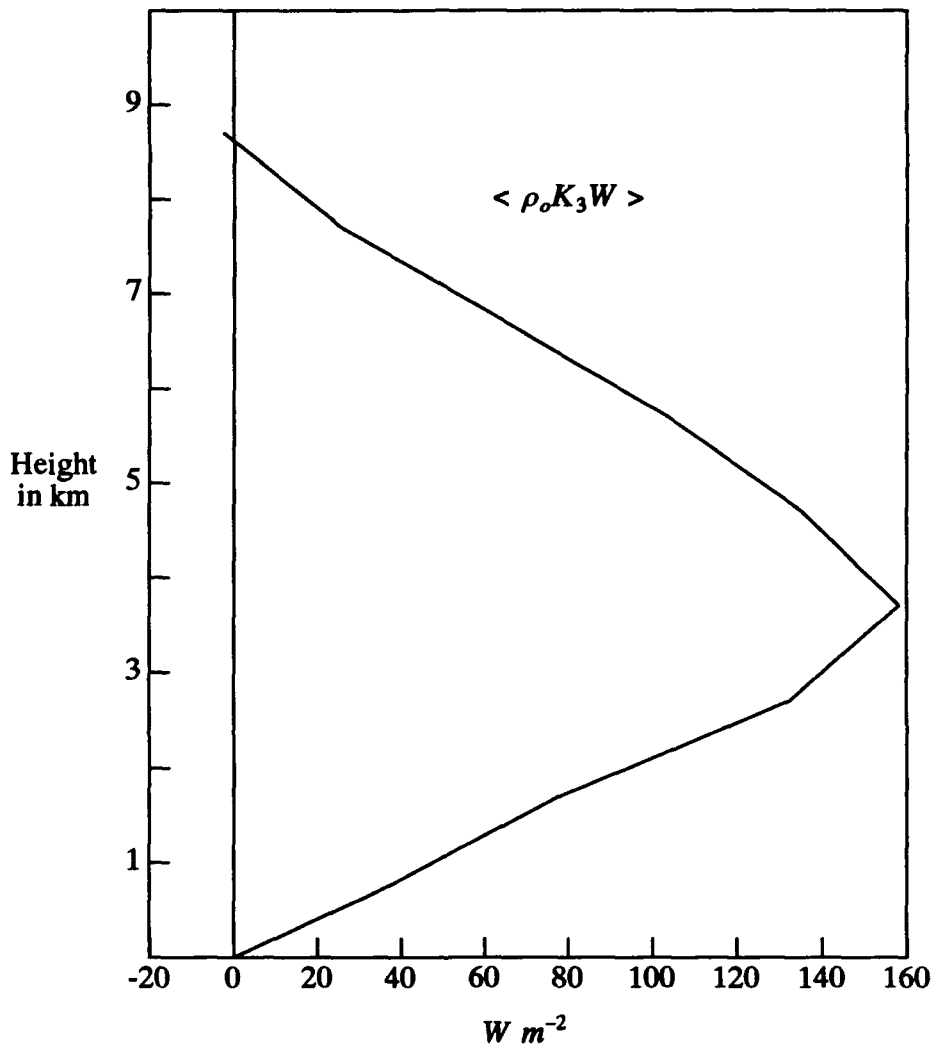


Fig. 5.17 The vertical distribution of mean vertical kinetic energy transport $\langle \rho_o K_3 W \rangle$. Units are in $W m^{-2}$.

TAMEX IOP-13

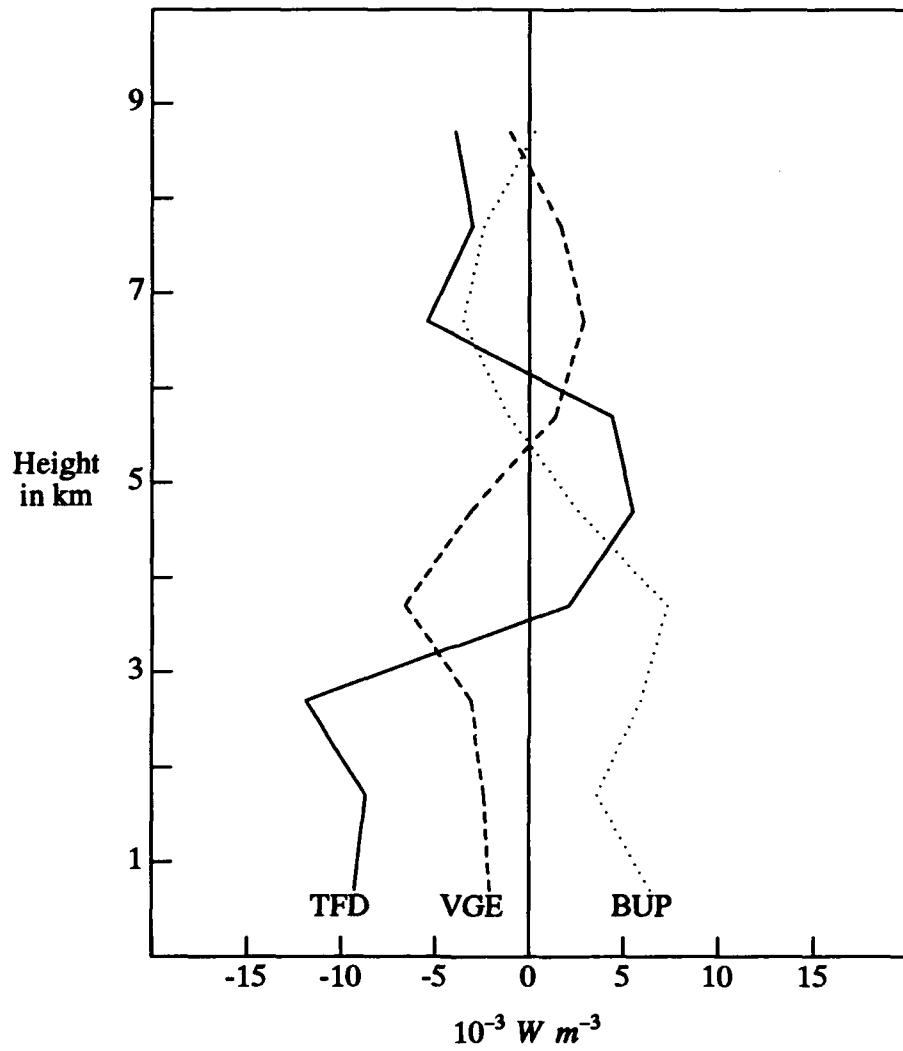


Fig. 5.18 Same as in Fig. 5.16 except for terms VGE, BUP and TFD.

the horizontal depictions of BUO in the previous section. In the layers below 5.25 km, air ascends in the convective updrafts causing warming due to release of latent heat by condensation. This results in an overall increase of kinetic energy due to BUP in those layers. Likewise, cooler air is descending within the convective downdrafts due to evaporative cooling thus also contributing to an increase in kinetic energy due to BUP. In contrast, above 5.25 km both the BUO and precipitation loading portions work together causing BUP to be negative thus a sink of kinetic energy. However, values of BUP above 7 km become less reliable due to the higher uncertainty in the retrieved perturbation temperature fields at upper levels (Lin *et al.*, 1991).

Vertical profiles for horizontal generation of kinetic energy (HGE) and frictional dissipation of kinetic energy (FDI) are shown in Fig. 5.19. These two terms are also smaller in magnitude than HFD and VFD but are of similar magnitudes when compared to VGE and BUP. The HGE term provides a source of kinetic energy at levels below 5.5 km and is variable and weak in levels above 5.5 km. The positive contribution of HGE occurs when the wind blows from high pressure to low pressure in the horizontal direction. Lin *et al.* (1993) found that in low and middle levels for IOP-13, horizontal perturbation pressure gradients were strong in the direction from west-northwest to east-southeast (parallel to the environmental flow). They also found that in the upper levels, the strong perturbation pressure gradients were in the direction opposite to the environmental flow. Thus, the results of the sign of the HGE

TAMEX IOP-13

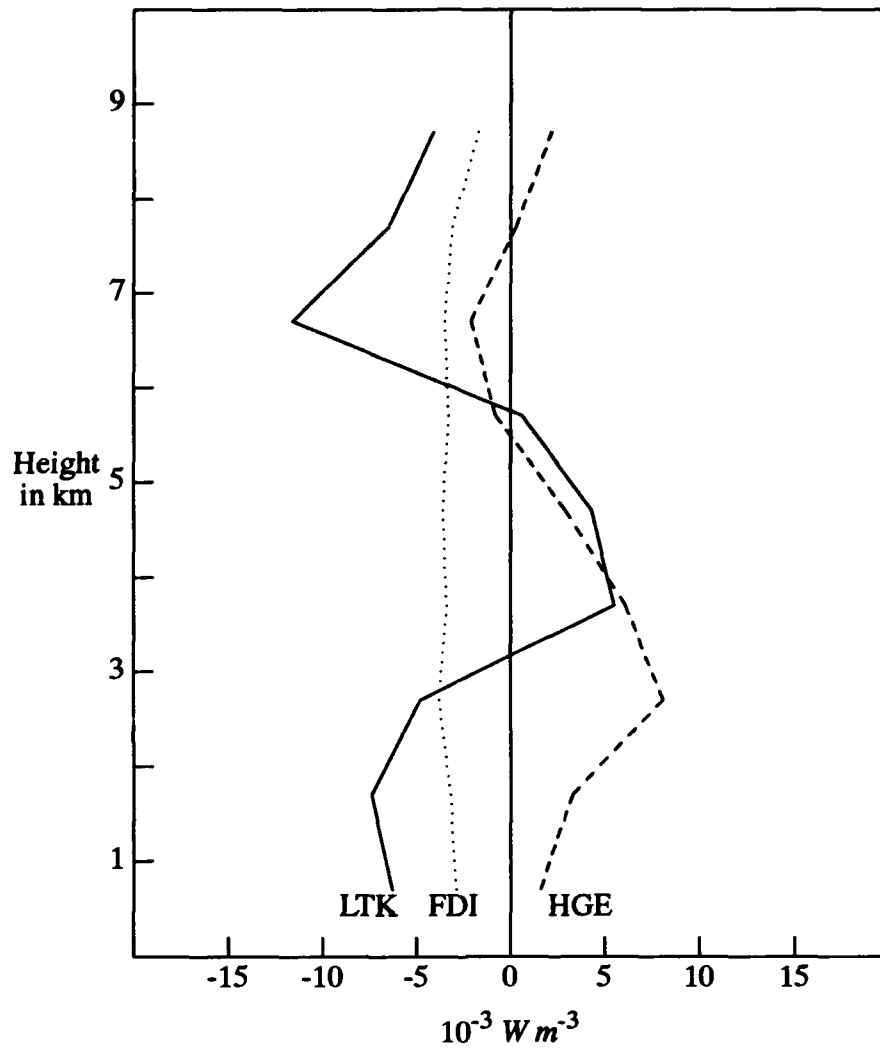


Fig. 5.19 Same as in Fig. 5.16 except for terms HGE, FDI and LTK.

term are consistent with the perturbation pressure fields found in Lin *et al.* (1993). The FDI term in this study was calculated using Austausch hypothesis with constant exchange coefficients and the three-dimensional dual-Doppler winds. This approach is significantly different from Lin and Coover (1988) and Lin *et al.* (1991) which both used the parameterization scheme of Klemp and Wilhemson (1978). It is also different from methods used by Fuelberg and Printy (1984) whom calculated dissipation as a residual term. The FDI term was found to be a sink at all levels and even though the values were relatively weak (consistently near $-3 \times 10^{-3} \text{ W m}^{-3}$), the vertical totals will later show that it is a primary sink of kinetic energy for this case.

Also displayed in Fig. 5.19 is the local tendency of kinetic energy (LTK) (the left-hand side of 4.18). Interpretation of this term should be strictly of qualitative nature and in a cautious manner since it is computed as a residual of all the other terms in (4.18). Theoretically, this term should equal the sum of the net gain/loss inside the selected mesoscale domain and the net flux through the domain boundaries. Unfortunately, this term includes errors in the data sampling as well as numerical computational errors thus a purely qualitative approach to its interpretation is best (Lin *et al.*, 1991). Looking at Fig. 5.19, note that the positive values of LTK are within the layer from 3-6 km with negative values above and below. Therefore, qualitatively there is an increase of kinetic energy within the middle levels. It is interesting to note that the vertical profiles of LTK in Fig. 5.19 and TFD in Fig. 5.18 are almost mirror images

displaying that the two most dominating terms in this budget study were HFD and VFD.

5.1.3 Vertical Totals of Kinetic Energy

Table 3 numerifies the vertical profiles presented in the previous section by integrating each term over a depth of 1 km from the surface to 9 km. The vertical totals of each term are listed at the bottom of the table and these totals offer an overall assessment of each specific process in the budget. A positive value represents an overall source of kinetic energy and a negative value implies an overall sink of kinetic energy. The values of the FDI term are an order of magnitude smaller than the HFD and VFD on a level-by-level basis but the vertical totals (-28.5 W m^{-2}) indicate that frictional dissipation was a significant sink of kinetic energy in the investigated prefrontal convective rainband. This result is in agreement of several previous studies (see Fuelberg and Printy (1984), Lin and Coover (1988) and Lin *et al.* (1991)). The two flux terms (HFD and VFD) are in quasi-balance within most layers, however, vertical totals of these two terms indicate that HFD (-32.4 W m^{-2}) is a main sink of kinetic energy while VFD (2.2 W m^{-2}) is a weak source. The vertical totals of VFD indicates that the mass continuity law is not violated within this domain of interest.

The vertical totals of BUP (19.1 W m^{-2}) indicate that it acts as an overall source of kinetic energy, while VGE (-12.3 W m^{-2}) acts as a sink. Recall that

these two terms were in quasi-balance through the system. Another source of kinetic energy is the HGE term (21.6 W m^{-2}). This indicates that the system had strong perturbation pressure gradients oriented in a manner that would be conducive to a positive contribution to kinetic energy. Further inspection of Table 3 reveals that the vertical sum of the LTK term indicates an overall decrease of total kinetic energy within the prefrontal convective rainband at the times of analysis.

The magnitudes and vertical totals of each term should be evaluated on a qualitative basis when comparing to other kinetic energy studies. No direct comparison of numerical values should be attempted since each study employs its own methodology and the weather systems under study may have several differences in structural and dynamical features. As an example, a fast-moving system like that of TAMEX IOP-2 (see Lin *et al.* 1991) will tend to have smaller values for the terms than those this case where the subtropical system moved very slowly. Also, using system-relative winds for the calculations can cause significant differences in magnitudes. The key is to look at trends.

5.2 Momentum-flux Budget

Since the orientation of the prefrontal convective rainband under investigation was primarily WSW-ENE, a rotation of -45 degrees to the domain of interest was necessary in order to determine the momentum-flux budget. This allows for the x-axis to be normal to the rainband (in this case, towards the

Table 3

Total kinetic energy budgets, averaged over a 25 by 40 km² horizontal domain and integrated over a depth of 1 km, based upon 0653 and 0700 LST 25 June data sets. Units are in W m⁻².

Layer (km)	HFD	VFD	TFD	HGE	VGE	BUP	FDI	LTK
8-9	-31.7	27.8	-3.9	2.2	-1.0	0.3	-1.7	-4.1
7-8	-42.4	39.4	-3.0	0.3	1.7	-2.4	-3.1	-6.5
6-7	-44.1	38.7	-5.4	-2.1	2.9	-3.5	-3.5	-11.6
5-6	-27.2	31.6	4.4	-0.8	1.4	-1.1	-3.3	0.6
4-5	-17.2	22.7	5.5	2.9	-3.1	2.6	-3.6	4.3
3-4	27.6	-25.5	2.1	6.1	-6.6	7.3	-3.4	-4.8
2-3	42.4	-54.3	-11.9	8.1	-3.1	5.9	-3.8	-4.8
1-2	34.9	-43.6	-8.7	3.3	-2.4	3.6	-3.2	-7.4
sfc-1	25.3	-34.6	-9.3	1.6	-2.1	6.4	-2.9	-6.3
Vertical total	-32.4	2.2	-30.2	21.6	-12.3	19.1	-28.5	-30.3

southeast) and the y-axis parallel to the rainband (towards the northeast) which is essential for a viable momentum-flux budget calculation. This technique is similar to the method used by LeMone (1983) in her study of a line of cumulonimbus observed during GATE in 1974. This section discusses the three-dimensional mean wind profiles, the horizontal momentum fluxes due to eddies, and the momentum-flux budget calculation regarding IOP-13.

5.2.1 Momentum Fluxes

The three-dimensional mean winds, U , V , and W , were determined for both the 0653 and 0700 LST volume scans within the rotated domain of interest and were averaged between the two volumes in order to determine the "best-estimate" profiles for each component. Figure 5.20 shows that the values of U are positive (i.e., towards the southeast) throughout the entire storm system with a maximum value of 14.25 m s^{-1} near the 8 km height. On the other hand, V is positive (towards the northeast) up to the height of 8.25 km with its maximum positive value (13.15 m s^{-1}) near 4 km. This strong low-level mean v-component wind is indicative of the low-level jet caused by the SW monsoon flow. Thus, the horizontal mean winds (U, V) are primarily southwesterly at low levels, westerly in the middle levels and northwesterly in the upper levels. Examination of W shows that weak upward vertical motion dominated this system with a maximum mean vertical velocity of 1.1 m s^{-1} near 5 km.

TAMEX IOP-13

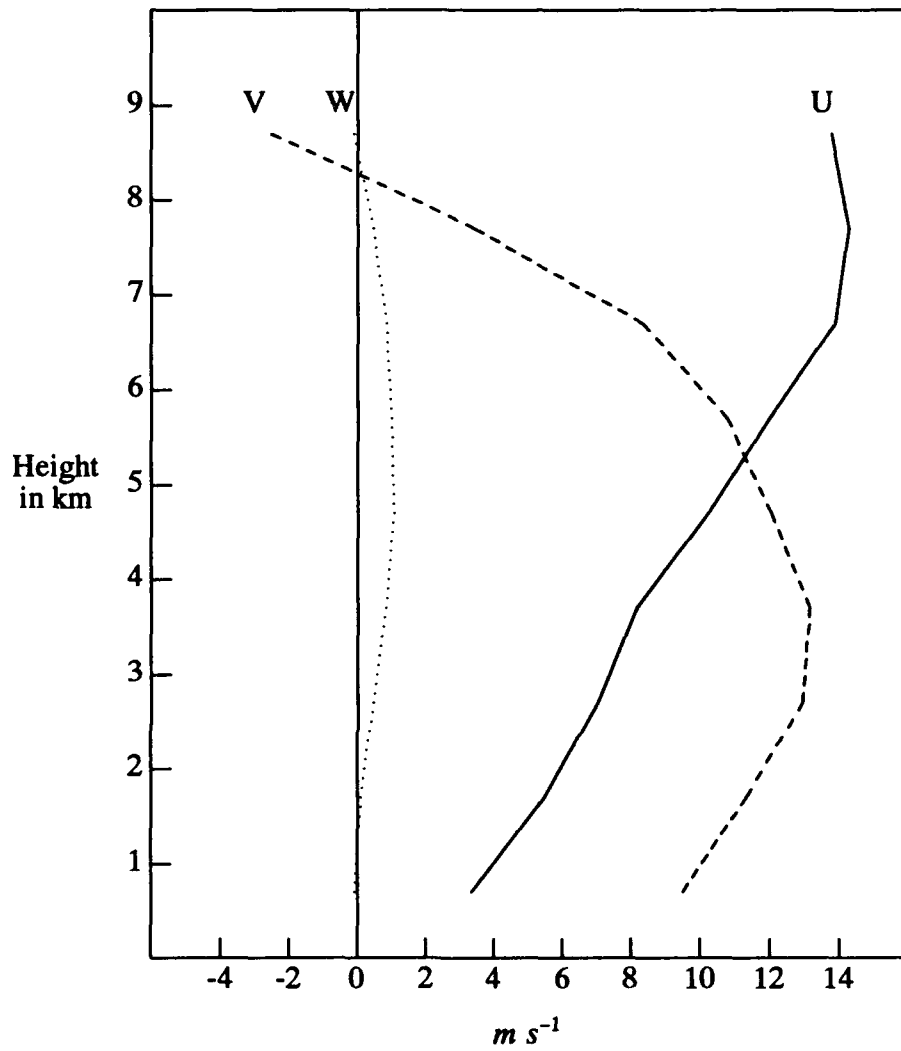


Fig. 5.20 Vertical profiles of the three mean wind components, U, V and W, averaged over the rotated domain of interest, based upon 0653 and 0700 LST 25 June 1987 data sets. Units are in $m s^{-1}$.

From the values of U and V , the vertical shear of the mean wind can be determined for both horizontal components. Again utilizing Fig. 5.20, one can easily visualize the trends of the vertical shear for both components, which will aid in the discussion of momentum flux later in this section. For the u -component, positive vertical shear ($\partial U/\partial z > 0$) occurs at all levels below 7 km. Numerically, the strongest positive shear is approximately $1.8 \times 10^{-3} \text{ s}^{-1}$ at levels from the sfc-2 km and from 4-7 km. Weak negative vertical shear of U (-0.25 to $-0.50 \times 10^{-3} \text{ s}^{-1}$) occurs above 7 km. The v -component exhibits an entirely different profile. Strong positive vertical shear ($\partial V/\partial z \sim 1.8 \times 10^{-3} \text{ s}^{-1}$) occurs in the lowest layers (sfc-3 km) but then dramatically turns negative above 3 km, especially above 6 km where values exceed $-6.0 \times 10^{-3} \text{ s}^{-1}$.

For simplicity, it has often been assumed that the vertical transport of horizontal momentum in the atmosphere is in the same sense as if air parcels were molecules - "down" the vertical gradient. That is, for wind increasing with height (positive vertical shear), downward-moving parcels carry with them high momentum and upward-moving parcels carry low momentum (LeMone *et al.*, 1984). In mathematical form, the transport of a quantity s , e.g., u or v , using the "mixing-length" approach is given by:

$$\overline{w's'} = -K \frac{\partial \bar{s}}{\partial z} \quad (5.1)$$

where K , the exchange coefficient, is positive, w is the vertical component of

the wind, s is the quantity of interest and the overbar and primes represent means and deviations from the means, respectively. Using (5.1), the eddy momentum flux for the u - and v -components can be determined. For downgradient (countergradient) transport of horizontal momentum by eddies, K is positive (negative).

The vertical transport of horizontal momentum occurring in a deep convective system is important to analyze since it shows how the system may affect the large-scale dynamics (LaFore *et al.*, 1988). Figures 5.21 and 5.22 display profiles of the u -momentum and v -momentum fluxes, averaged over the two volumes within the rotated domain of interest. The solid line represents total transport, the dashed line represents the mean transport and the dotted line represents the eddy transport. In this study, I will focus on the eddy transports of horizontal momentum. Positive (negative) values of the fluxes, $(\overline{u'w'})$ and $(\overline{v'w'})$, represent an upward (downward) transport of the specified horizontal component of momentum.

Looking at Fig. 5.21, $\overline{\rho u'w'}$, the u -component of the vertical transport of horizontal momentum due to eddies, is positive at all levels with a maximum value of $3 \text{ kg m}^{-1} \text{ s}^{-2}$ near 3.75 km. This positive $\overline{\rho u'w'}$ throughout all levels is likely due to the overall positive vertical motions coupled with the transport of positive horizontal momentum ($u' > 0$) into the southeastward-tilting updrafts. Figure 5.23 displays a vertical cross-section along line A-B in Fig. 5.1 for the fields of (a) the system-relative winds (with reflectivity Z contours

TAMEX IOP-13

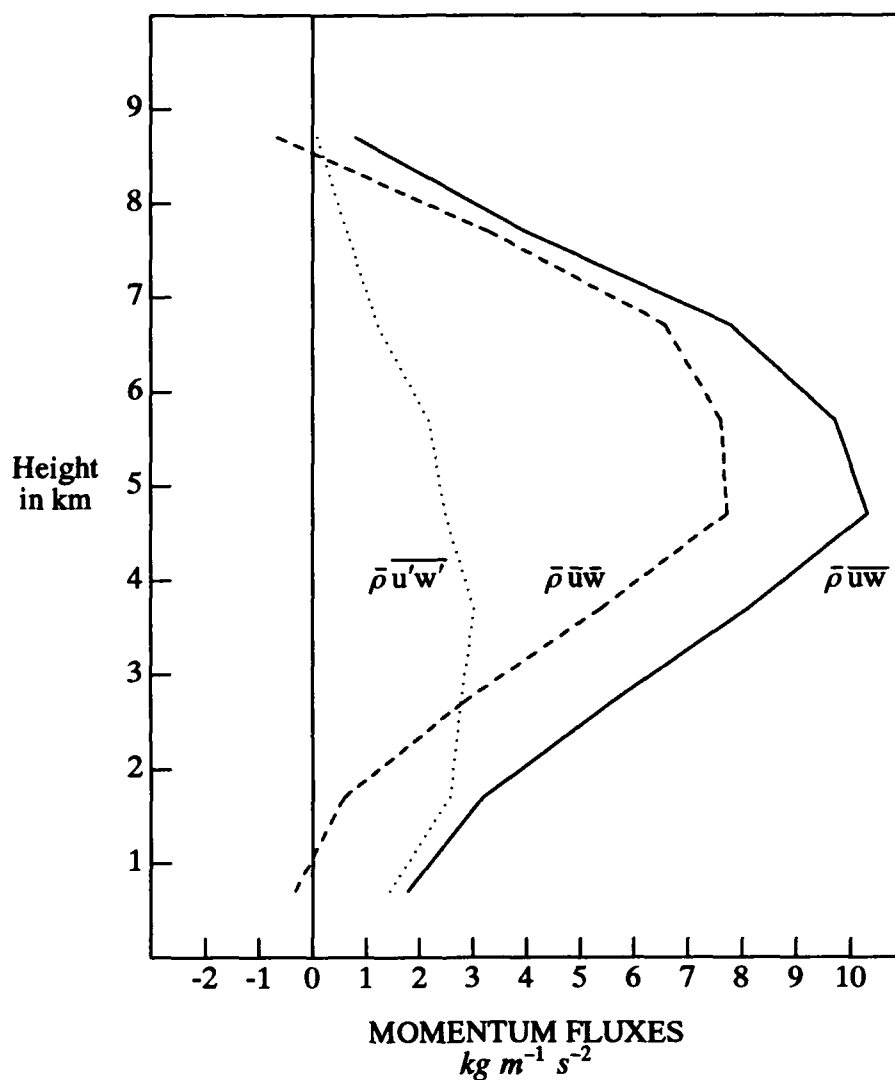


Fig. 5.21 Vertical profiles of the vertical transports of horizontal momentum for the u-component, averaged over the domain of interest, based upon 0653 and 0700 LST 25 June 1987 data sets. The total, mean and eddy transports are denoted by the solid, dashed and dotted lines, respectively. Units are in $kg\ m^{-1}\ s^{-2}$. A positive value represents an upward transport of horizontal momentum.

superimposed) and (b) the vertical velocity, w . These cross-sections are oriented NW-SE and represent a typical cross-sectional view of the prefrontal convective rainband under investigation. The heavy dashed line represents the Mei-Yu front (~ 20 km from the origin) and the arrow along the x-axis signifies the position of the gust front (GF). In Fig. 5.23 (b), the southeastward-tilt of the main updraft (near 21 km) is highly evident. These two cross-sections lend visual support that u' and w' tend to be of the same sign in the majority of the domain thus causing $\overline{\rho u' w'}$ to be positive.

The vertical transport of horizontal momentum due to eddies can be determined from (5.1) by comparing the signs of $\overline{w' s'}$ and $\partial \bar{s} / \partial z$. Recalling that $\partial U / \partial z$ is positive for all levels below 7 km and since $\overline{\rho u' w'} > 0$ for all levels, we find that the vertical transport of u-momentum due to eddies is countergradient below 7 km. This is contrary to "mixing-length" theory. This finding was also found during the study of a tropical convective line during GATE (LeMone, 1983) and in the study of an eastern Arabian Sea convective band (Rao and Hor, 1991) but not over such a deep layer as was found in this case.

The vertical transports of v-momentum by total, mean and eddy motions in the direction parallel to the prefrontal convective rainband are depicted in Fig. 5.22. In contrast to u-momentum due to eddies, the values of $\overline{\rho v' w'}$ are negative at levels below 6.75 km. However, comparing this profile to the vertical shear of V , we find that $\overline{\rho v' w'}$ and $\partial V / \partial z$ are the same sign only in the layer between 4-6.5 km. Thus countergradient transport is also occurring

TAMEX IOP-13

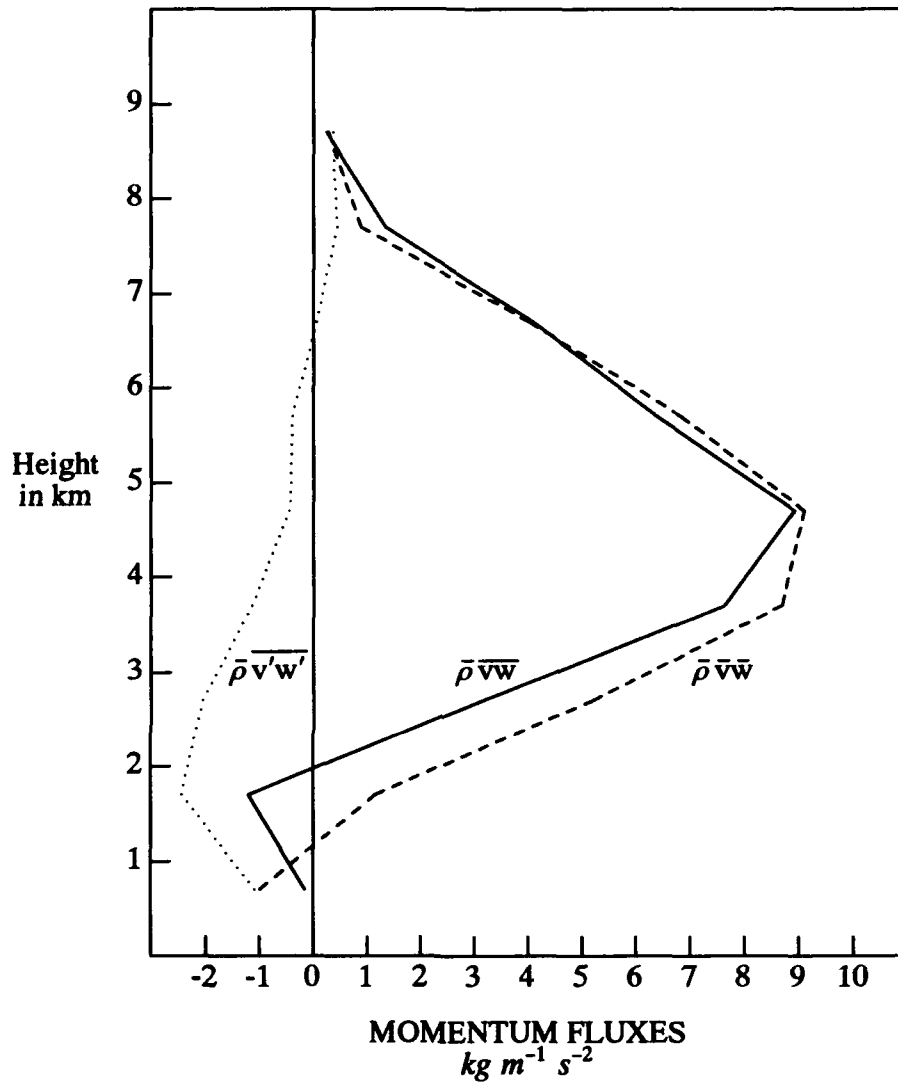


Fig. 5.22 Same as in Fig. 5.21 except for the v-component.

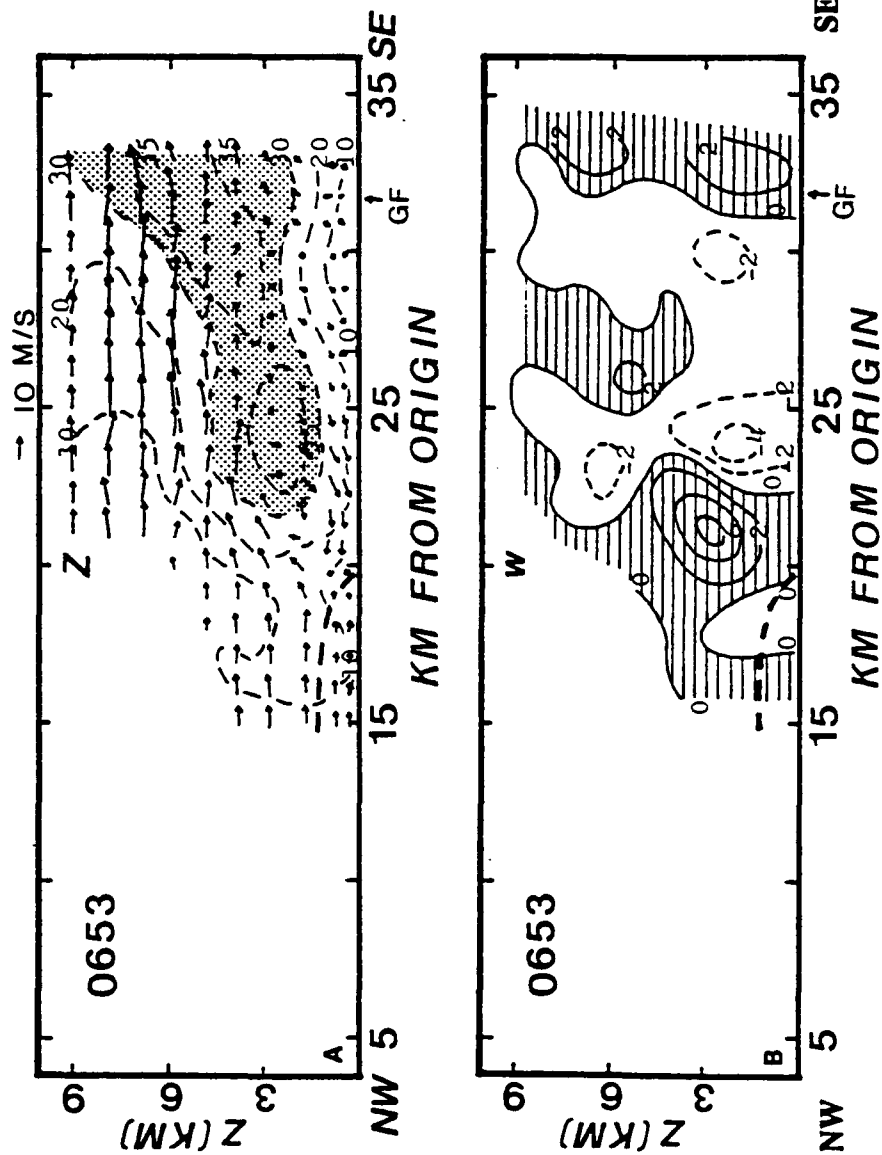


Fig. 5.23 The vertical cross-section along the line A-B in Fig. 5.1 showing (a) system-relative wind with reflectivity contours Z superimposed and (b) vertical velocity, w. Positive values are hatched and negative values dashed. Vertical velocity contours are at 2 $m s^{-1}$ intervals. Reflectivities greater than 30 dBZ are shaded (after Lin *et al.*, 1993).

within this layer. But below 4 km and above 6.5 km, the two terms are opposite in sign thus adhering to "mixing-length" theory by exhibiting a downgradient transport of v-momentum by eddies.

5.2.2 Momentum-flux Budget Analysis

The horizontal momentum-flux budgets are analyzed in this section. The generation of u- and v-momentum flux within the domain of interest were calculated from (4.21) and (4.23), respectively, and a "best-estimate" based on the 0653 and 0700 LST 25 June volume scans are presented in Tables 4 and 5 for the Terms A-G. On the meso- β -scale, the Coriolis term (Term H) is generally much smaller than the other terms thus not presented in either table. Keep in mind that the local time-change of u- and v-momentum flux (the left-hand sides of 4.21 and 4.23) is determined from the summation of all the right-hand side of the respective equation and is subject to numerous errors, similar to those discussed in the local term (LTK) of the total kinetic energy equation (4.18). Thus, this term must be interpreted on a qualitative basis. However, theoretically, a positive (negative) rate of change in $\overline{u'w'}$ or $\overline{v'w'}$ will decrease (increase) downward transport of momentum due to eddies (Lin and Condray, 1988).

Results of the $\overline{u'w'}$ budget is shown in Table 4. Contributions from the shear production (S), total buoyancy (B) and velocity-pressure interaction (P) to the local time-change of $\overline{u'w'}$ are more dominant than the remaining terms

Table 4

Results of the u-momentum flux ($\overline{u'w'}$) budget calculation, averaged over the 25 by 40 km² horizontal domain, based upon 0653 and 0700 LST 25 June data sets. Units are in 10⁻³ m² s⁻³.

Z (km)	$\frac{\partial \overline{u'w'}}{\partial t}$	Term A S	Term B T _r	Term C B	Term D P	Term E D _x	Term F D _y	Term G D _z
0.75	8.15	-3.49	3.62	24.22	-16.57	0.49	0.02	-0.14
1.75	7.22	-6.81	1.38	17.52	-3.68	0.04	-0.52	-0.71
2.75	0.67	-7.61	-1.21	11.51	0.52	-1.71	0.35	-1.18
3.75	-16.08	-10.34	-0.70	5.08	-8.46	-1.63	0.95	-0.98
4.75	-22.54	-13.94	-2.47	7.73	-10.61	-2.45	-0.71	-0.09
5.75	-25.57	-13.27	-2.77	1.70	-9.30	-2.37	-0.71	1.15
6.75	-11.27	-7.41	-0.48	6.74	-9.04	-2.04	-0.73	1.69
7.75	0.74	0.26	0.56	-6.49	8.39	-2.43	-0.65	1.10
8.75	2.81	1.14	0.46	-10.73	13.25	-1.87	-0.42	0.71

in (4.21). Fig. 5.24 illustrates vertical profiles of these three terms. The pressure term (P) (dashed line) and buoyancy (B) (solid line) term are more dominant than the shear term (S) (dashed line separated by deltas) in the lower and upper levels. The P term and B term tend to be of opposite signs and are in quasi-balance throughout the depth of the system. The buoyancy term provided a positive u-momentum flux below 7 km following the sign of $\overline{u'w'}$. A positive contribution of the B term is largely due to the advection of warm air ($T'_v > 0$) toward the southeast ($u' > 0$) and cold air ($T'_v < 0$) toward the northwest ($u' < 0$) and vice versa. As depicted in Lin *et al.* (1993), warm air was consistently advected towards the northeast at low levels ($Z < 3$ km) in the warm sector, while warmer air was transported southeastward in the midtroposphere. These processes as a whole contributed to the increase of an upward transport of horizontal momentum (i.e., $\partial \overline{u'w'}/\partial t > 0$). This feature is different from those reported in tropical and subtropical studies cited earlier. The shear term (S) is comparable to P and B terms in the middle levels where there is strong positive vertical shear of the mean u-component of the wind. The dotted line in Fig 5.24 is the vertical profile of the sum of these three dominant terms (S+B+P). This profile is comparable to how the local time-change of u-momentum flux ($\partial \overline{u'w'}/\partial t$) varies with height. Note how the dominating negative values of S+B+P within the 4-6 km layer. This is also evident in Table 4 when looking at the values of $\partial \overline{u'w'}/\partial t$. The two dominating processes contributing to this negative value of the tendency term are the shear production (S) and velocity-pressure interaction (P) terms. This is consistent with the pre-

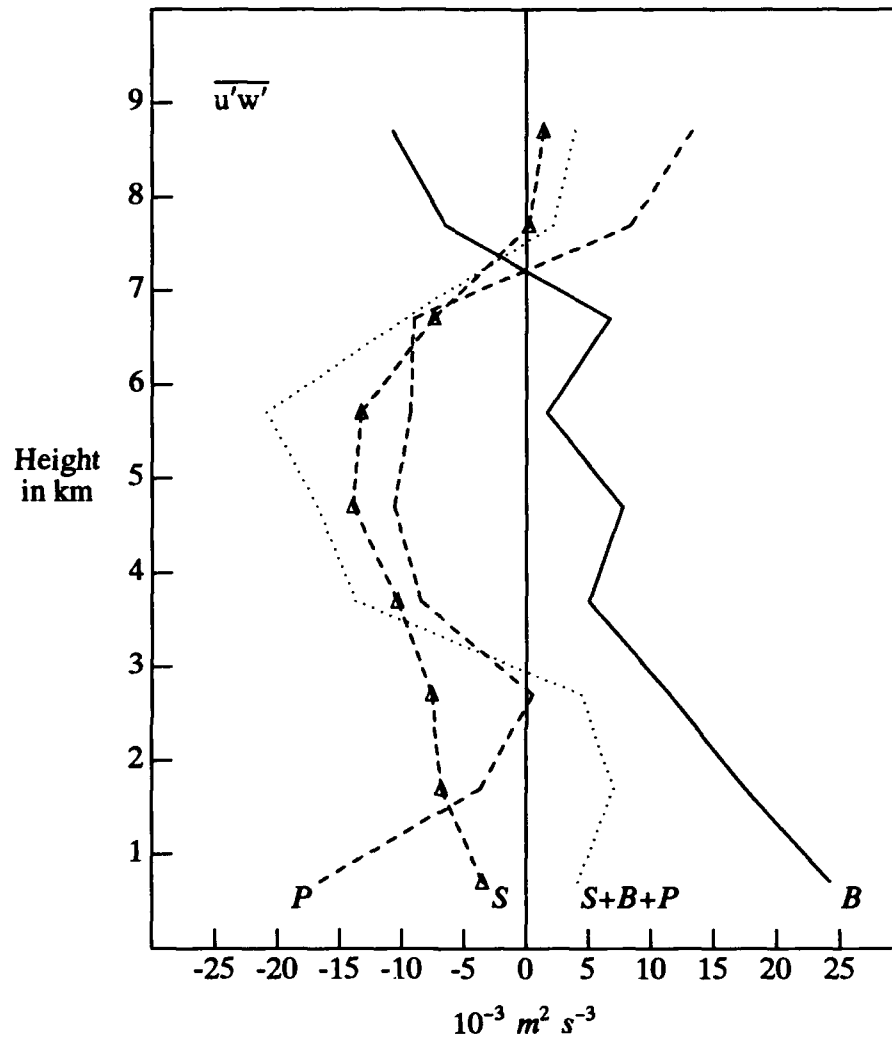


Fig. 5.24 Vertical profiles of the dominant terms in the momentum-flux budget for the u-component, $\overline{u'w'}$, averaged over the domain of interest, based upon 0653 and 0700 LST 25 June 1987 data sets. Symbols represent contributions from the vertical shear (S), total buoyancy (B), and velocity-pressure interaction (P), and SBP the sum of these terms (S+ B+P). Units are in $10^{-3} m^2 s^{-3}$.

viously discussed findings of the strong positive vertical shear. It is also consistent with the findings of strong perturbation pressure gradients in the direction of the mean environmental flow within the middle levels (Lin *et al.*, 1993). Initially, we find that $\overline{\rho u'w'}$ is positive. Hence, the negative rate of change of $\overline{u'w'}$ qualitatively implies that an upward flux of horizontal momentum is weakened in the middle troposphere due to the combined effects of the shear production (S) and velocity-pressure interaction (P) terms. However, in the lower troposphere ($Z < 3$ km), the buoyancy production term (B) largely contributes to the increase of upward momentum transport by eddies.

Table 5 summarizes the results of the v-momentum-flux budget of this study in a similar manner presented in Table 4. Again, the same three processes, terms A, C and D (representing shear production (S), total buoyancy (B) and velocity-pressure interaction (P), respectively) were found to be the most influential terms in contributing to the local time-change of $\overline{v'w'}$. Similar to the u-component finding, P and B terms were found to be in quasi-balance throughout the depth of the storm system. However, these terms were both opposite in sign to their u-momentum counterparts. Thus, P was a main source of $\overline{v'w'}$ generation and B was a sink (see Fig. 5.25). The buoyancy term (B) for the v-momentum flux below 7 km also followed the sign of $\overline{v'w'}$. This term is negative throughout the lower 8 km due largely to the advection of colder air ($T'_v < 0$) towards the northeast ($v' > 0$) and warmer air ($T'_v > 0$) towards the southwest ($v' < 0$). Thus, both component buoyancy production terms acted in

conjunction with the sign of their respective flux components. This trend was also found in the study of a subtropical squall line during TAMEX IOP-2 (Lin *et al.*, 1991). Inspection of the shear production term (S) in Fig. 5.25 (dashed line separated by deltas) shows that it became an overwhelming source of positive v-momentum flux generation above 6 km. The strong negative vertical shear of the mean v-component wind (look back at Fig. 5.20 again) shows clear evidence to support this finding.

The vertical profile of S+B+P is represented by the dotted line in Fig. 5.25. Again, this profile exhibits a close association to how $\overline{\partial v'w'}/\partial t$ varies with height. The stronger positive values of $\overline{\partial v'w'}/\partial t$ from 4-8 km qualitatively implies an increase of the upward transport of v-momentum due to eddies thus possibly strengthening the earlier found countergradient transport in the 4-6.5 km layer below 6.5 km. Hence, a positive rate of change of $\overline{v'w'}$ ($\overline{\partial v'w'}/\partial t > 0$) qualitatively implies that the downward transport of horizontal momentum in the direction parallel to the rainband is decreased. Conversely, when $\overline{\partial v'w'}/\partial t$ is negative, like in the lower levels ($Z < 3$ km), the downward transport of horizontal momentum is increased. These findings are consistent with the observed features reported earlier. It was shown that the large-scale LLJ weakened and a MLJ formed as a result of organized convection associated with the prefrontal convective rainband, thus indicating that the mesoscale was providing feedback to the large-scale.

Table 5

Results of the v-momentum flux ($\overline{v' w'}$) budget calculation, averaged over the 25 by 40 km² horizontal domain, based upon 0653 and 0700 LST 25 June data sets. Units are in 10⁻³ m² s⁻³.

Z (km)	$\frac{\partial \overline{v' w'}}{\partial t}$	Term A S	Term B T _r	Term C B	Term D P	Term E D _x	Term F D _y	Term G D _z
0.75	-9.98	-2.83	-3.73	-9.37	10.18	-1.38	-2.99	0.14
1.75	-12.39	-6.37	-1.10	-6.52	2.45	-0.25	-1.22	0.53
2.75	-0.83	-5.12	1.54	-3.14	4.12	1.79	-0.45	0.43
3.75	3.97	3.01	-0.72	-6.32	6.58	2.49	-0.81	-0.26
4.75	8.20	8.61	-0.24	-2.06	3.68	1.01	-2.43	-0.37
5.75	11.00	13.17	2.34	-4.24	2.96	0.92	-3.79	-0.36
6.75	16.17	23.98	3.31	-11.79	2.65	0.83	-2.34	-0.47
7.75	9.56	20.09	1.40	-6.08	-1.99	-1.92	-1.96	0.02
8.75	3.99	14.12	-0.62	5.06	-11.10	-2.30	-1.55	0.38

TAMEX IOP-13

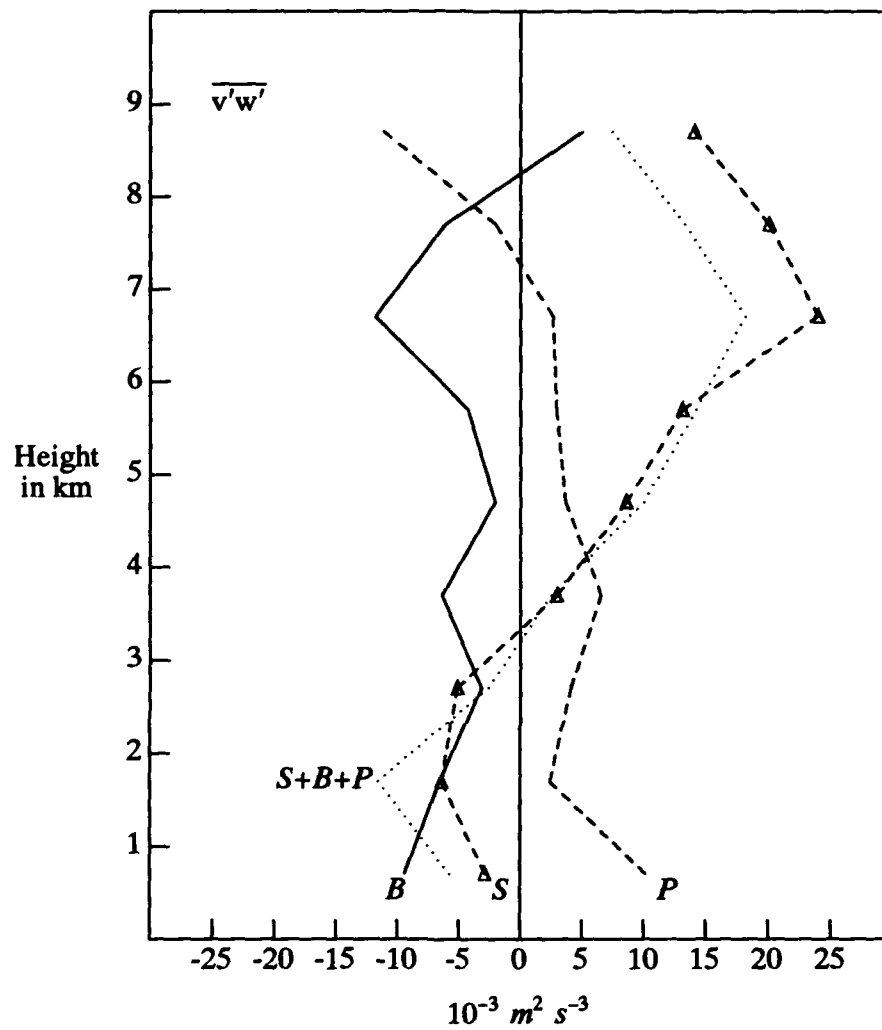


Fig. 5.25 Same as in Fig. 5.24 except for the v-component.

5.3 Vorticity Budgets

The budgets for the three components of vorticity (ξ , η and ζ) are presented in this section. A discussion of the three-dimensional vorticity fields at three levels (0.75 km, 3.75 km and 6.75 km) will be presented in order to look at the vorticity fields at low, middle and upper levels. Horizontal variations of the four dominant terms within each vorticity component equation will be displayed and discussed in order to aid in the discussion of their respective component budgets. Due to the vast number of diagrams for each level associated with the three component equations for the two volume scans, only a handful of pertinent diagrams will be presented in order to keep the volume to a level where it can give the general idea of the plan views of these processes.

5.3.1 Vorticity Fields

Plan views of the fields of the horizontal vorticity (in vector form) for 0700 LST 25 June 1987 at three levels are presented in Figs. 5.26, 5.28 and 5.30. These vectors represent $(\hat{i}\xi + \hat{j}\eta)$ at each grid point of the rotated horizontal domain. Except in the vicinity of strong updraft/downdraft cores where the horizontal variations of the vertical wind component, w , are highly significant, these horizontal vorticity vectors are essentially $(-\partial v/\partial z)\hat{i} + (\partial u/\partial z)\hat{j}$, which is the difference between the vertical shear of the two horizontal wind components. Thus, a large vector indicates that one of the vertical shear values is more dominant than the other at that grid point. The vertical velocity

contours (in 3 m s^{-1}) for the displayed level are superimposed on the horizontal vorticity vectors with negative values contour by the dashed lines. Figures 5.27, 5.29 and 5.31 show the horizontal distributions of the vertical component of vorticity, ζ , at the same three levels superimposed on the system-relative horizontal winds. On the lowest level diagrams, the heavy dashed line indicates position of the wind-shift line associated with the surface front and the dotted line indicates the position of the surface gust front. As a reminder, the x-axis is positive towards the southeast and the y-axis is positive towards the northeast in all diagrams.

At 0.75 km, the horizontal vorticity vectors (Fig. 5.26) are primarily north to northwest in direction. This is because ξ at this level (not shown) is primarily negative and weaker than η , which is generally positive since the vertical shear of the u-component winds is positive at low levels. The strongest vectors are to the southeast (ahead) of the wind-shift line in an area between the updraft and downdraft cores located in the northeastern portion of the domain. This is where the strongest cell was located thus strong shear is associated with it. Behind the wind-shift line, north to northwest directed vectors prevail while the vectors are primarily variable and weaker in the areas behind the gust front. Figure 5.27 depicts the horizontal variation of ζ superimposed on the system-relative horizontal winds at 0.75 km. Positive values of ζ dominate ahead of the wind-shift line with positive centers of 4.0 to $8.0 \times 10^{-3} \text{ s}^{-1}$ associated with the updraft cores. The positive values of ζ are located generally where the

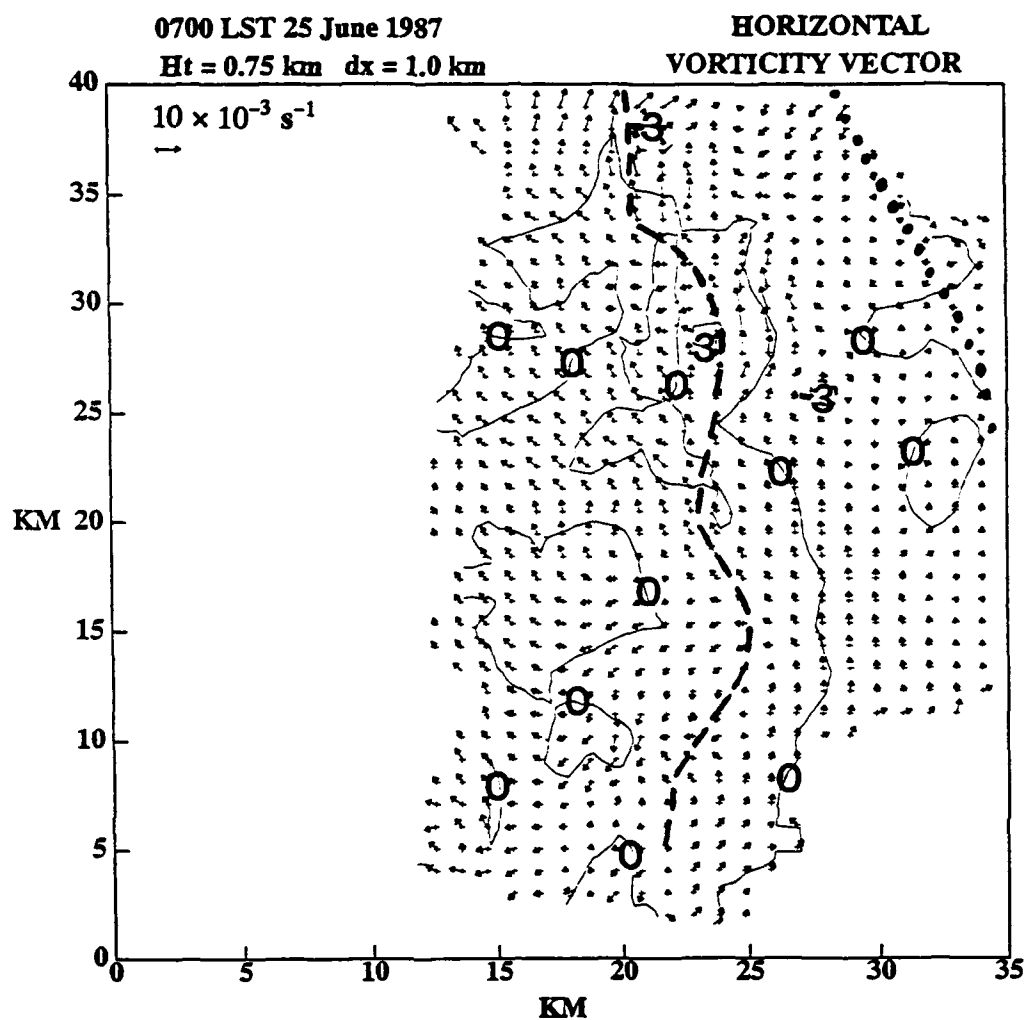


Fig. 5.26 Plan view of horizontal vorticities ($\hat{i}\xi + \hat{j}\eta$) with vertical velocity, w , contours superimposed at 0.75 km for 0700 LST 25 June 1987. Contour interval is $3 \times 10^{-3} \text{ s}^{-1}$ with negative values dashed. The vector representing $10 \times 10^{-3} \text{ s}^{-1}$ is located in the top left corner. Positions of the Mei-Yu front wind-shift line (heavy dashed line) and the gust front (dotted line) are also depicted.

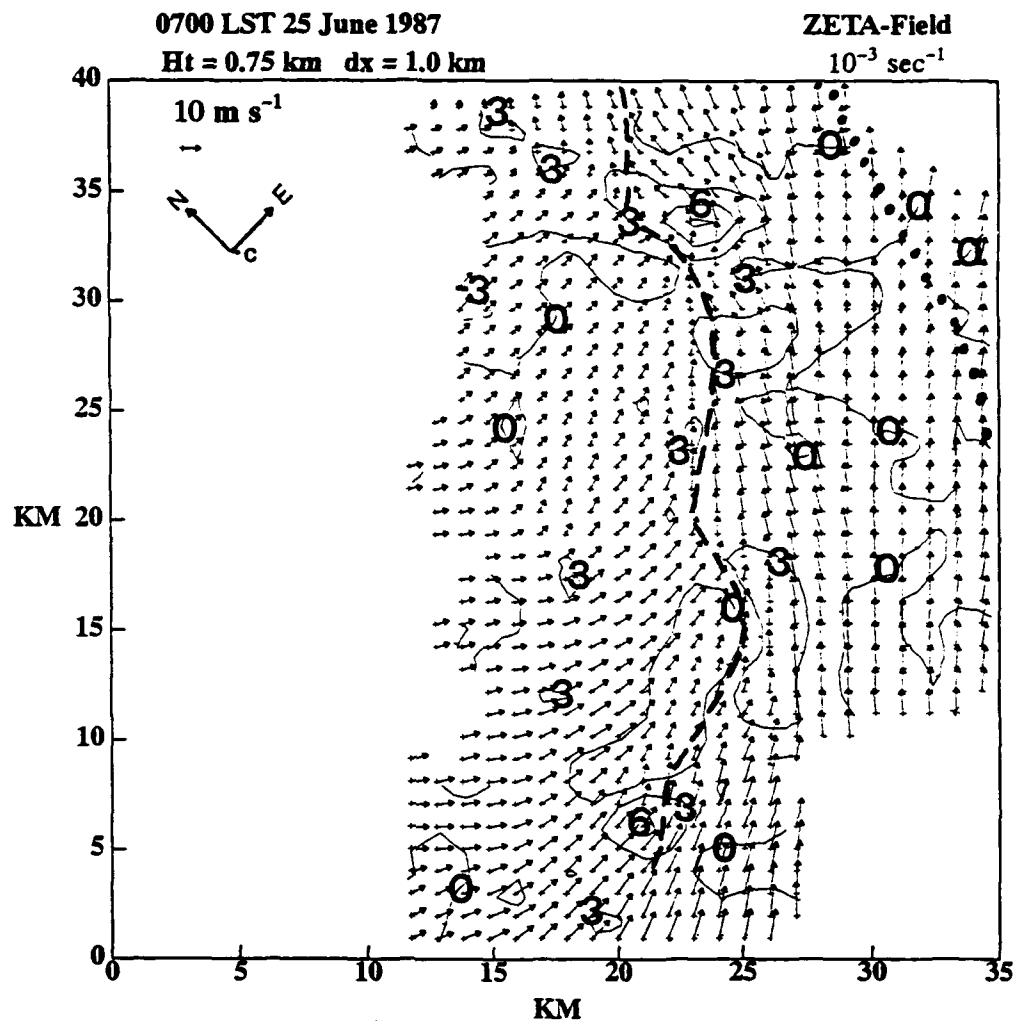


Fig. 5.27 Plan view of the vertical vorticity, ζ , field superimposed on the system-relative horizontal wind field at 0.75 km for 0700 LST 25 June 1987. Units for ζ are in 10^{-3} s^{-1} . Contour interval is $3 \times 10^{-3} \text{ s}^{-1}$ with negative values dashed. The system-relative wind speed for 10 m s^{-1} is denoted by the vector in the top left corner. North (N), east (E) and system motion (c) are indicated in the top left corner. Positions of the Mei-Yu front wind-shift line (heavy dashed line) and the gust front (dotted line) are also depicted.

horizontal vorticity vectors are north to northeast thus ζ and η are comparable at this level while ξ is slightly weaker. The environmental flow is advecting positive ζ towards the east/northeast, into the heart of the convective cells. The updraft cores are also transporting positive ζ upward into the main cells.

Figures 5.28 and 5.29 display the same fields as Figures 5.26 and 5.27 except at the 3.75 km level. The 3.75 km horizontal variations of ξ and η (not shown) indicate that η is overall positive with the same field strength as at the 0.75 km level but ξ changed from the weak negative values at 0.75 km to a series of positive/negative couplets located near the updraft/downdraft cores throughout the entire domain. Thus, the vectors displayed in Fig. 5.28 are highly variable in strength and direction. This level exhibits many horizontal cyclonic/anticyclonic centers (commonly called vortex rings in the horizontal) associated with the updraft and downdraft cores. Cyclonic vortex rings are associated with the main updraft cores and anticyclonic vortex rings are near the downdraft cores. These patterns around the stronger updraft/downdraft cores could be explained as follows. These areas have very strong horizontal gradients of w and these portions of ξ and η become more dominant than the vertical shear terms. As an example, around a strong updraft core, on the northwest side of the core, $\partial w / \partial x$ is strongly positive causing η to be a dominant negative value thus contributing to a southwest directed horizontal vorticity vector. On the southeast of the updraft core, $\partial w / \partial x$ is strongly negative causing η to be positive thus contributing to a northeast directed horizontal

vorticity vector. On the northeast side of the updraft core, $\partial w/\partial y$ is strongly negative causing ξ to be a dominant negative value thus, a northwest directed horizontal vorticity vector prevails. Rounding out around the updraft core, on the southwest side, $\partial w/\partial y$ is strongly positive thus ξ is a dominant positive resulting in a southeast directed horizontal vorticity vector. Thus, a counter-clockwise (cyclonic) circulation around the strong updrafts cores is a result and is highly evident.

As far as the circulation around the stronger downdraft cores, the principles are the same except the signs of $\partial w/\partial x$ and $\partial w/\partial y$ are reversed in the locations discussed about the updraft cores. Therefore, the circulation is reversed and clockwise (anticyclonic) rotation is the result. The stronger updraft/downdraft cores exhibited stronger horizontal vorticity vectors around the core and more defined rotation. These horizontal vortex rings developed above the low-level jet (LLJ) associated with this MCS. Since the cells embedded in this prefrontal convective rainband were, at best, moderate in intensity, these vortex rings are likely due to variations in the vertical shear of the horizontal winds and not due to rotation of the updrafts or downdrafts.

Figure 5.29 displays the horizontal variations of ξ superimposed on the system-relative horizontal winds for 3.75 km. With the exception of a strong positive center located at X=28 and Y=35, the field of ξ is overall weaker than

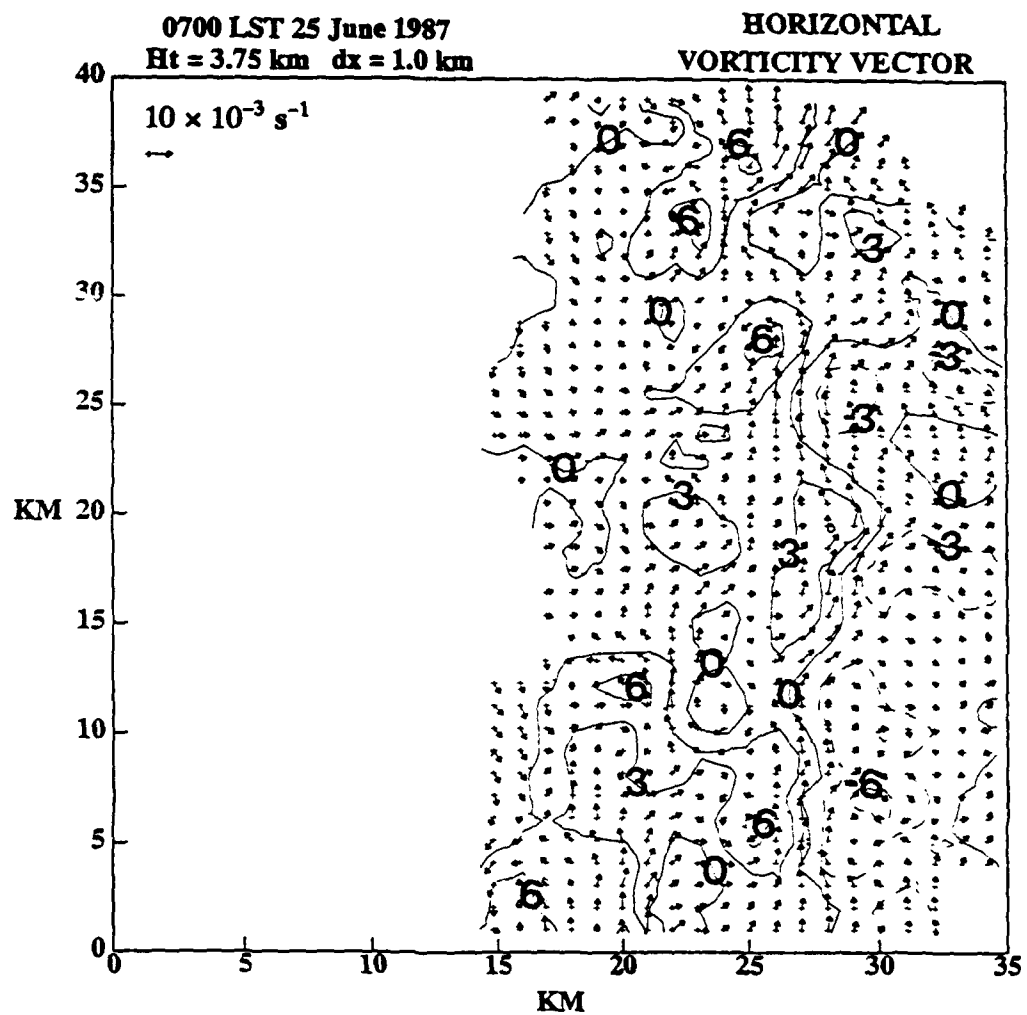


Fig. 5.28 Same as in Fig. 5.26 except for 3.75 km.

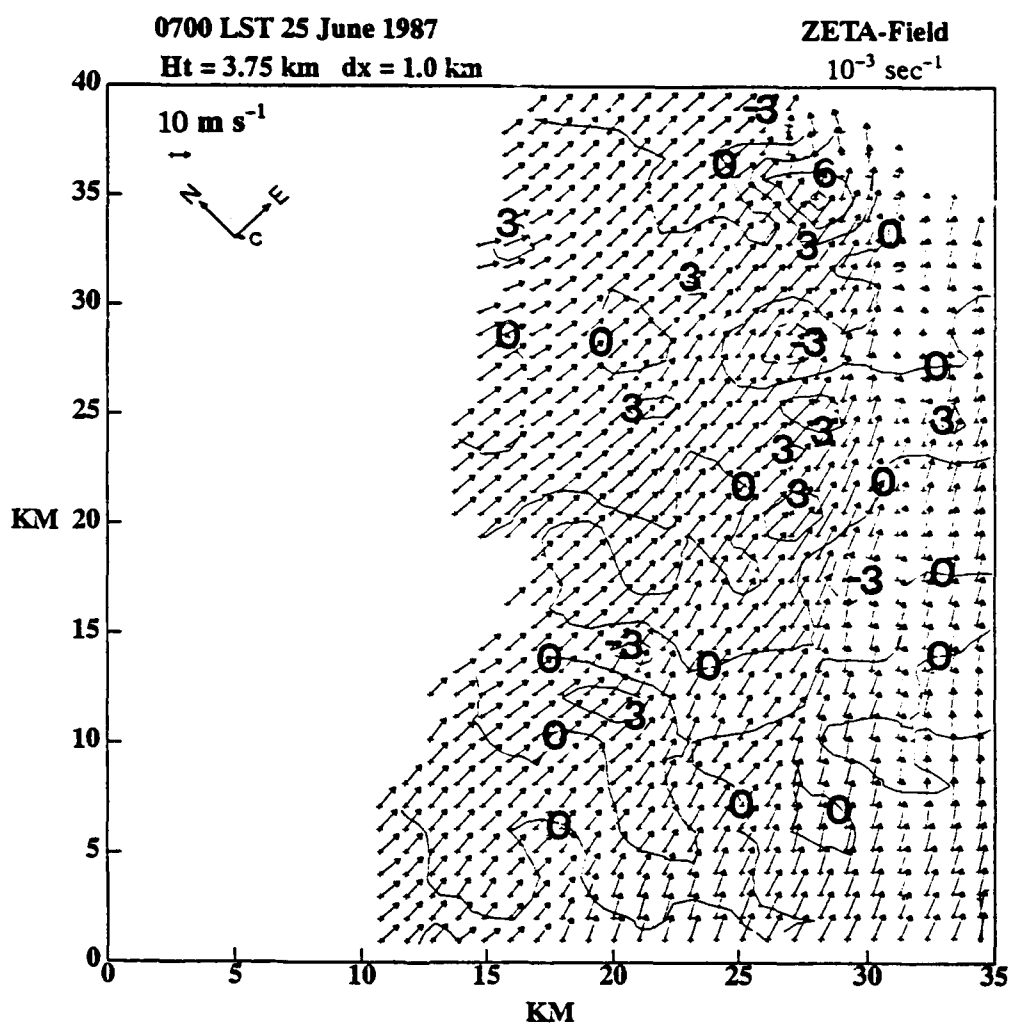


Fig. 5.29 Same as in Fig. 5.27 except for 3.75 km.

the η field but comparable to the ξ field. Comparing to 0.75 km, the pattern exhibits more positive/negative couplets throughout the domain. Unlike at 0.75 km, these positive/negative centers showed no correlation to the updraft/downdraft cores. However, the strong positive center at (28,35) was in an area where the strong updraft could advect positive ξ into a storm cell located along the gust front.

Figures 5.30 and 5.31 display the same features of the previous vorticity diagrams only at 6.75 km. Since the vertical shear of the v-component of the wind is strongly negative in the upper levels, ξ is primarily positive at this level. Eta (η) has several couplets of ± 6 to $8 \times 10^{-3} \text{ s}^{-1}$ thus any vortex rings evident at this level are due to the variability of the η field. The horizontal vorticity vectors at this level are primarily southeast directed with the strongest vectors located between the updrafts and downdrafts of the main cells. Several vortex rings are still evident at this level and the relationship between the cyclonic (anticyclonic) rotation around the updrafts (downdrafts) is still upheld. Figure 5.31 displays the ξ field superimposed on the system-relative horizontal winds for the 6.75 km level. The overall strength of the ξ field at this level is slightly stronger than at 3.75 km. Several areas of positive ξ is being horizontally advected into the gust front area (dotted line in Fig. 5.27). With the exception of the positive/negative couplet located near (29,35), the overall field strength of ξ was weaker than ξ and η fields at this level. Actually, this trend was found for almost all levels thus the significance of the hori-

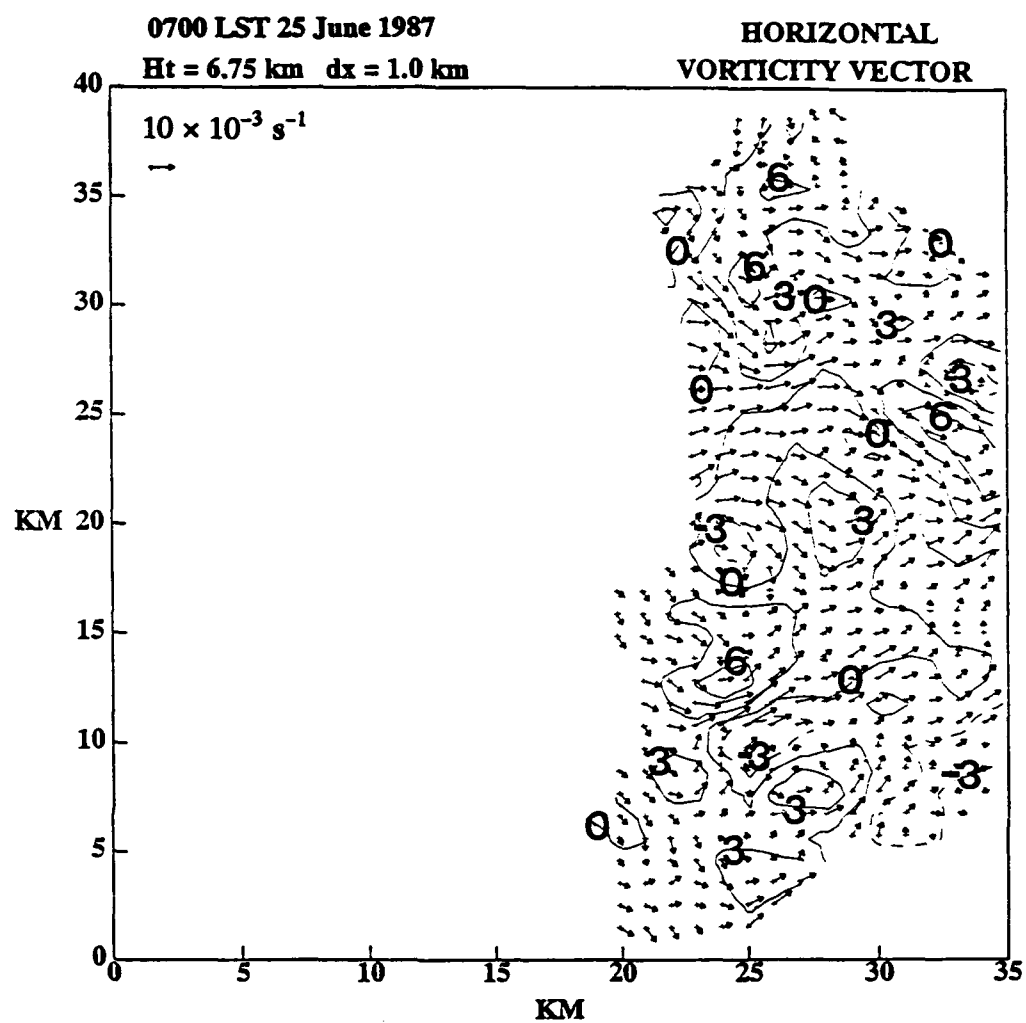


Fig. 5.30 Same as in Fig. 5.26 except for 6.75 km.

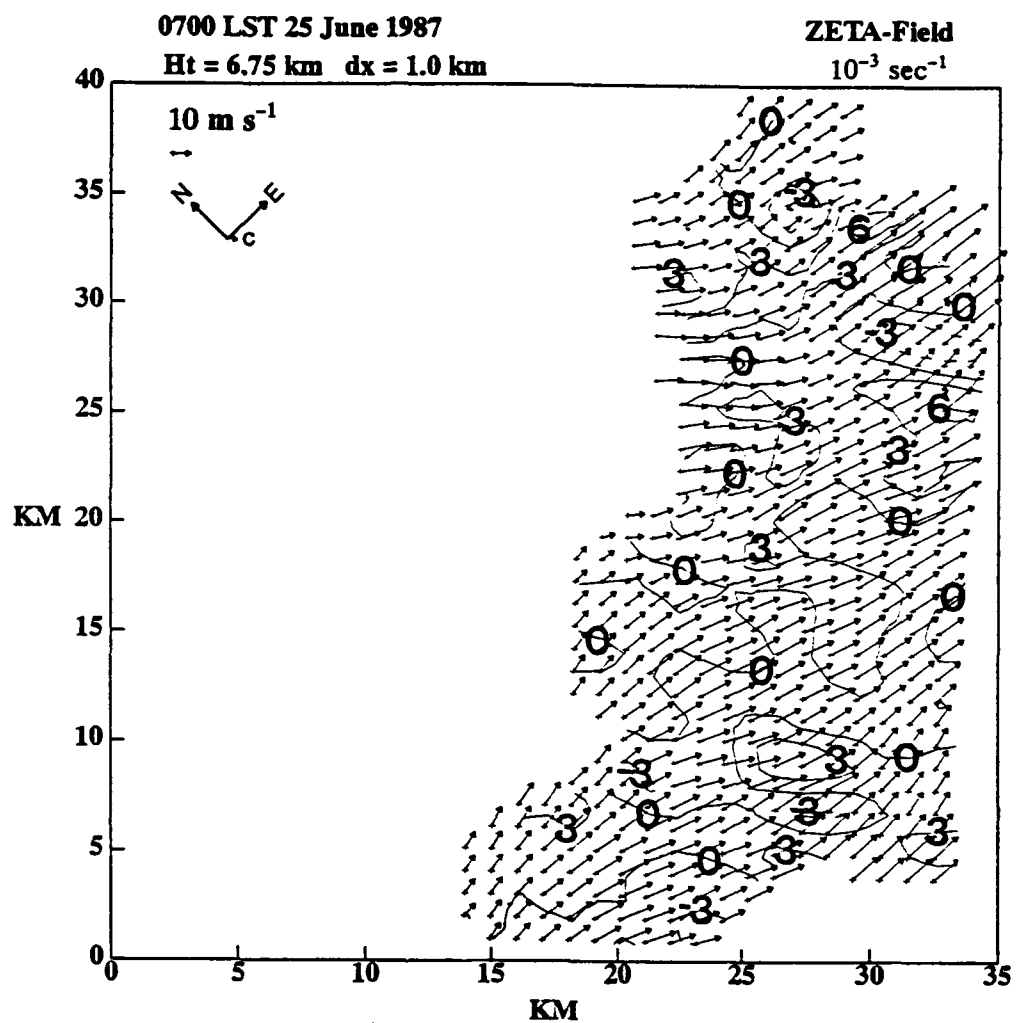


Fig. 5.31 Same as in Fig. 5.27 except for 6.75 km.

zontal vorticity fields must be watched for when analyzing the budgets.

Table 6 lists the area mean and the standard deviation values for each component of vorticity by level for the 25 km by 40 km horizontal domain of interest. This table was constructed from the values found in both volume scans in order to provide the "best-estimate" values for the prefrontal convective rainband under investigation. Typical magnitudes for each component are represented by the standard deviations (ξ_σ , η_σ and ζ_σ). Both ξ_σ and η_σ are slightly stronger than ζ_σ at all levels, this was evident in the previously discussed, level-by-level analysis of the horizontal variations of each term. Comparison of the area means (represented by the overbar of each component) shows that $\bar{\xi}$ and $\bar{\eta}$ were almost one order of magnitude larger than $\bar{\zeta}$ at most levels. From this table, the mean horizontal vorticity vector for a given level can be determined. This is depicted in Fig. 5.32. The numbers at the end of the arrows represent the particular level for that mean horizontal vorticity vector. In the lower levels, $\bar{\xi}$ is negative and $\bar{\eta}$ is positive thus the mean horizontal vorticity vector is towards the north. In the middle levels, the mean horizontal vorticity vector is towards the east since $\bar{\xi}$ and $\bar{\eta}$ are both positive and of nearly equal magnitudes. In the upper levels, the mean horizontal vorticity vector is towards the southeast as strong positive $\bar{\xi}$ dominates the weaker negative $\bar{\eta}$. Notice how the strength of the mean vectors reach their minimum values at 2.75 km and 3.75 km. This is an indication of a transition from the lower levels to the higher levels. This transition was evident in Fig. 5.28

Table 6

Area mean ($\bar{\quad}$) and standard deviation (σ) values for each vorticity component, over a 25 by 40 km² horizontal domain, based upon 0653 and 0700 LST 25 June data sets. Units are in 10⁻³ s⁻¹.

Z (km)	$\bar{\xi}$	ξ_{σ}	$\bar{\eta}$	η_{σ}	$\bar{\zeta}$	ζ_{σ}
0.75	-1.41	2.08	1.77	2.75	0.89	1.58
1.75	-1.55	2.24	2.02	2.66	0.55	1.41
2.75	-0.59	1.88	1.61	2.98	0.34	1.41
3.75	0.80	1.81	1.61	3.16	0.33	1.54
4.75	1.67	2.21	2.17	3.36	0.46	1.68
5.75	2.44	2.74	1.84	3.36	0.42	2.00
6.75	4.11	3.14	0.71	3.32	0.59	2.21
7.75	5.49	3.09	-0.27	3.14	0.89	2.47
8.75	5.82	3.48	-0.74	3.59	1.39	2.97

TAMEX IOP-13 MEAN HORIZONTAL VORTICITY VECTOR

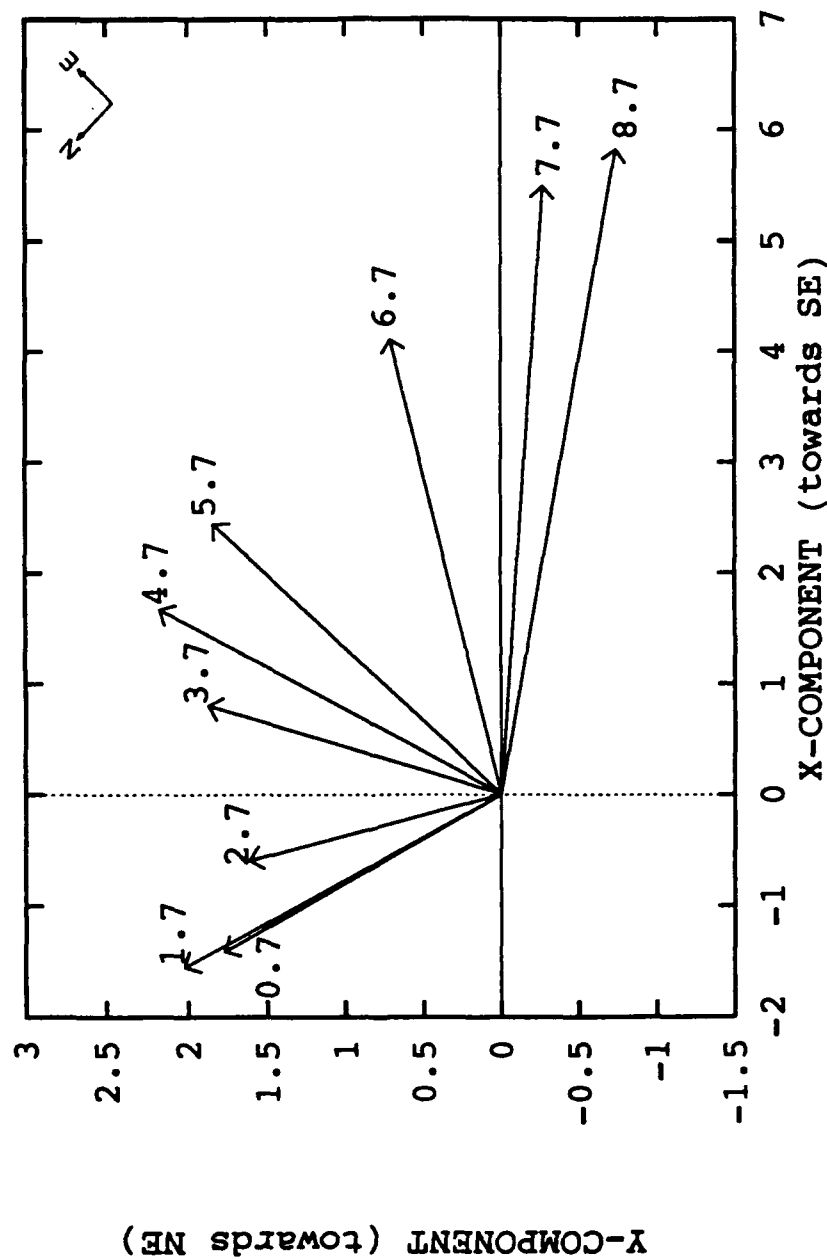


Fig. 5.32 The mean horizontal vorticity vectors ($\hat{i}\bar{\xi} + \hat{j}\bar{\eta}$) determined from $\bar{\xi}$ and $\bar{\eta}$ values contained in Table 6. Units are in 10^{-3} s^{-1} . The number at the vector arrowheads is the height in kilometers for that vector. The x-axis is positive towards the southeast and the y-axis is positive towards the northeast.

where there was the strongest variability in the horizontal vorticity vectors. This psuedo-hodograph of the mean horizontal vorticity vectors (Fig. 5.32) shows the intimate relationship between the vertical mean wind shear ($\partial \bar{u}/\partial z$ and $\partial \bar{v}/\partial z$) and the horizontal mean vorticity vector. Thus, there is a good chance that the horizontal vorticity components could interact with each other and/or with the vertical component to enhance circulation therefore prolonging the lifetime of the prefrontal convective rainband.

5.3.2 Horizontal Variations of Component Terms

Analysis of the horizontal variations of the four dominant terms in (4.25), (4.26) and (4.27) can provide a sound basis for the reliability of the vorticity budget analyses. To display and discuss the local variations of each of the terms for each level of the three components of vorticity would be both tedious and an overdisplay of the features. This discussion will highlight the main features pertaining to the 0.75, 3.75 and 6.75 km levels (representing the low, middle and upper levels, respectively). The horizontal variations for each component term at 3.75 km will displayed to illustrate their relative strengths and variabilities. Other levels will be displayed if their features are highly significant. For simplicity, I will use the term abbreviations described at the end of the methodology section. Very few studies found in the literature review discuss the horizontal variations in great detail. If they did, they did not employ the same methodologies used in this study thus comparisons are not attempted.

Figures 5.33, 5.34, 5.35, and 5.36 illustrate the horizontal variations of HAD, VAD, DIV and TILT for the x-component, ξ , of vorticity at 3.75 km. The field of HAD shows a vast distribution of positive and negative centers throughout the entire domain. The positive centers seem well balanced by negative centers of the same intensity, most couplets being $\pm 30-60 \times 10^{-6} \text{ s}^{-2}$. Keep in mind while viewing the diagrams that the contour labels are in $10 \times 10^{-6} \text{ s}^{-2}$. This pattern of positive/negative centers in quasi-balance was evident at both the lower and upper levels except that the intensities were generally weaker at lower levels and slightly stronger at upper levels. Positive centers were associated with the updraft cores and negative centers with downdraft cores, which was evident at all levels. Thus positive values of HAD of ξ were being transported upward and negative values advected downward. The horizontal variation of the vertical advection term (VAD) of η for 3.75 km is shown in Fig. 5.34. This term is determined by the sign of the vertical velocity, w , and how the component vorticity varies with height. Due to overall upward vertical motion and overall positive vertical shear of ξ at this level, this field is primarily negative with the negative centers associated with the updraft cores. Although weaker in magnitude (generally $20-30 \times 10^{-6} \text{ s}^{-2}$ weaker), the positive (negative) centers of VAD were nearly located where the negative (positive) centers of HAD were located. The fields of ξ VAD were weaker at lower levels because of the weaker vertical motions and relatively the same strength at upper levels. Figure 5.35 shows the plan view of the DIV term of (4.25) at 3.75 km. This term for ξ vorticity was much weaker than the other terms

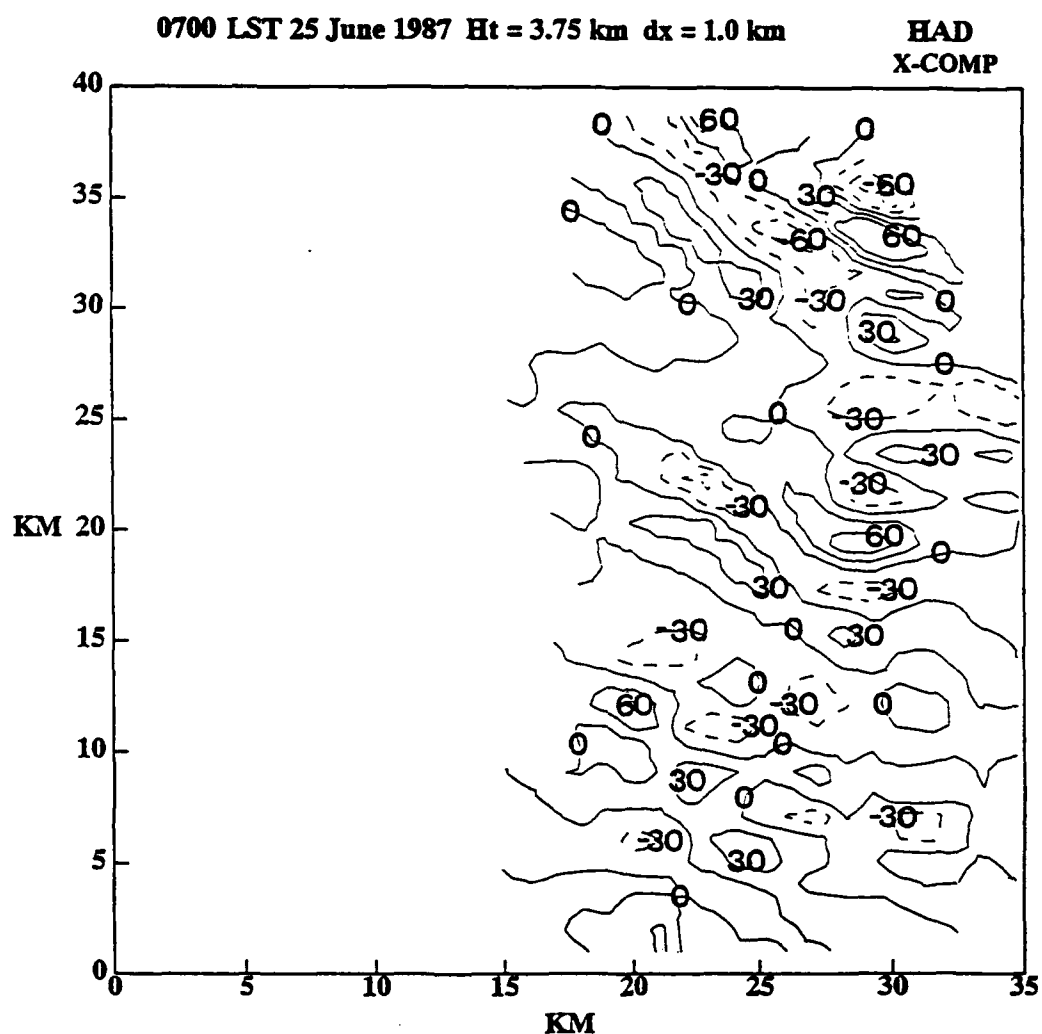


Fig. 5.33 Horizontal distributions of the horizontal advection (HAD) of the x-component of vorticity, ξ , at 3.75 km for 0700 LST 25 June 1987. Units are in $10^{-6} s^{-2}$. Contour interval is $30 \times 10^{-6} s^{-2}$ with negative values dashed. The x-axis is positive towards the southeast and the y-axis is positive towards the northeast.

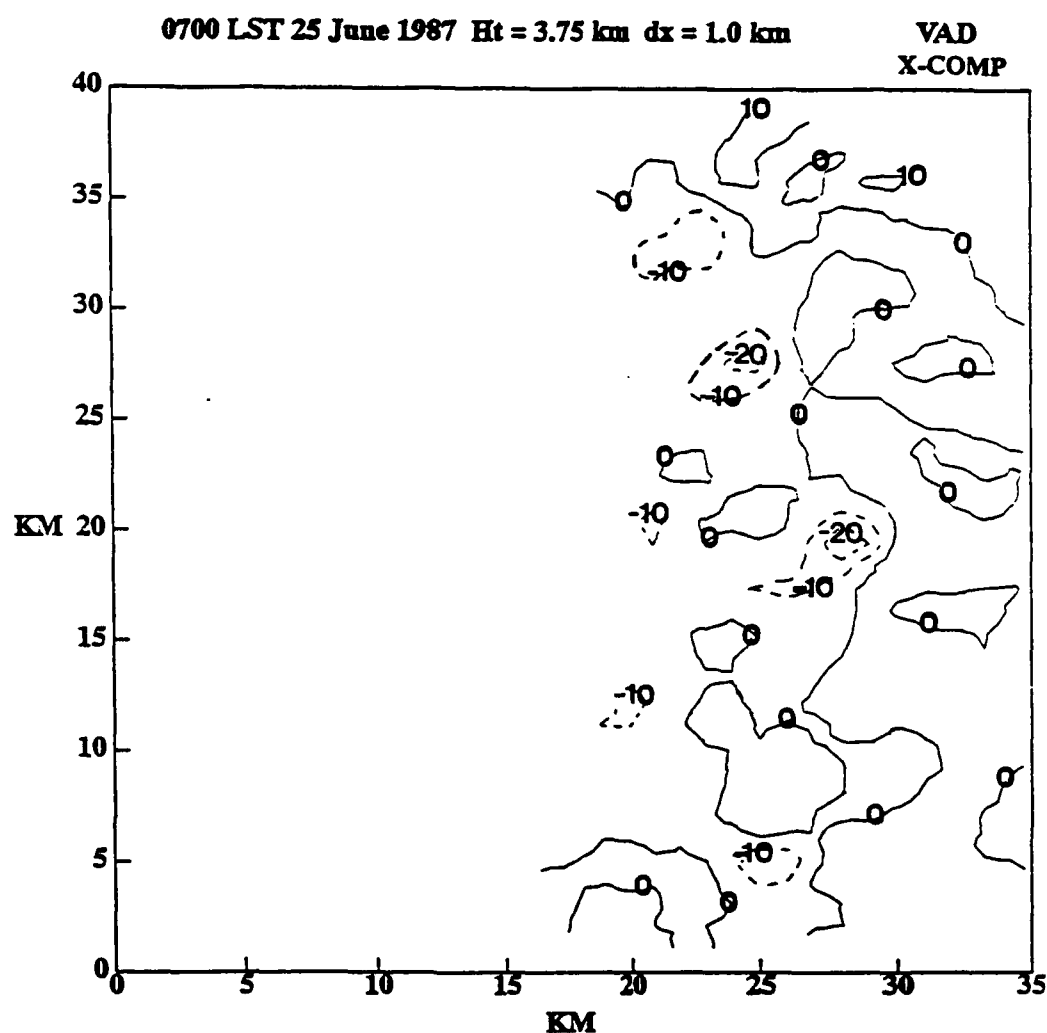


Fig. 5.34 Horizontal distributions of the vertical advection (VAD) of the x-component of vorticity, ξ , at 3.75 km for 0700 LST 25 June 1987. Units are in 10^{-6} s^{-2} . Contour interval is $10 \times 10^{-6} \text{ s}^{-2}$ with negative values dashed. The x-axis is positive towards the southeast and the y-axis is positive towards the northeast.

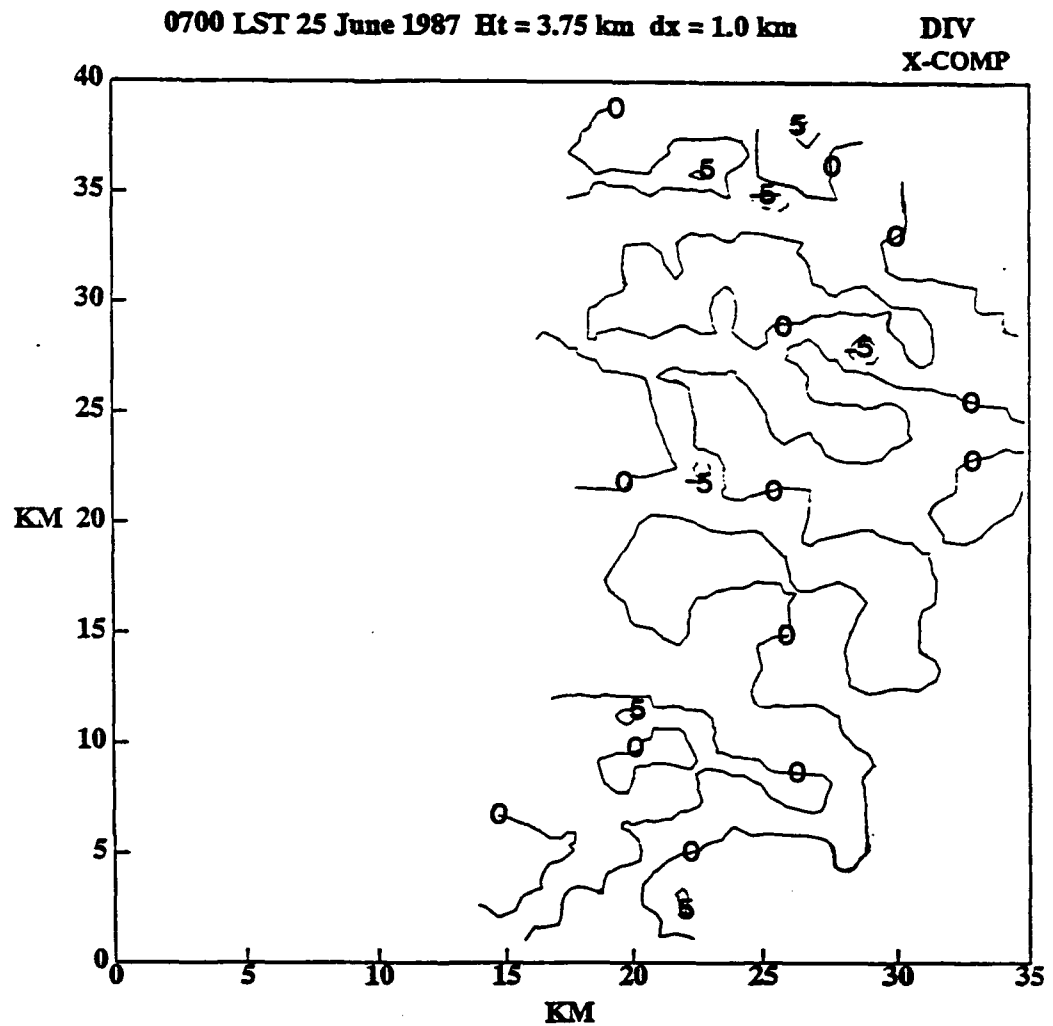


Fig. 5.35 Horizontal distributions of the divergence/convergence (DIV) of the x-component of vorticity, ξ , at 3.75 km for 0700 LST 25 June 1987. Units are in $10^{-6} s^{-2}$. Contour interval is $5 \times 10^{-6} s^{-2}$ with negative values dashed. The x-axis is positive towards the southeast and the y-axis is positive towards the northeast.

for almost all levels. The TILT term of (4.25) displayed in Fig. 5.36 also shows a weaker field than the HAD and VAD terms at 3.75 km. A similar weak field of TILT was found at 6.75 km but at 0.75 km (Fig. 5.37), there is a large area of positive TILT of ξ ahead of the wind-shift line (heavy dashed line). This is where overall positive upward vertical motion occurs thus these positive values of ξ TILT most likely add to the positive vertical vorticity, ζ , in this area (see Fig. 5.27).

The horizontal variations of HAD, VAD, DIV, and TILT for the y-component of vorticity, η , are displayed in Figs. 5.38 to 5.41. Like the x-component, the y-component of HAD (Fig 5.38) displays numerous positive/negative couplets with magnitudes of $\pm 30-60 \times 10^{-6} \text{ s}^{-2}$. However, the signs of these couplets are reversed from those in the general same location in the x-component of HAD (see Fig. 5.33). This tendency was also found at 0.75 km and 6.75 km (not shown). Thus, these two horizontal advection terms of the two horizontal components of vorticity tend to counteract each other in this case. Figure 5.39 shows the local variation of the VAD of η at 3.75 km. This field was much weaker than the corresponding x-component VAD. It is generally positive with the strongest values located at or near the updraft cores. Since w is overall positive for 3.75 km, these areas of positive VAD must be caused by a decrease of η with height. This was also found at 6.75 km. The positive centers of the VAD of η matched fairly well with the negative centers of the VAD of ξ , especially at middle and upper levels where vertical motions

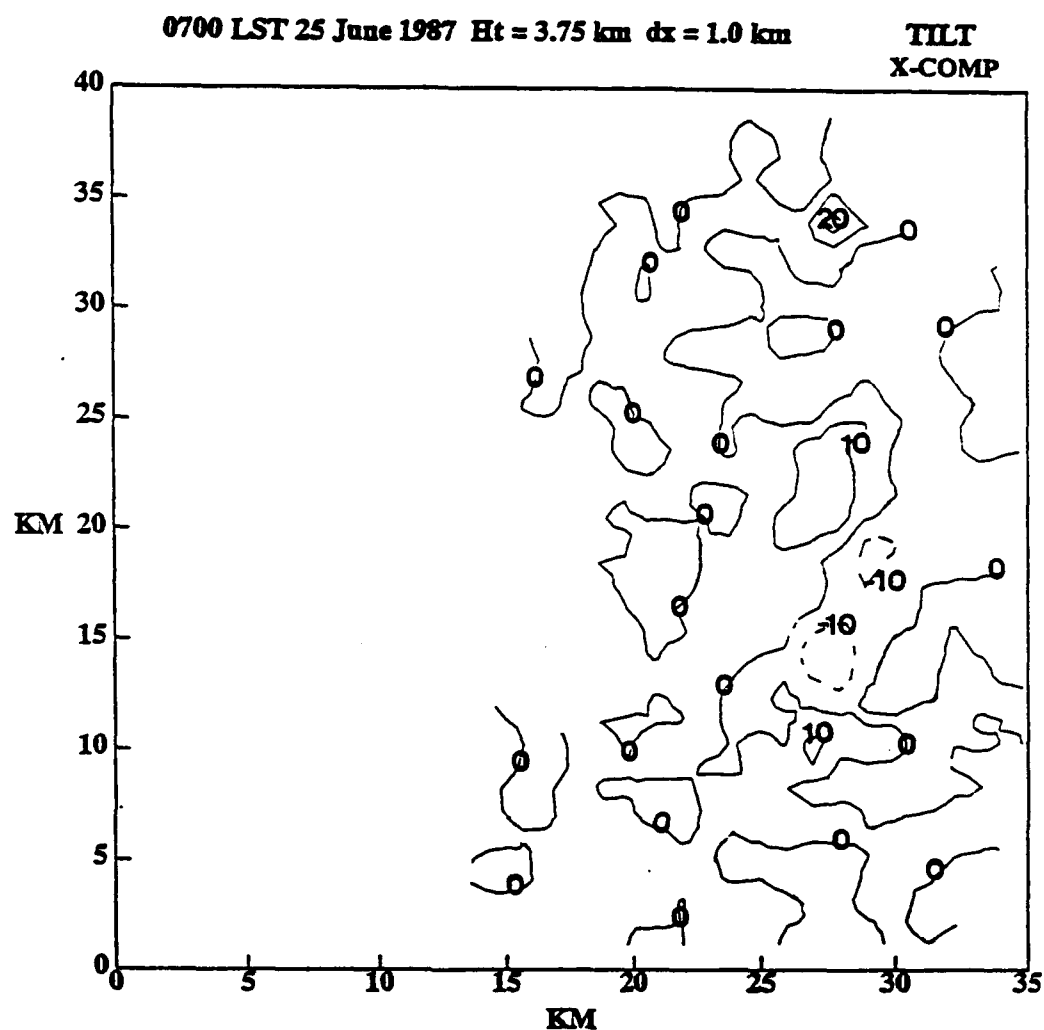


Fig. 5.36 Horizontal distributions of the tilting/tipping (TILT) of the x-component of vorticity, ξ , at 3.75 km for 0700 LST 25 June 1987. Units are in $10^{-6} s^{-2}$. Contour interval is $10 \times 10^{-6} s^{-2}$ with negative values dashed. The x-axis is positive towards the southeast and the y-axis is positive towards the northeast.

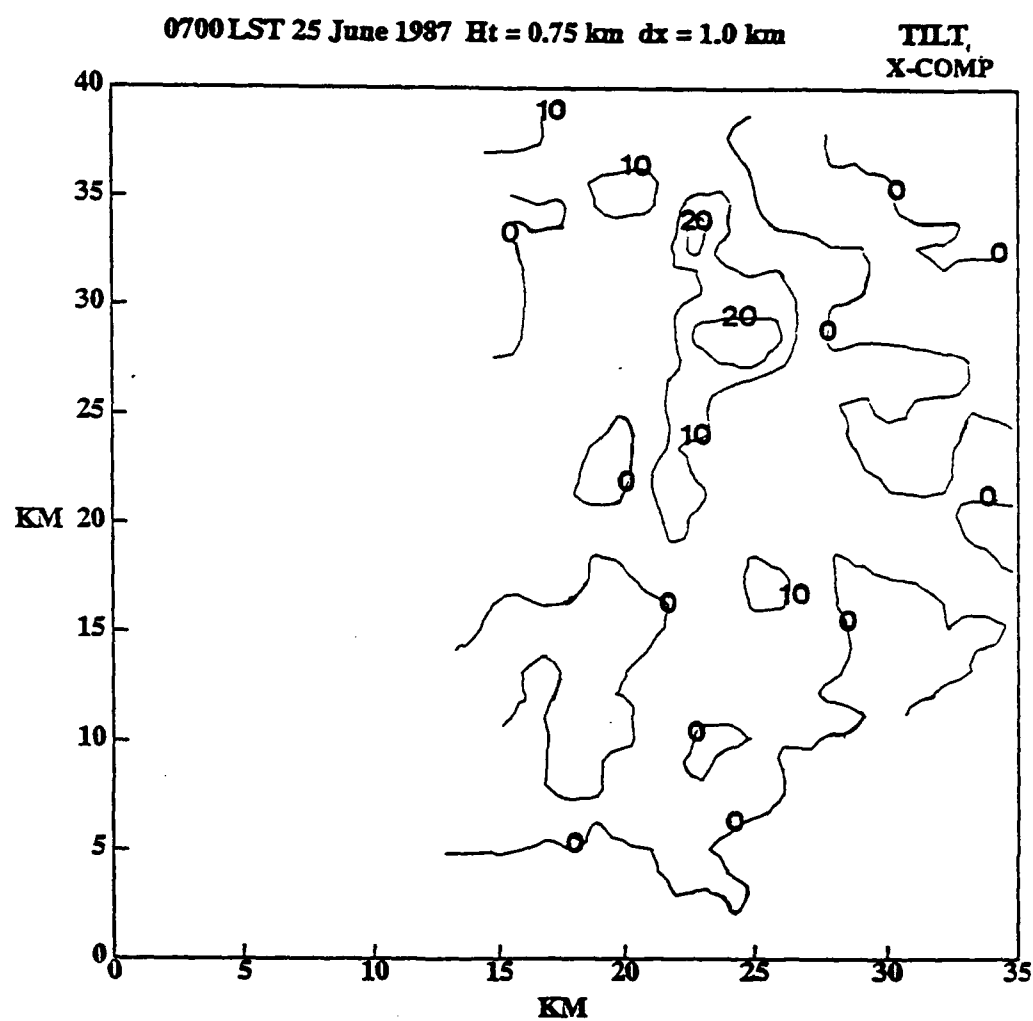


Fig. 5.37 Same as in Fig. 5.36 except for 0.75 km.

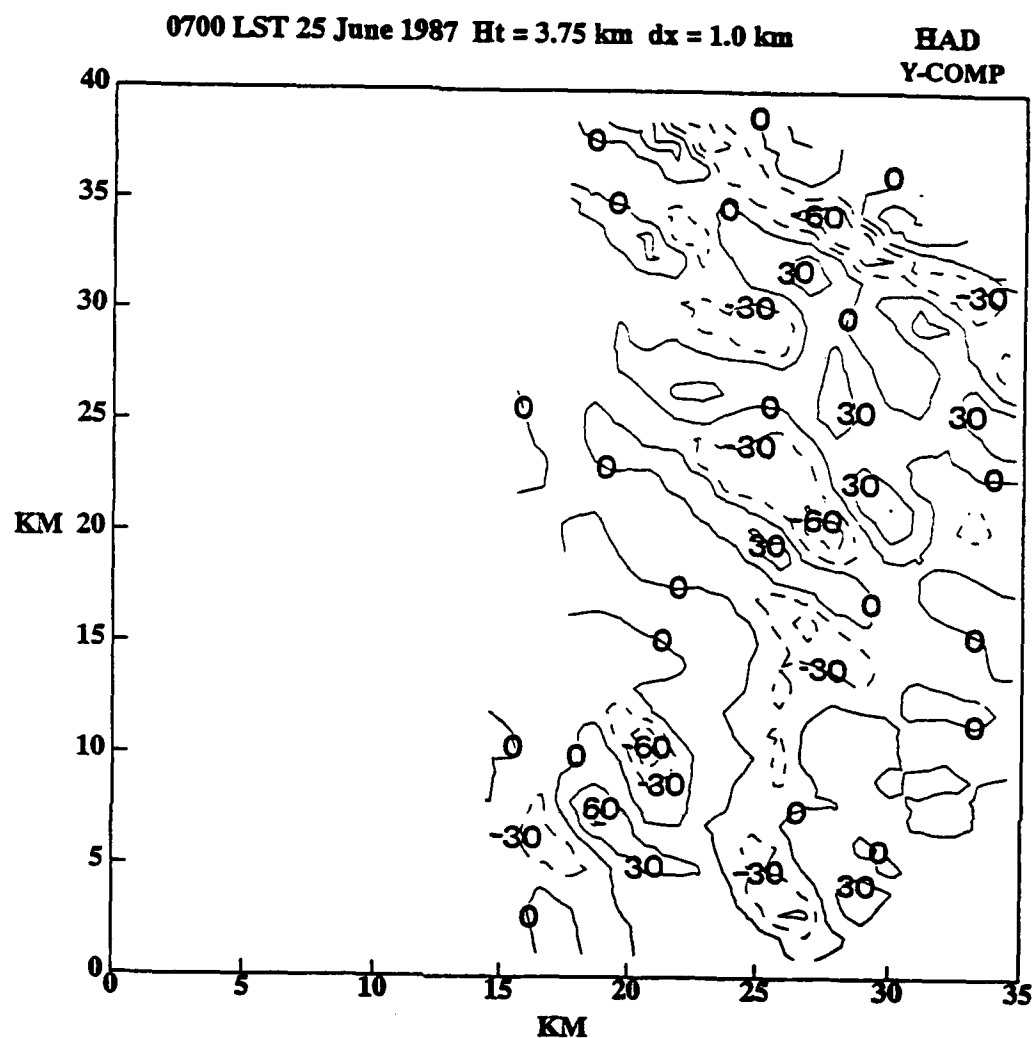


Fig. 5.38 Same as in Fig. 5.33 except for the y-component of vorticity, η .

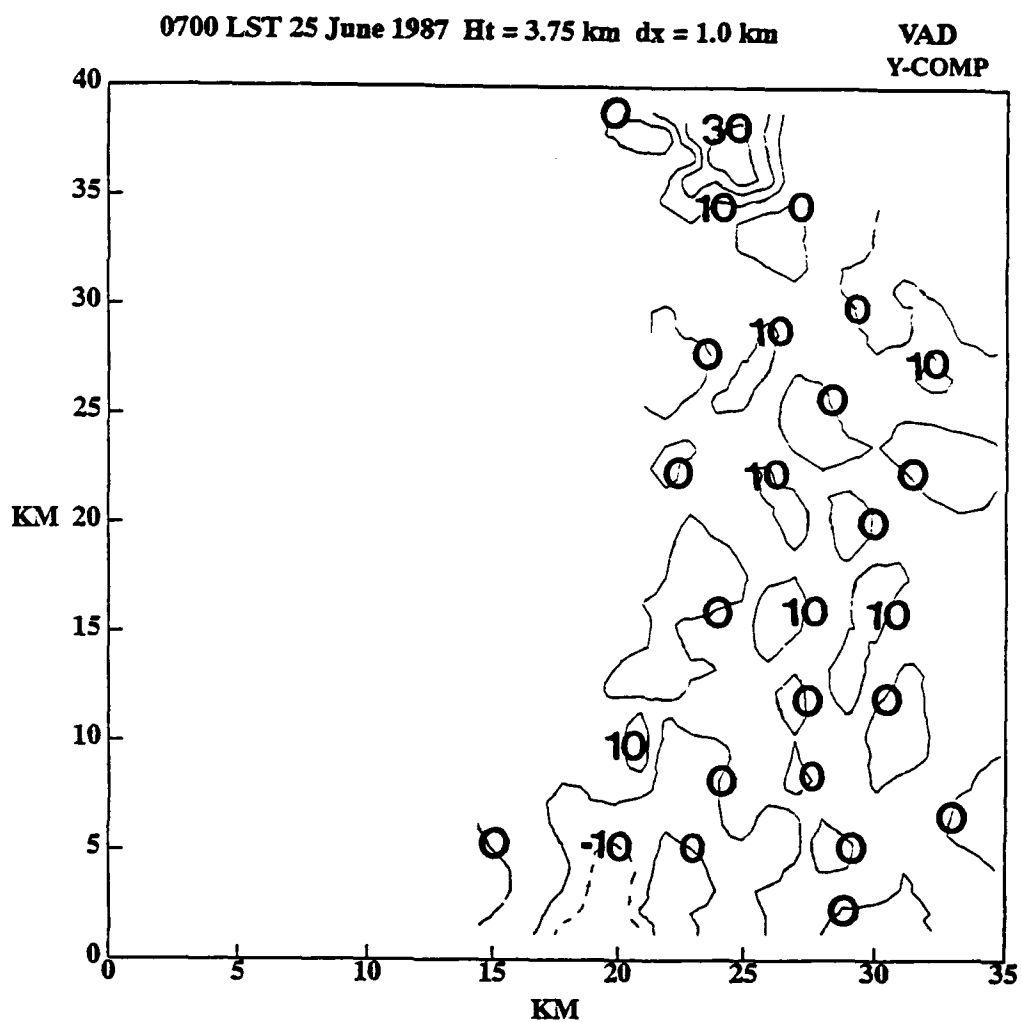


Fig. 5.39 Same as in Fig. 5.34 except for the y-component of vorticity, η .

are stronger. Thus like HAD for the horizontal vorticity components, VAD also worked against each other. The DIV horizontal variations for the y-component is shown in Fig. 5.40. A positive value of DIV in the immediate vicinity of an updraft or downdraft will enhance the positive vorticity of that component within that region by stretching the existing positive vorticity. This is evident in Fig. 5.40 and exists in many areas throughout the domain for all levels DIV for the y-component. The horizontal variation at 3.75 km of the y-component TILT term is illustrated in Fig. 5.41. This diagram shows that the y-component TILT field is generally negative at this level. Comparing to the other terms for η vorticity at this level, the TILT field is more variable than the DIV field but of the same strength for the positive/negative centers. Positive (negative) centers of TILT were located in the same areas as the negative (positive) centers of DIV thus they tend to offset each other at this level. Comparing TILT to HAD and VAD, HAD was a stronger field than TILT and VAD was an overall positive field, opposite to TILT.

Turning our attention to the z-component of vorticity, ζ , horizontal variations of the four main terms are presented in Figs. 5.42 to 5.45. The HAD term (Fig. 5.42) continues to exhibit the strongest field of the four terms. The orientation of the positive/negative couplets of HAD are directly related to the positive and negative centers of ζ in Fig. 5.29. The positive centers of HAD are located upstream of the positive ζ centers and the negative centers of HAD are downstream of the positive ζ centers. The orientation of these couplets is

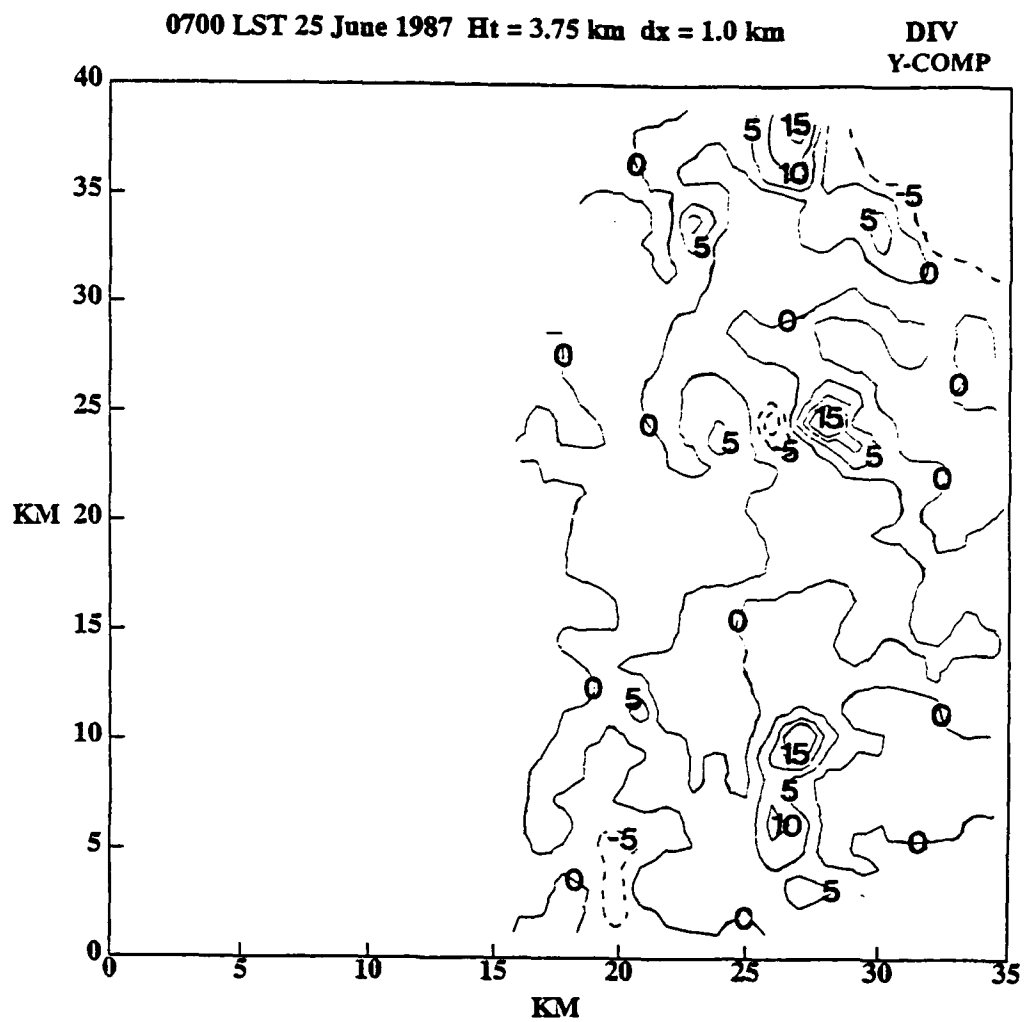


Fig. 5.40 Same as in Fig. 5.35 except for the y-component of vorticity, η .

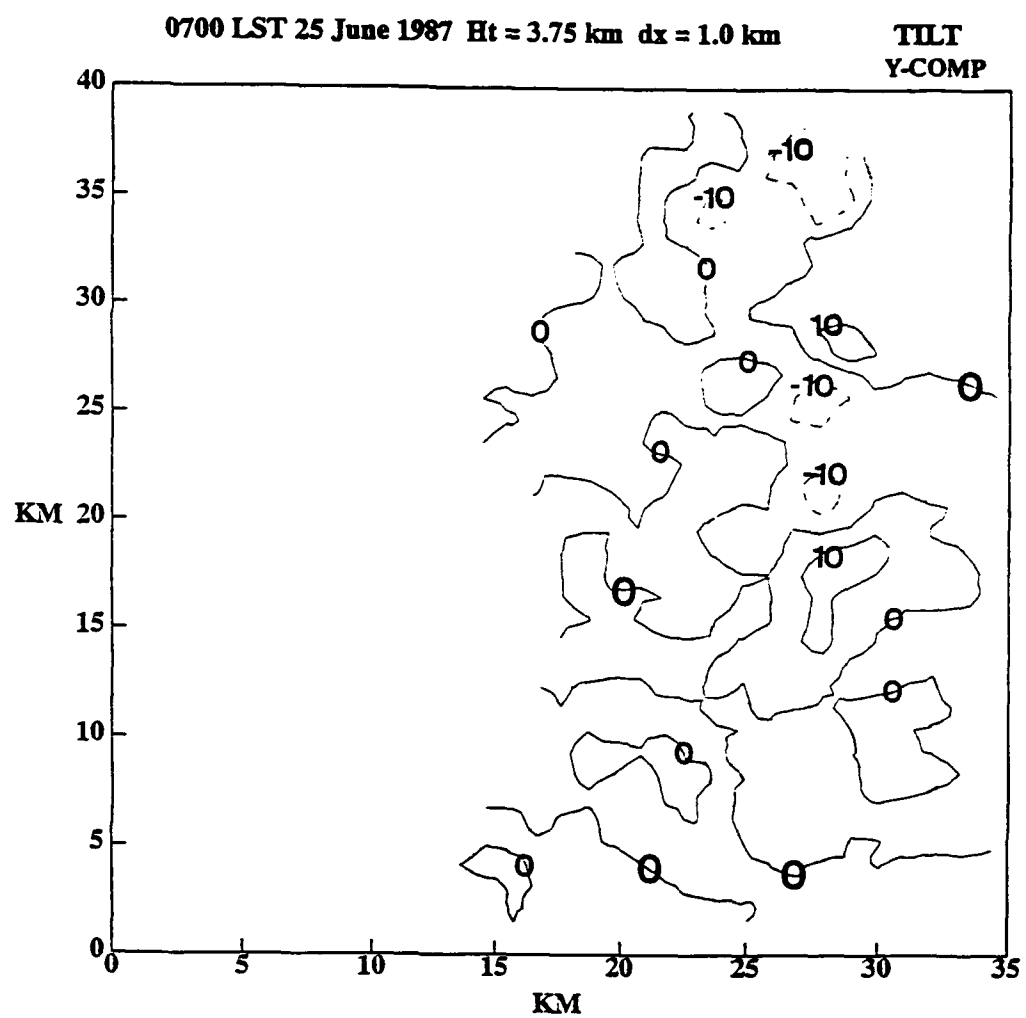


Fig. 5.41 Same as in Fig. 5.36 except for the y-component of vorticity, η .

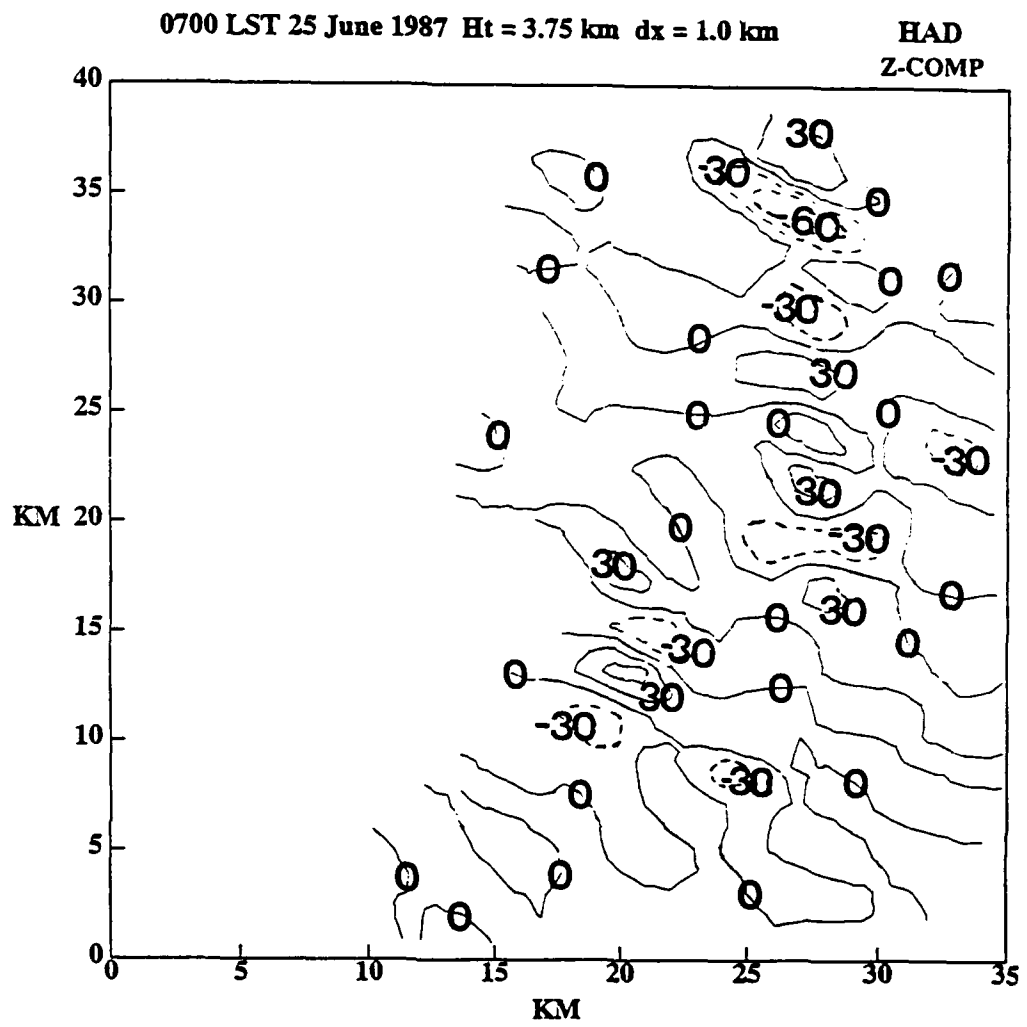


Fig. 5.42 Same as in Fig. 5.33 except for the z-component of vorticity, ζ .

such that neither positive nor negative HAD is dominating the entire domain and interpreting their effects on the individual convective cells is difficult for this type of case. Figure 5.43 is the plan view for VAD of ζ at 3.75 km. The VAD field is also weaker than the HAD field for this component. There was little association between the fields of these two terms at this level or any other level. Likewise, there was no direct relationship between the positive/negative centers of the VAD of ζ and the updraft/downdraft cores. Thus, this term can be affecting individual portions of the domain differently in both the horizontal and vertical. Figure 5.44 illustrates that DIV for ζ is an extremely weak field at 3.75 km, which was also evident at the other levels as well. The horizontal variation of TILT for ζ at 3.75 km is illustrated in Fig. 5.45. The field strength of TILT is considerably stronger than both VAD and DIV. The TILT term represents the conversion of horizontal vorticities to vertical. This process is particularly significant at the 3.75 km as depicted in Fig. 5.45. The dominance of this term in the vertical vorticity equation is expected for the mesoscale processes such as the one being studied here. This term becomes of secondary importance as the horizontal scale of motion increases. Viewing Fig. 5.45, we see several positive/negative centers spread throughout the entire domain. At 0.75 km (not shown), several positive centers are located ahead (to the southeast) of the wind-shift line where upward vertical motion can transport positive values of TILT upward into the main updrafts which could enhance the convective cells. At the mid-level view (Fig. 5.45), the positive centers are located near the main updrafts thus the same consequence could take place.

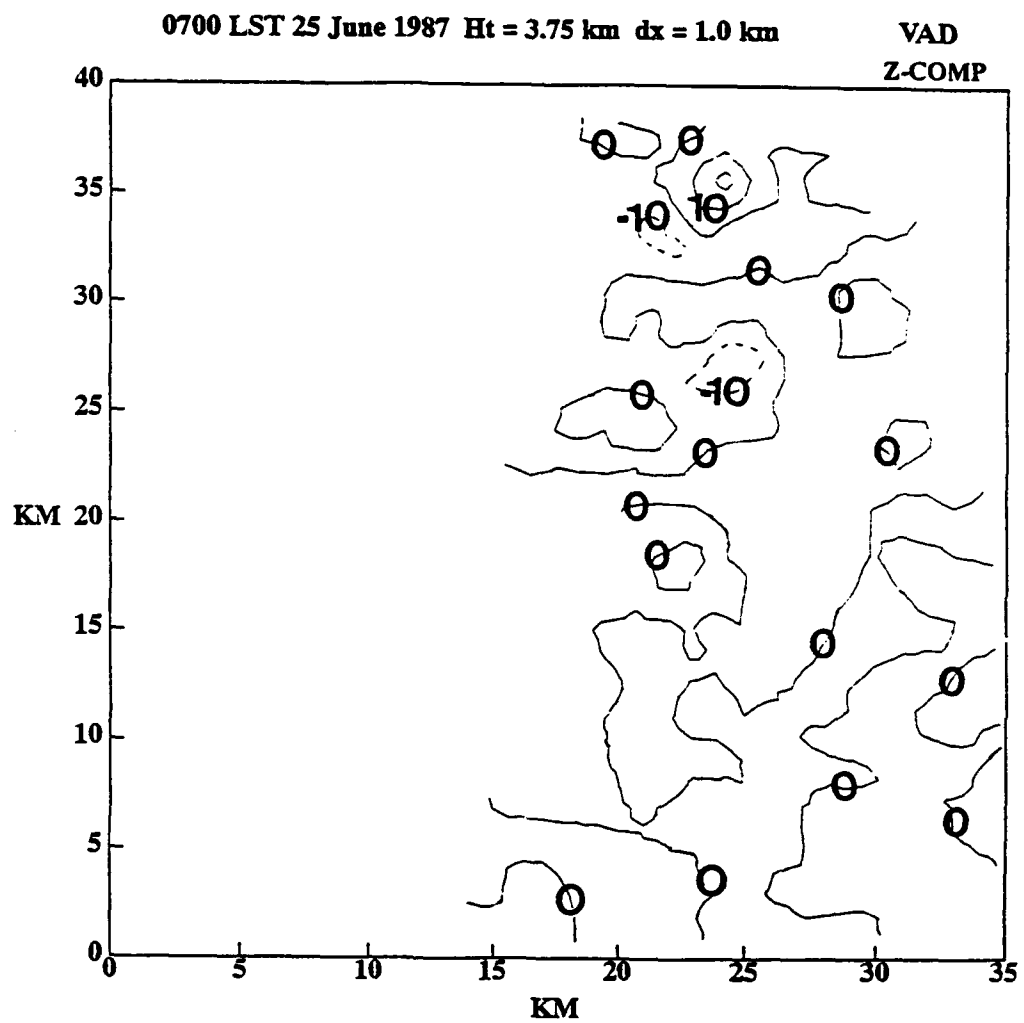


Fig. 5.43 Same as in Fig. 5.34 except for the z-component of vorticity, ζ .

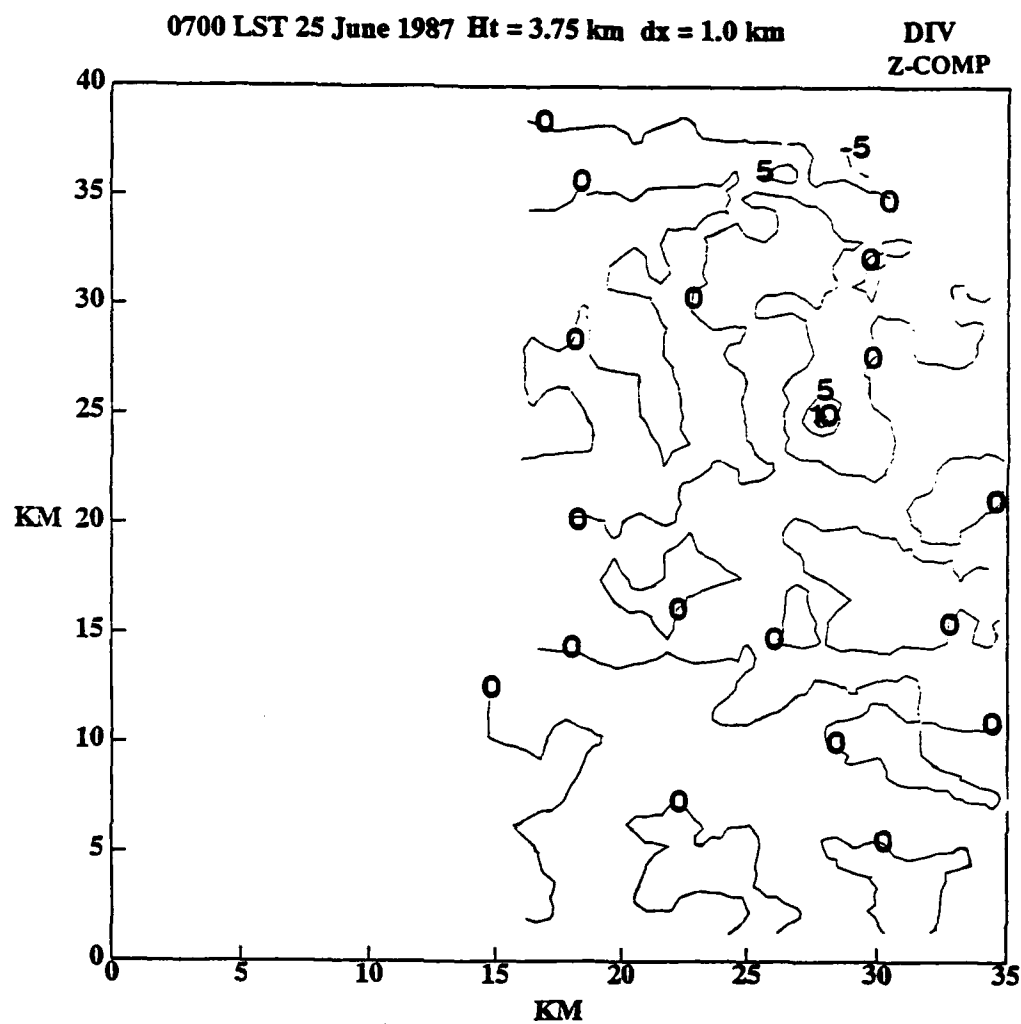


Fig. 5.44 Same as in Fig. 5.35 except for the z-component of vorticity, ξ .

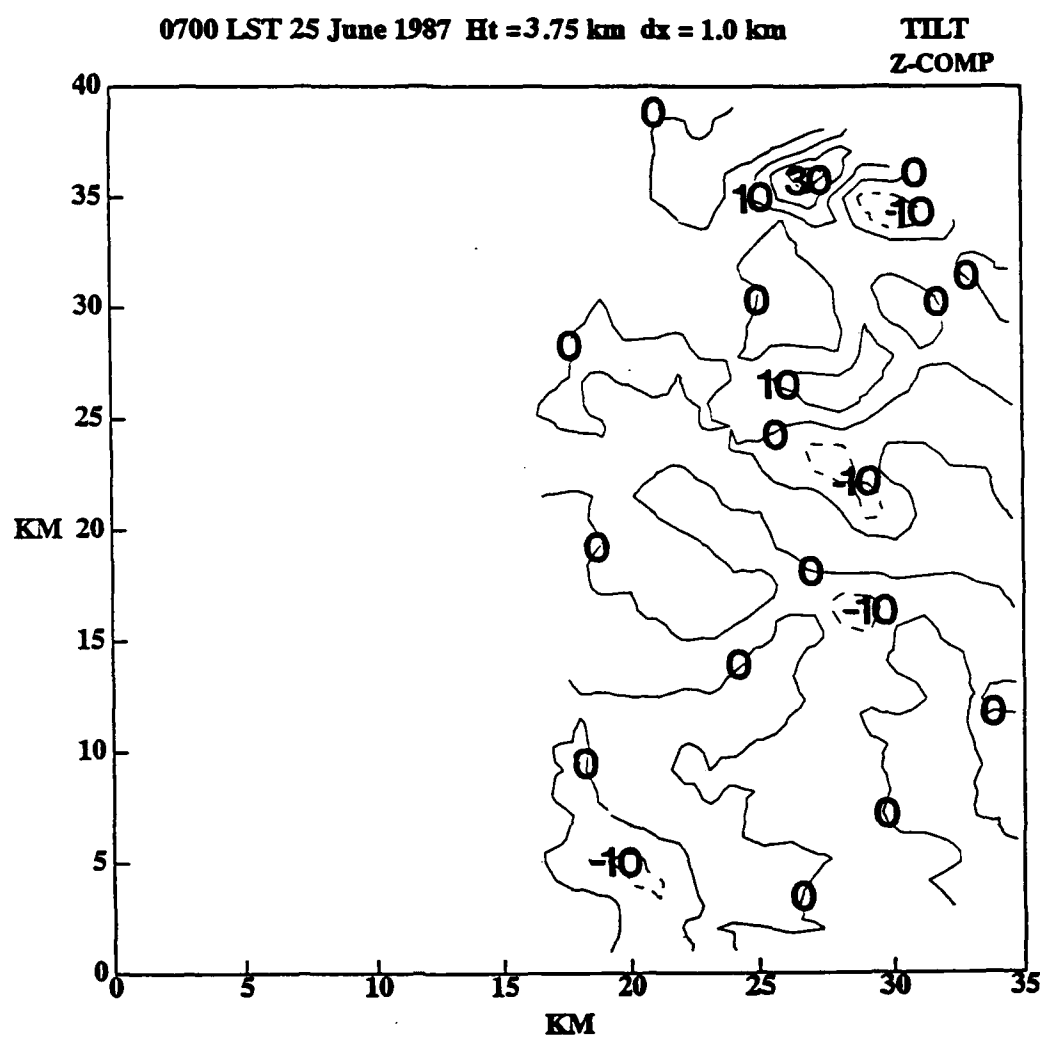


Fig. 5.45 Same as in Fig. 5.36 except for the z-component of vorticity, ζ .

These horizontal variations of the various terms for the three vorticity components illustrate that, for a mesoscale convective system of this nature, many processes are occurring throughout both the horizontal and vertical planes. An analysis of how each process is affecting the individual cells is very difficult unless you reduce the domain of interest. Thus to determine the effects of these processes on an MCS like the one studied here, the budgets of each component should be calculated and analyzed. Analyzing the horizontal variations is necessary in order to determine if the budget calculations are viable.

5.3.3 Analysis of the Vorticity Budget Calculations

Reiterating, the relative vorticity budgets for the component vorticity equations (4.24, 4.25 and 4.26) were calculated over a 25 km by 40 km rotated horizontal domain for the volume scans at 0653 and 0700 LST 25 June 1987. Also reiterating, Terms A-F on the right-hand side of these three equations represent the horizontal advection of the component in question (HAD), the vertical advection of that component (VAD), generation of component vorticity by divergence/convergence (DIV) with positive values representing convergence, the generation of vorticity by tilting/tipping the vorticity vector into the respective positive axial direction (TILT), the generation of component vorticity due to the solenoid term (which in this case study is neglected because of the anelastic assumption) and the generation/ dissipation of vorticity due to

frictional forces. The last term was determined using Austausch hypothesis with constant exchange coefficients and was found to be one to two orders of magnitudes smaller than the other calculated terms thus will not be presented in this discussion. The results from both volume scans were very comparable thus the results presented here are based upon both volume scan results in order to provide the "best-estimate" of the processes involved during IOP-13.

Table 7 lists the results of the "best-estimate" values for the four dominating processes in each of the component equations. It numerifies level-by-level the area means (denoted by the overbar) and the standard deviations (denoted by the sigma subscript) for HAD, VAD, DIV, and TILT for the rotated horizontal domain encompassing the prefrontal convective rainband. Since the area means for each component term are at least one order of magnitude smaller than their standard deviations at all but a few levels, the standard deviations may be considered the typical magnitudes of that term for the given level. Comparing the values of the calculated standard deviations to the magnitudes in the previously presented in the horizontal variation diagrams, it is easily seen that the budget calculations can be interpreted with a high level of confidence.

For the x-component, ξ , area mean of HAD is a sink below 3.75 km then a weak source in the middle levels. However, in the upper levels, HAD is a strong source ($\sim 4.0 \times 10^{-6} \text{ s}^{-2}$) of ξ vorticity generation. The area mean of the VAD term for the x-component is negative throughout the system depth with

Table 7

Area mean ($\bar{}$) and standard deviation (σ) of the vorticity budget terms for each component, over a 25 by 40 km² horizontal domain, based upon 0653 and 0700 LST 25 June data sets. Units are in 10⁻⁶ s⁻². Physical meanings of the budget terms are explained in the text.

X-COMPONENT (ξ)								
Z (km)	$\overline{\text{HAD}}$	HAD_σ	$\overline{\text{VAD}}$	VAD_σ	$\overline{\text{DIV}}$	DIV_σ	$\overline{\text{TILT}}$	TILT_σ
0.75	-0.32	12.48	0.20	2.13	-0.23	1.75	2.49	5.25
1.75	-1.03	15.29	-0.19	2.22	-0.34	1.95	2.26	5.01
2.75	-1.16	15.29	-0.92	3.99	-0.05	1.60	0.89	3.82
3.75	0.38	24.40	-1.21	5.05	0.08	1.72	0.48	4.35
4.75	0.32	28.96	-1.39	5.25	0.01	2.75	0.41	5.05
5.75	0.97	34.67	-1.68	6.80	0.14	3.55	0.73	6.82
6.75	2.76	36.26	-1.22	8.15	0.41	5.75	1.22	8.75
7.75	4.86	28.59	-0.59	5.27	-0.27	8.52	0.36	11.50
8.75	3.87	30.94	-0.11	3.62	0.15	9.02	-1.29	12.52
Total	10.65		-7.11		-0.10		7.55	
Y-COMPONENT (η)								
Z (km)	$\overline{\text{HAD}}$	HAD_σ	$\overline{\text{VAD}}$	VAD_σ	$\overline{\text{DIV}}$	DIV_σ	$\overline{\text{TILT}}$	TILT_σ
0.75	-0.47	13.82	0.69	3.44	0.24	2.69	0.78	4.55
1.75	-1.48	15.49	0.70	4.29	0.43	3.00	0.02	3.73
2.75	-2.37	21.31	1.43	6.44	0.32	2.75	-0.24	3.28
3.75	-3.58	24.91	2.22	7.73	0.20	3.65	-0.06	3.85
4.75	-5.27	32.95	3.15	7.49	0.45	3.78	-0.03	4.42
5.75	-4.96	41.96	3.64	8.16	0.94	3.95	0.08	4.82
6.75	-4.29	44.09	2.81	7.99	0.87	3.74	0.65	8.88
7.75	-1.56	34.31	0.72	5.56	1.09	4.70	0.01	9.57
8.75	-1.02	35.59	-0.27	3.51	1.42	8.76	-0.59	11.22
Total	-25.00		15.09		5.96		0.62	
Z-COMPONENT (ζ)								
Z (km)	$\overline{\text{HAD}}$	HAD_σ	$\overline{\text{VAD}}$	VAD_σ	$\overline{\text{DIV}}$	DIV_σ	$\overline{\text{TILT}}$	TILT_σ
0.75	-0.45	11.37	0.25	1.54	0.01	1.57	0.43	3.25
1.75	-0.54	12.44	0.53	2.52	0.07	1.47	-0.07	3.59
2.75	-0.20	16.09	0.46	3.06	0.02	1.21	-0.04	4.18
3.75	-0.22	18.61	-0.12	3.33	0.03	1.41	0.47	5.27
4.75	0.49	21.27	0.02	3.78	-0.07	1.67	-0.05	6.32
5.75	0.72	24.67	-0.35	3.67	-0.03	2.38	0.36	7.75
6.75	0.58	24.77	-0.42	3.93	-0.04	2.88	0.43	8.55
7.75	0.31	24.75	-0.32	3.56	-0.01	4.81	0.04	8.79
8.75	0.21	24.23	-0.19	3.94	-0.47	7.58	-0.18	8.39
Total	0.90		-0.14		-0.49		1.39	

the strongest negative values ($\sim 1.5 \times 10^{-6} \text{ s}^{-2}$) within the middle levels. The area mean for the DIV term is generally much weaker than the HAD and VAD but does show divergence (negative values) of ξ vorticity at lower levels and convergence of ξ above 2.75 km (with the exception of one level). The area mean of the TILT term shows that TILT is a source for ξ vorticity generation throughout all levels below 8.75 km. Its strongest positive values ($\sim 2.4 \times 10^{-6} \text{ s}^{-2}$) are located in the lowest two levels thus showing that this component of horizontal vorticity overall adds to the vertical component of vorticity through tilting. Figure 5.46 shows the vertical profiles of these four terms for the x-component. It is easy to see that TILT is an important contributor to the positive generation of ξ vorticity in the lower levels and that HAD is a large source in the upper levels. The VAD and TILT terms are in quasi-balance between 3-8 km. It is also easy to see that the area mean for the DIV term is much smaller than the other terms although its standard deviation values are on the same order of magnitude of the VAD and TILT terms. For the x-component, (as well as for the other two components of vorticity) the typical magnitudes of the HAD term is generally one order of magnitude larger than the other three terms.

For the y-component (η), area means for HAD and VAD are generally opposite in sign of their x-component counterparts. Recall that the positive (negative) centers of y-component HAD and VAD were generally located where the negative (positive) centers of x-component HAD and VAD were

TAMEX IOP-13

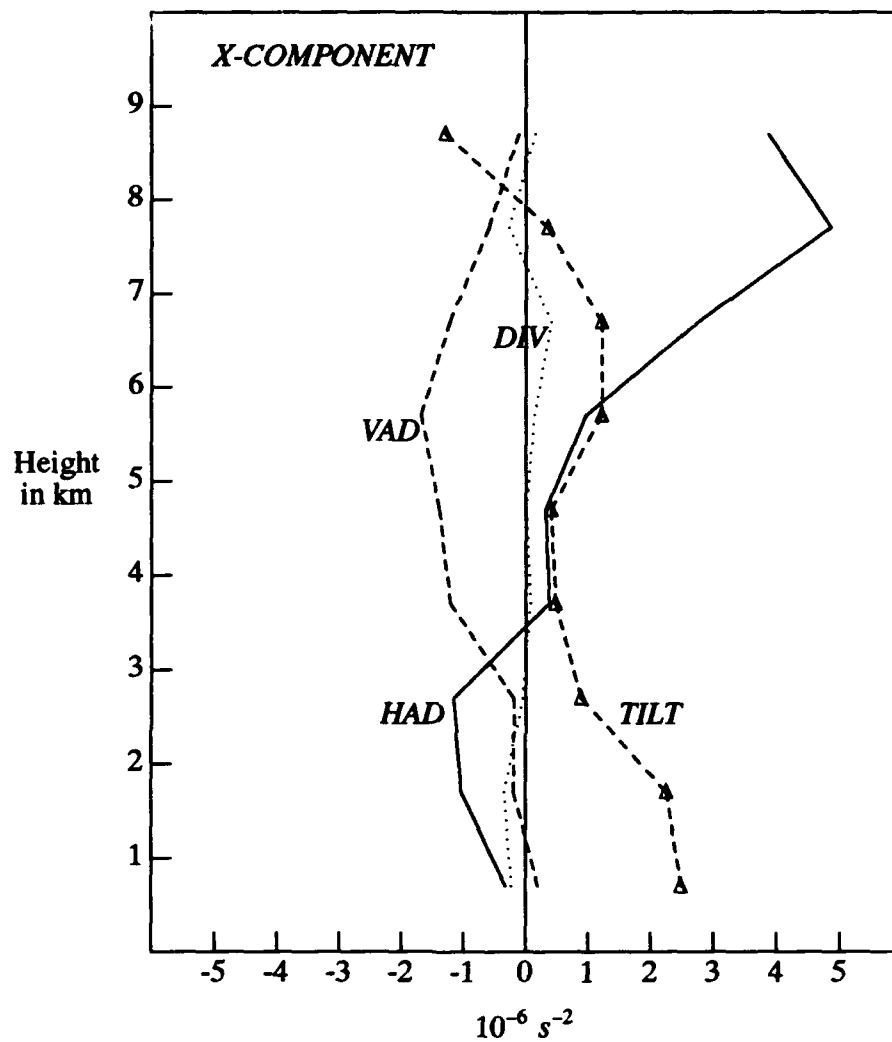


Fig. 5.46 Vertical profiles of the vorticity budget terms for the x-component averaged over the domain of interest, based upon 0653 and 0700 LST 25 June data sets. Units are in $10^{-6} s^{-2}$.

located. The area mean of the HAD term shows that it is a sink at all levels with the strongest negative values between 3.75 km and 6.75 km ($\sim 5.0 \times 10^{-6} \text{ s}^{-2}$). This is also where the strongest positive values ($\sim 3.25 \times 10^{-6} \text{ s}^{-2}$) for the area mean of VAD were located. Thus the VAD term is acting as a source, counteracting the effects of the HAD term. Both the area means for the DIV and TILT terms are much smaller than HAD and VAD. The DIV term is a weak source of η below 4.75 km and a slightly stronger source above thus DIV is a source at all levels. For the y-component, the area means of TILT are highly variable and weak throughout the system depth, which is different from the x-component of TILT where it was a source at almost all levels. The vertical profiles for the y-component area means of these four terms are illustrated in Fig. 5.47. These profiles show that, for the y-component of vorticity, HAD and VAD are in quasi-balance at all levels and are significantly stronger than the DIV and TILT terms.

For the z-component (ζ), area means are significantly smaller for all four terms than their x- and y-component counterparts. However, the typical magnitudes of the z-component terms are comparable to those found in the other two components. Thus for the z-component, the positive and negative areas for the individual terms were more than likely in near balance. Nevertheless, the area mean for the HAD of ζ shows that it acts as a sink of ζ generation below 4.75 km and acts as a source at and above 4.75 km. The VAD term was opposite in sign from HAD at all but two levels (3.75 km and 4.75 km). Figure 5.48

TAMEX IOP-13

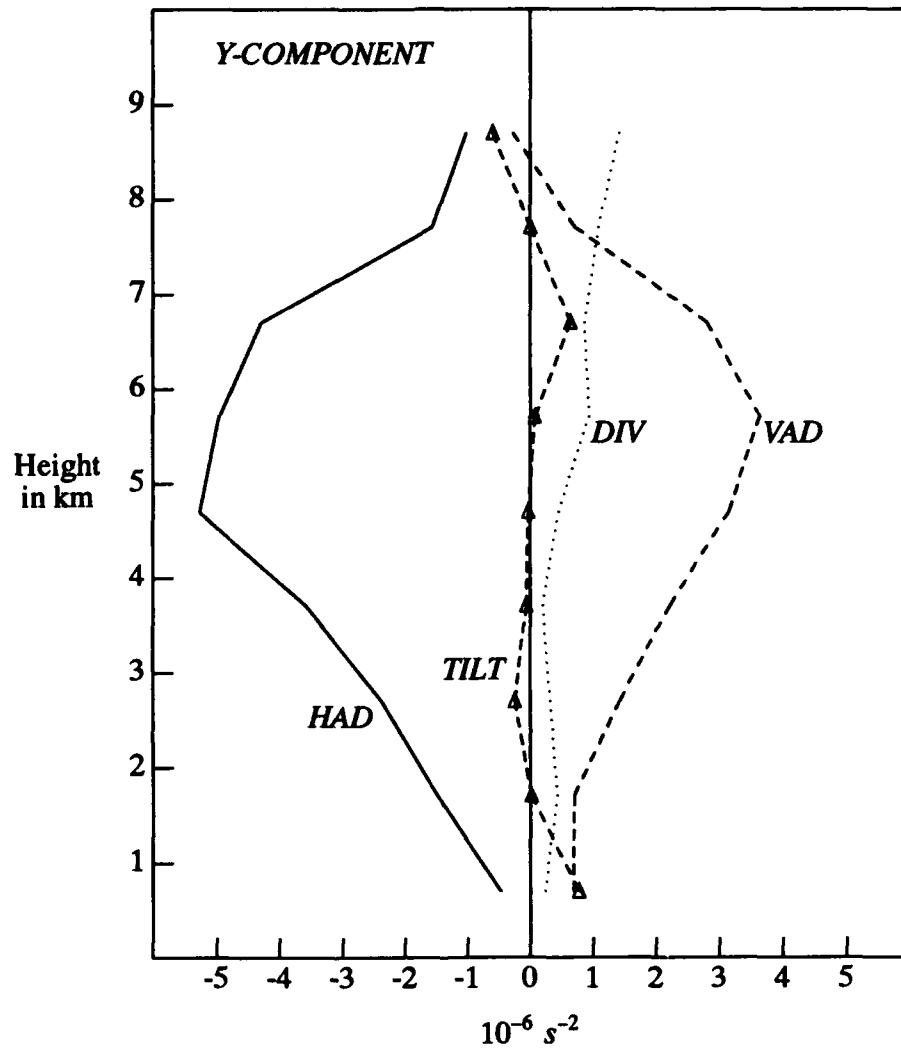


Fig. 5.47 Same as in Fig. 5.46 except for the y-component.

TAMEX IOP-13

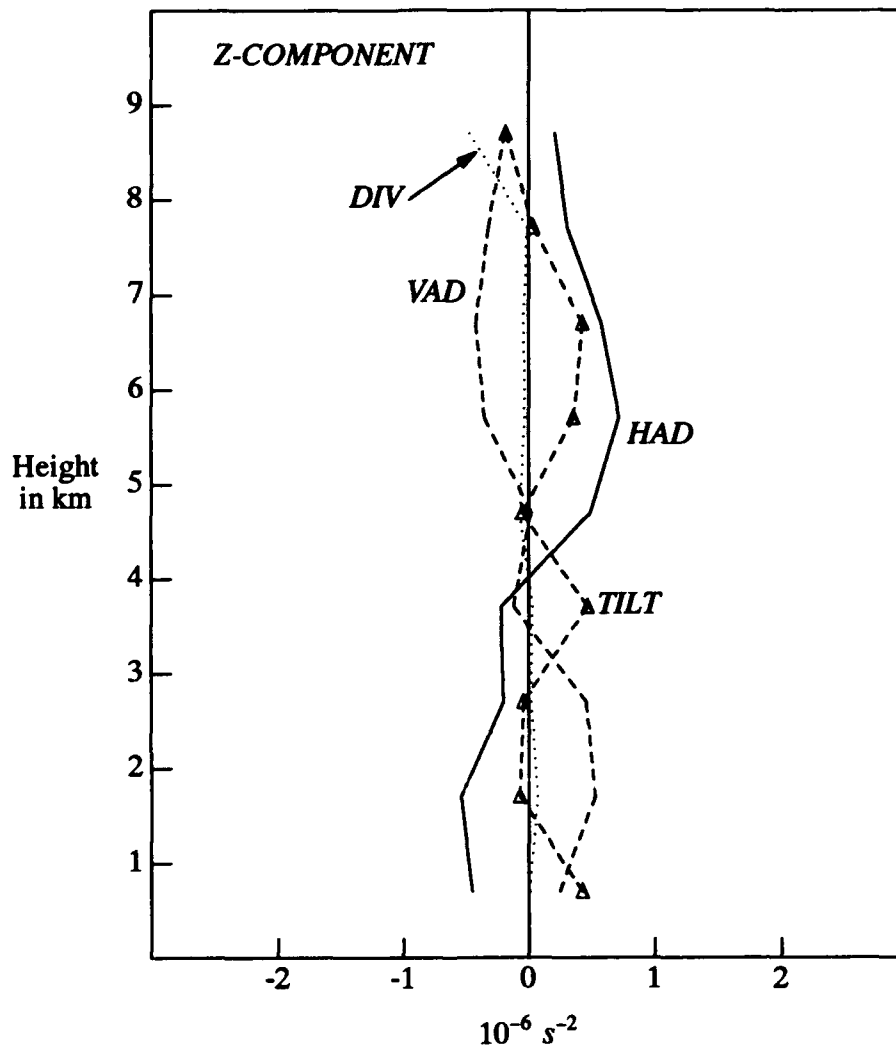


Fig. 5.48 Same as in Fig. 5.46 except for the z-component. Note that the scale used for the x-axis is one-half those in Figs. 5.46 and 5.47. This is because the z-component terms are smaller in magnitude than the x- and y-component terms.

displays the vertical profiles of the four area mean terms for the z-component of vorticity. Note that the x-axis has smaller values than the x-axes in the x- and y-component vertical profile figures. Thus, a direct visual comparison between these should not be made. Figure 5.48 shows that HAD and VAD for ζ are in near balance and that DIV and TILT are overall much smaller than HAD and VAD at almost all levels.

The vertical totals of the area mean for each component term is also shown in Table 7. The HAD term is an overall source ($10.65 \times 10^{-6} s^{-2}$) for ξ but a strong sink ($-25.00 \times 10^{-6} s^{-2}$) for η . The VAD terms acted oppositely to this. The VAD term for ξ is a moderate sink ($-7.11 \times 10^{-6} s^{-2}$) and a strong source ($15.09 \times 10^{-6} s^{-2}$) for η . Thus these two terms (HAD and VAD) for the horizontal vorticity components were generally in balance of each other for this case. Looking at the other two terms for the horizontal components, TILT was an overall moderate source ($7.55 \times 10^{-6} s^{-2}$) for ξ generation and a weak source ($0.62 \times 10^{-6} s^{-2}$) for η generation. The DIV term acted as a weak sink ($-0.10 \times 10^{-6} s^{-2}$) for ξ but a moderate source ($5.96 \times 10^{-6} s^{-2}$) for η . The vertical totals of the z-component area means showed that HAD and TILT acts as weak sources (0.90 and $1.39 \times 10^{-6} s^{-2}$, respectively) for ξ and VAD and DIV were weak sinks (-0.14 and $-0.49 \times 10^{-6} s^{-2}$, respectively).

Overall, the component vorticity budget calculations show that the tilting term (TILT) was an overall source of vorticity generation in all three components. Thus, in this case study of a slow-moving prefrontal convective

rainband, the tilting of vorticity (especially horizontal vorticity) into the vertical could have enhanced vertical vorticity generation within this rainband thus aiding in the lifetime of the existing cells and in the development of new cells along the gust front.

Chapter 6

Conclusions

The budget studies of total kinetic energy, horizontal momentum flux and three-dimensional vorticity were calculated and analyzed for a prefrontal convective rainband associated with the Mei-Yu front that occurred on 25 June 1987 over northern Taiwan. Dual-Doppler data collected during TAMEX IOP-13 were objectively analyzed in a horizontal domain of $35 \times 40 \text{ km}^2$ using a 1 km grid spacing. Ten vertical levels were chosen and ranged from 0.25 to 8.75 km with a vertical grid spacing of 1 km (except for the lowest two levels where the vertical grid spacing was 0.5 km). The horizontal domain was rotated so that the x-axis was normal and the y-axis was parallel to the rainband under investigation. Also, since the prefrontal convective rainband propagated slowly to the southeast, rotating the domain in this manner made it a consistent domain for both the 0653 and 0700 LST data sets. The three-dimensional winds were subjected to variational analysis to render them internally consistent. Vertical velocities were obtained using the anelastic continuity equation with downward integration. Fields of perturbation pressure and temperature were retrieved from the Doppler-derived winds using the three momentum equations. These parameters were then subjected to internal consistency checks and thoroughly interpreted before inserting them into the various equations for the budget calculations.

Results of the total kinetic energy budget reveal that the horizontal generation and total buoyancy terms acted as main sources of kinetic energy, while frictional dissipation and horizontal flux divergence both acted as main sinks of kinetic energy generation. The horizontal flux divergence and the vertical flux divergence terms of the kinetic energy budget were in quasi-balance at almost all levels. There was an upward transport of mean kinetic energy throughout the rainband with the strongest upward transport occurring in the middle levels coincident with the strongest convective updrafts. This may help explain the formation of the middle-level jet (MLJ) and the dissipation of the low-level jet (LLJ) during convection.

Pertaining to momentum flux, it was found that the vertical transport of horizontal momentum due to eddies normal to the rainband ($\overline{u'w'}$) was counter-gradient below 7 km, which is contrary to "mixing-length" theory. For the component line-parallel to the rainband ($\overline{v'w'}$), countergradient transport also occurred in the middle levels but downgradient transport occurred in the lower and upper levels. Momentum-flux budget calculations showed that the shear production, the total buoyancy and the velocity-pressure interaction terms were the most significant contributing processes for both components of eddy horizontal momentum flux. For $\overline{u'w'}$, the normal component, the pressure and buoyancy terms were in quasi-balance throughout the depth of the system with the buoyancy term acting primarily as a source for the local time-change of $\overline{u'w'}$ ($\partial\overline{u'w'}/\partial t$). The shear production term was a strong sink for $\partial\overline{u'w'}/\partial t$ in

the middle levels, coincident with the location of the strongest positive vertical shear of the u-component of the wind. For the line-parallel component ($\overline{v'w'}$), the same three processes were dominant except the buoyancy term was found to be sink of $\partial\overline{v'w'}/\partial t$ below 8 km. The pressure and buoyancy terms were opposite in sign from each other and from their x-component counterparts. Shear production of the y-component of eddy horizontal momentum flux was a strong source for $\partial\overline{v'w'}/\partial t$ due to strong negative vertical shear of the v-component of the wind above 6 km. These findings showed that the same processes that dominated within this rainband also were the dominant forces in several other cases. However, in this study, the dominant forces had an opposite effect for both the normal and line-parallel components when comparing these results to those found in the previous studies of a tropical convective line in GATE, a convective rainband in the Arabian Sea and a subtropical squall-line in TAMEX. The structure of an investigated event is a key factor in determining how the processes act on the system, therefore, one must know the structure(s) of the investigated event(s) before making any direct comparisons to other studies. In this case, the system was tilted southeastward at almost all levels, whereas in the previous studies, the systems were tilted westward throughout most levels. Therefore, finding that the dominating processes acted oppositely in this case to the previously mentioned cases is somewhat expected. Additionally, these findings may help explain the formation of the large-scale MLJ and the dissipation of the large-scale LLJ during convection, thus, illustrating how the mesoscale can provide feedback to the large-scale.

The three-dimensional vorticity budget analyses revealed several interesting findings. The mean horizontal vorticity vectors were directed northerly at low levels, easterly at middle levels and southeasterly at upper levels, consistent with the internal structure of this rainband. Each component budget calculation showed that the horizontal advection of the specific component was generally one order of magnitude larger than the other terms. For the x-component of vorticity, ξ , the horizontal advection term was a source while the vertical advection term was a sink. This was opposite for the y-component, η , where the horizontal advection term was an overall strong sink of η vorticity and the vertical advection term was a source. Thus, these two processes for the two horizontal components of vorticity tended to counteract or balance each other. The divergence term was found to be significant mainly for the y-component where it was a moderate source of η vorticity. This finding shows that the strong vertical shear of the u-component of the wind within the prefrontal convective rainband could generate vorticity through the stretching of the existing vorticity near the convective updrafts. The budget for the z-component of vorticity, ζ , showed that the typical magnitudes of the main terms were comparable to the horizontal component terms. But their budget values were generally one order of magnitude less than the other components. Therefore, the vertical vorticity component terms were more likely internally balanced than the other components. Of the processes most likely to contribute to overall positive generation of vorticity, the tilting/tipping term likely played the most influential role. Budget calculations showed that the tilting term was a source of vorticity

for all three components, especially for the x-component. Therefore, the tilting/tipping of vorticity, especially horizontal vorticity, played a significant role in maintaining the lifetime of this prefrontal convective rainband. By tilting horizontal vorticity into the vertical, the system could have enhanced its circulation (both horizontal and vertical) resulting in sustaining the existing cells and inducing growth of new convective cells along the gust front.

This study shows that, by using Doppler radar, we can study items such as the budgets of various dynamical and thermodynamical features on the meso- γ -scale. From this, we can determine how these features affect their surrounding environment at several scales of motion.

BIBLIOGRAPHY

- Armijo, L., 1969: A theory for the determination of wind and precipitation velocities with dual-Doppler radars. *J. Atmos. Sci.*, **26**, 570-573.
- Barnes, S., 1973: Mesoscale objective analysis using weighted time series observations. *NOAA Tech. Memo. ERL-NSSL-62*, 60 pp., 1973.
- Beeson, M.R., 1991: An observational study of a prefrontal convective rainband using TAMEX single- and dual-Doppler data. M.S. Thesis, Saint Louis University. 106 pp.
- Bohne, A. R., and R. C. Srivastava, 1976: Random errors in wind and precipitation fall speed measurement by a triple Doppler radar system. Preprints, *17th Radar Meteorology Conf.*, Seattle, Amer. Meteor. Soc., 7-14.
- Brandes, E. A., 1977: Gust front evolution and tornadogenesis as revealed by Doppler radar. *J. Appl. Meteor.*, **16**, 333-338.
- _____, 1978: Mesoscale evolution and tornadogenesis: Some observations. *Mon. Wea. Rev.*, **106**, 995-1011.
- _____, 1984: Relationship between radar derived thermodynamic variables and tornadogenesis. *Mon. Wea. Rev.*, **112**, 1033-1052.
- Chang, H.W., 1992: Dynamic and thermodynamic characteristics of a prefrontal convective rainband in northern Taiwan determined from TAMEX data. Ph.D. Thesis, Saint Louis University. 155 pp.
- Chen, G. T.-J., 1983: Observational aspect of the Mei-Yu phenomenon in subtropical China. *J. Met. Soc. Japan.*, **61**, 306-312.
- _____, and Y.-H. Kuo, 1991: The scientific results of TAMEX. Proceedings, *International Conference on Mesoscale Meteorology and TAMEX*. 3-6 December 1991, Taipei, Taiwan, 7-15.
- Chi, S. S., and R. A. Scofield, 1991: Study of the Mesoscale Convective Systems (MCSs) propagation characteristics over subtropical China during Taiwan Mei-Yu season. Proceedings, *Workshop on TAMEX Scientific Results*, 3-6 Dec 1991, Taipei, Taiwan, 32-41.

- Chiou, T. K., 1990: Forecasting of mesoscale convective system over southern China during the Mei-Yu period. Proceedings, *Workshop on TAMEX Scientific Results*, 24-26 September 1990, Boulder, CO., 95-102.
- Chong, M., and J. Testud, 1983: Three-dimensional wind field analysis from dual-Doppler radar data. Part III: The boundary condition: An optimum determination based on a variational concept. *J. Climate Appl. Meteor.*, **22**, 1227-1241.
- Douglas, M. W., 1992: Structure and dynamics of two monsoon depressions. Part II: Vorticity and heat budgets. *Mon. Wea. Rev.*, **120**, 1548-1564.
- Doviak, R. J., P. S. Ray, R. G. Strauch, and L. J. Miller, 1976: Error estimation in wind fields derived from dual-Doppler radar measurements. *J. Appl. Meteor.*, **15**, 868-878.
- Foote, G. B., and P. S. du Toit, 1969: Terminal velocity of raindrops aloft. *J. Appl. Meteor.*, **8**, 149-253.
- Fuelberg, H. E., and J. R. Scoggins, 1978: Kinetic energy budgets during the life cycle of intense convective activity. *Mon. Wea. Rev.*, **106**, 637-653.
- _____, and M. F. Printy, 1984: A kinetic energy analysis of the meso- β -scale severe storm environment. *J. Atmos. Sci.*, **41**, 3212-3226.
- Gal-Chen, T., 1978: A method for the initialization of the anelastic equations: Implications for matching models with observations. *Mon. Wea. Rev.*, **106**, 587-606.
- _____, 1982: Errors in fixed and moving frame of references: Applications for conventional and Doppler radar analysis. *J. Atmos. Sci.*, **39**, 2279-2300.
- _____, and C. E. Hane, 1981: Retrieving buoyancy and pressure fluctuations from Doppler radar observations: A status report. *Progress in Radar Meteorology, Atmos. Technol.*, **13**, 98-104.
- _____, and R. A. Kropfli, 1984: Buoyancy and pressure perturbations derived from dual-Doppler radar observations of the planetary boundary layer: Applications for matching models with observations. *J. Atmos. Sci.*, **41**, 3007-3020.

- Hane, C. E., R. B. Wilhelmson, and T. Gal-Chen, 1981: Retrieval of thermodynamic variables within deep convective clouds: Experiments in three dimensions. *Mon. Wea. Rev.*, **109**, 564-576.
- _____, and P. S. Ray, 1985: Pressure and buoyancy fields derived from Doppler radar data in a tornadic thunderstorm. *J. Atmos. Sci.*, **42**, 18-35.
- Hauser, D., P. Amayenc, and M. Chong, 1984: A new optical instrument for simultaneous measurement of raindrop diameter and fallspeed distributions. *J. Atmos. Oceanic Technol.*, **1**, 256-269.
- _____, and P. Amayenc, 1986: Retrieval of cloud water and vapor contents from Doppler radar data in a tropical squall line. *J. Atmos. Sci.*, **43**, 823-838.
- Jorgensen, D. P., and M. A. LeMone, 1989: Vertical velocity characteristics of oceanic convection. *J. Atmos. Sci.*, **46**, 621-640.
- Klemp, J. B., and R. B. Wilhelmson, 1978: The simulation of three-dimensional convective storm dynamics. *J. Atmos. Sci.*, **35**, 1070-1096.
- Kung, E. C., and T. L. Tsui, 1975: Subsynoptic-scale kinetic energy balance in the storm area. *J. Atmos. Sci.*, **32**, 729-740.
- Kuo, Y. H., and G. T. -J. Chen, 1990: Taiwan Area Mesoscale Experiment: An overview. *Bull. Amer. Meteor. Soc.*, **71**, 488-503.
- Lafore, J. P., J. L. Redelsperger, and G. Jaubert, 1988: Comparison between a three-dimensional simulation and Doppler radar data of a tropical squall line: Transports of mass, momentum, heat, and moisture. *J. Atmos. Sci.*, **45**, 3483-3500.
- Lee, W. C., R. Wakimoto, and R. Carbone, 1992: The evolution and structure of a "Bow-Echo-Microburst" event. Part II: The bow echo. *Mon. Wea. Rev.*, **120**, 2211-2225.
- LeMone, M. A., 1983: Momentum transport by a line of cumulonimbus. *J. Atmos. Soc.*, **40**, 1815-1834.
- _____, G. M. Barnes, and E. J. Zipser, 1984: Momentum flux by lines of cumulonimbus over the tropical oceans. *J. Atmos. Sci.*, **41**, 1914-1932.

- _____, and D. P. Jorgensen, 1991: Precipitation and kinematic structure of an oceanic mesoscale convective system. Part II: Momentum transport and generation. *Mon. Wea. Rev.*, **119**, 2638-2653.
- Lin, Y. J., and R. W. Pasken, 1982: A diagnostic study of the tornadic storm based on dual-Doppler wind measurements. *Cloud Dynamics* (Agee and Asai, Eds.), D. Reidel Publication Co., 315-328.
- _____, T. C. Wang, and J. H. Lin, 1986: Pressure and temperature perturbations within a squall-line thunderstorm derived from SESAME dual-Doppler data. *J. Atmos. Sci.*, **43**, 2302-2327.
- _____, and R. G. Hughes, 1987: Structural features of a microburst-producing storm in Colorado revealed by JAWS dual-Doppler radars. *J. Atmos. Sci.*, **44**, 3641-3655.
- _____, and P. M. Condray, 1988: Momentum flux in the subcloud layer of a microburst-producing thunderstorm determined from JAWS dual-Doppler data. *Boundary-Layer Meteorology*, **43**, 125-141.
- _____, and J. A. Coover, 1988: A kinetic energy analysis of a microburst-producing thunderstorm based on JAWS dual-Doppler data. *J. Atmos. Sci.*, **45**, 2764-2771.
- _____, T. C. Wang, R. W. Pasken, and H. Shen, and Z. S. Deng, 1990: Characteristics of a subtropical squall line determined from TAMEX dual-Doppler data. Part II: Dynamic and thermodynamic structures and momentum budgets. *J. Atmos. Sci.*, **47**, 2382-2399.
- _____, and P. G. LaPointe, 1991: Observational study of a multiple microburst-producing storm. Part III: Vorticity budgets. *TAO*, **2**, 217-241.
- _____, R. W. Pasken, and H. Shen, 1991: Momentum-flux budgets of a subtropical squall line in TAMEX IOP-2 based on dual-Doppler data. Preprints, *International Conference on Mesoscale Meteorology and TAMEX*, 3-6 December, Taipei, Taiwan, Meteor. Soc. Rep. China and Amer. Meteor. Soc., 133-139.
- _____, H. Shen, and R. W. Pasken, 1991: Kinetic energy budget of a squall line over the Taiwan straits revealed by dual-Doppler radar. *Mon. Wea. Rev.*, **119**, 2654-2663.

- _____, R. W. Pasken, and H. W. Chang, 1992: The structure of a subtropical prefrontal convective rainband. Part I: Mesoscale kinematic structure determined from dual-Doppler measurements. *Mon. Wea. Rev.*, **120**, 1816-1836.
- _____, H. W. Chang, and R. W. Pasken, 1993: The structure of a subtropical prefrontal convective rainband. Part II: Dynamic and thermodynamic structures and momentum budgets. *Mon. Wea. Rev.*, **121**, (in press).
- Miglioranza, M. J., 1992: The kinematic structure of a prefrontal convective rainband revealed by TAMEX Doppler radar data. M.S. Thesis, Saint Louis University, 114 pp.
- Nelson, S. P., and R. A. Brown, 1987: Error sources and accuracy of vertical velocities computed from multiple-Doppler radar measurements in deep convective storms. *J. Atmos. Ocean. Technol.*, **4**, 233-238.
- Parsons, D. B., R. A. Kropfli, J. M. Schmidt, and T. Gal-Chen, 1983: Comparisons between Doppler radar derived air motions in fixed and moving frames of reference. Preprints, *21st Conf. on Radar Meteorology*, Edmonton, Canada, Amer. Meteor. Soc., 558-564.
- _____, C. G. Mohr, and T. Gal-Chen, 1987: A severe frontal rainband. Part III: Derived thermodynamic structure. *J. Atmos. Sci.*, **44**, 1615-1631.
- Rao, G. V., and T. H. Hor, 1991: Observed momentum transport in monsoon convective cloud bands. *Mon. Wea. Rev.*, **119**, 1075-1087.
- Ray, P. S., K. K. Wagner, K. W. Johnson, J. J. Stephens, W. C. Bumgarner, and E. A. Mueller, 1978: Triple-Doppler observations of a convective storm. *J. Appl. Meteor.*, **17**, 1201-1212.
- _____, C. L. Ziegler, W. Bumgarner, and R. J. Serafin, 1980: Single and multi-Doppler radar observations of tornadic storms. *Mon. Wea. Rev.*, **108**, 1607-1625.
- Roux, F. J., Testud, M., Payen, and B. Pinty, 1984: West African squall-line thermodynamic structure retrieved from dual-Doppler radar observations. *J. Atmos. Sci.*, **41**, 3104-3121.
- Sekhon, R. S., and R. C. Srivastava, 1971: Doppler radar observations of drop-size distributions in a thunderstorm. *J. Atmos. Sci.*, **28**, 983-994.

- Stevens, D. E., 1979: Vorticity, momentum and divergence budgets of synoptic-scale wave disturbances in the tropical eastern Atlantic. *Mon. Wea. Rev.*, **107**, 535-550.
- Townsend, T. L., and J. R. Scoggins, 1983: The influence of convective activity on the vorticity budget. *NASA Contractor Report-3752*, NASA Marshall Space Flight Center, Alabama, 105 pp.
- Tsui, T. L., and E. C. Kung, 1977: Subsynoptic-scale energy transformations in various severe storm situations. *J. Atmos. Sci.*, **34**, 98-110.
- Wang, T. C., Y. J. Lin, R. W. Pasken, and H. Shen, 1990: Characteristics of a subtropical squall line determined from TAMEX dual-Doppler data. Part I: Kinematic structure. *J. Atmos. Sci.*, **47**, 2357-2381.
- Wilson, J. W., R. D. Roberts, C. Kissinger, and J. McCarthy, 1984: Microburst wind structure and evaluation of Doppler radar for airport wind shear detection. *J. Climate. Appl. Meteor.*, **22**, 1227-1241.
- Wiseman, M. L., and J. B. Klemp, 1986: Characteristics of isolated convective storms. *Mesoscale Meteorology and Forecasting* (Edited by Ray, 1986), Chapter 15., Amer. Meteor. Soc., Boston, MA, 331-358.
- Ziegler, C. L., P. S. Ray, and N. C. Knight, 1983: Hail growth in an Oklahoma multicell storm. *J. Atmos. Sci.*, **40**, 1768-1791.

BIOGRAPHY OF THE AUTHOR

Martin Russell Martino was born on September 9, 1959 and grew up in Roanoke, Illinois. After graduating from Roanoke-Benson High School in 1977, he attended Black Hawk College in Moline, Illinois. He transferred to Indiana State University in Terre Haute, Indiana on a baseball scholarship and was selected as a CoSida Academic All-American outfielder in 1981. Upon graduating from ISU with a B.S. degree in Chemistry, he married Natalie Miracle and spent the next two years playing professional baseball in the Kansas City Royals organization. In 1984, he attended the Air Force Officer Training School in Texas where he was commissioned as an Air Force officer.

His first assignment was attending the Basic Meteorology Program at St. Louis University. In 1985, he was assigned to Air Force Global Weather Center in Nebraska. In 1987, he attended Squadron Officer School at Maxwell AFB, Alabama and was selected as a distinguished graduate. In 1988, he and his family were transferred to Schwaebisch Gmuend, West Germany where he was the Staff Weather Officer for the U.S. Army 56th Field Artillery Command (PERSHING). In 1991, he was offered through the Air Force Institute of Technology the challenge to pursue a Master of Science degree in Meteorology at St. Louis University. He gratefully accepted the challenge.